

LITHIUM NIOBATE MICROPHOTONIC MODULATORS

by

David Alan Cohen

A Dissertation Presented to the
FACULTY OF THE GRADUATE SCHOOL
UNIVERSITY OF SOUTHERN CALIFORNIA
in Partial Fulfillment of the
Requirements for the Degree
DOCTOR OF PHILOSOPHY
(Electrical Engineering)

May 2001

Copyright 2001

David Alan Cohen

Acknowledgements

First and foremost I would like to offer my entire family the gratitude that words alone cannot describe for the constant love, giving, sharing, support, and encouragement that has defined much of who I am today. They are all truly the backbone of my life. To my dad whom I owe so much for the years of long hours and hard work he has put in, to provide me everything he could, and yet ask for nothing more than my happiness in return. To my mom whom by overcoming so many personal challenges in life taught the persistence and patience I needed to achieve this goal. My debt to them is incalculable and I dedicate this work to them. I thank my wife Imelda for her love and encouragement over the years, and especially for tolerating my long work hours, and to my son Alexander who gave me the greatest incentive of all to obtain this goal.

To my wife's parents, all my sisters and brothers (Deanna, Jancy, Caroline, Irene, and Henry), Aunts and Uncles, Oms and Tantes, cousins, and niece (Jai Jai), who have given me so much confidence to finish. Especially Deanna who has always given me her constant support, while still putting up with me all those years. Also Uncle Vern and Aunt Jean, who I know are always there when I need them. Finally, to my Grandpa and Grandma Marshall and Grandma Cohen who defined the importance of love and family to me, and to my Grandad Cohen who expected the best out of me, I thank you.

With deep appreciation I would like to thank my advisor Dr. Anthony Levi for challenging me to achieve my best. His direction and insights helped me become the scientist and engineer that I am today. His inspiring ideas, guidance, and encouragement gave me the confidence to achieve all that I have.

Many of the skills used in this work were learned through collaborations with others. Namely, I would like to thank Dr. Newton Frateschi for training me in the cleanroom. Dr. Sherali Zeadalli who taught me the basics of much of my computer knowledge. I would like to thank Dr. Harold Fetterman and Dr. Yian Chang from UCLA for their work on the Optically Controlled phased array project, and Dr. Lute Maleki and Dr. Vladimir Ilchenko for there collaboration while at Jet Propulsion Laboratory. Finally, I thank Dr. Michael Barnoski for all his lessons on how the real world outside of the university works, and his insights into the world of business.

I would like to thank Dr. Robert Hellwarth and Dr. Aluizio Prata Jr. for agreeing to serve on my qualification and defense committees, and Dr. Elsa Garmire for the confidence she gave me during my early years at USC.

I owe much of my sanity over the years at USC to Kim Reid. She is the best I've seen at what she does, and did much of the behind the scenes work that made my

research possible. But more importantly she was always an uplifting spirit in the group, and was always there for me to talk with during difficult times.

To my fellow long-term group members Dr. Sumesh Thiyagarajan, Dr. Bharath Raghavan, Dr. Ashok. Kanjamala, and Dr. Bindu Madhavan. All of them showed me what a true group should really be about. From the sharing of time and ideas, to the sharing of thoughts and beliefs. For all of you and Kim, I “take a step back”. But this time to appreciate all that you have meant to me, and the lasting impression you’ve had both on this work, and on my life. Especially Sumesh, whose technical impact on this work is immeasurable, and whose emotional support given to me over the years is incalculable.

Many other group members have helped during my time at USC. Namely, Fernando Harriague, Mani Hossein-Zadeh, Jeff Sondeen, and Panduka Wijetunga. I would like to especially thank Mani Jr., whose hard work contributed greatly toward the completion of this work. I would also like to thank both Steven Meier and Erich Ippen for both their friendship and academic help through my first years in the Physics department at USC.

I would also like to thank all my friends, especially Bruce, John, Mike, and Lisa whose help in innumerable ways allowed me to reach this step in my life. Finally, I

must thank both the UCLA basketball and football teams for the national championship and 8 year win streak that made my stay at USC much more pleasant.

Abstract

This work addresses the physics and engineering challenges which must be overcome to create a new class of small, light-weight, power-efficient, RF-photonic devices for use in indoor wireless communication applications. It is possible that opto-electronic solutions for indoor wireless systems may out-perform purely electronic versions. To achieve this goal, a new microphotonic mm-wave receiver architecture with direct electrical-to-optical conversion is presented. Central to such an architecture is the microphotonic optical modulator. This active optical component directly converts the received RF carrier frequency to an optical carrier frequency by interaction of optical and RF electric fields via the electro-optic effect. The modulator uses high- Q RF and microphotonic electro-optic resonators which are operated in simultaneous resonance. Fabrication of these new devices in the electro-optic material Lithium Niobate, and application of advanced RF coupling designs enable efficient interaction of RF and photonic electromagnetic fields. Simulations indicate that efficient modulation of an optical carrier at RF in the *mm*-wave range can be realized. Experimental results approaching 100% optical modulation at *GHz* frequencies in the RF, optical, and time- domain are presented. In addition, experiments demonstrating modulation of an optical carrier at RF in the *mm*-wave range are reported. This introduction of an active microphotonic modulator in an electro-optic material creates an entirely new dimension to contemporary microresonator research that has never before been investigated.

Table of Contents

page

1	Introduction	1
1.1	Motivation	1
1.1.1	Conventional <i>mm</i> -wave electronic wireless receiver architecture	3
1.1.2	Microphotonic architecture for a <i>mm</i> -wave electronic wireless receiver	4
1.2	Research approach	9
1.3	Brief survey of related research	11
1.3.1	Optical whispering gallery mode microspheres	13
1.3.2	Microsphere sensors	16
1.3.3	Optical coupling into spherical devices	17
1.3.4	Passive ring and disk shaped waveguide resonators	19
1.3.5	Active ring and disk shaped microlaser cavities	20
1.3.6	Conventional optical modulators	22
1.3.7	Resonant Fabry-Perot modulators and comb generators	23
1.4	Thesis Organization	24
1.5	References	25
2	LiNbO ₃ microphotonic modulator design and fabrication	31
2.1	Introduction	31
2.2	Material properties	32
2.3	Microphotonic optical resonator fabrication	36
2.4	Optical coupling	38
2.5	Electrical coupling to the microphotonic modulator	41
2.5.1	Patterned metal electrodes	42
2.5.2	Metal-walled RF cavity	48
2.6	Summary	49
2.7	References	50
3	Passive LiNbO ₃ microphotonic modulator	52
3.1	Introduction	52
3.2	Whispering gallery mode excitation	52
3.3	Experimental setup	63
3.4	Principles of the coupler-resonator system	66
3.5	Optical losses and the quality factor Q	73
3.6	Optical spectrum	75
3.7	Optical pulse response	77
3.8	Electrical material properties	78

3.9	Summary	79
3.10	References	80
4	LiNbO ₃ microphotonic modulator	82
4.1	Introduction	82
4.2	Direct-contact static and base-band experimental setup	83
4.3	Static voltage response of the microphotonic resonator.....	84
4.4	Base-band RF modulation	86
4.5	Electrical pulse response of the LiNbO ₃ resonator	88
4.6	Out-of-band modulation	91
4.6.1	Introduction to RF resonator design principles	92
4.6.2	Resonant periodic metal-electrode modulation approach	93
4.6.3	Single pass periodic metal-electrode modulation simulation.....	96
4.6.4	Resonant periodic metal-electrode modulation simulation in the Mach-Zehnder configuration.....	98
4.6.5	Resonant periodic metal-electrode modulation simulation without a reference arm.....	107
4.7	Direct-contact (“T - electrode”) modulation	109
4.7.1	Experimental results of RF modulation	110
4.7.2	Experimental results of <i>mm</i> -wave modulation.....	114
4.8	Side-coupled-electrode modulation.....	117
4.8.1	Experimental results of RF modulation	119
4.8.2	Experimental results of <i>mm</i> -wave modulation.....	128
4.9	Measured linearity of LiNbO ₃ optical microresonator.....	130
4.10	Scaling of the LiNbO ₃ microresonator	132
4.11	System impact/efficiency	133
4.11.1	Thermal stability	133
4.11.2	System noise.....	134
4.12	Summary	140
4.13	References	141
5	Conclusion and future work	142
5.1	Conclusions	142
5.2	Future work	145
Appendix A	Microwave band designations	150
A.1	Designation of the microwave spectrum	150
A.2	References	151
Appendix B	Bibliography.....	153

List of Figures

page

- Figure 1.** Schematic of basic conventional wireless receiver architecture consisting of analog electronic circuitry in monolithic microwave integrated circuit (MMIC) modules and a Digital Signal Processing (DSP) module. An electromagnetic wave received at a RF antenna is pass-band filtered, amplified, and fed to a mixer. A local oscillator (LO) also feeds the mixer whose output is filtered to obtain base-band. 4
- Figure 2.** Insertion of *mm*-wave microphotonic device technologies in future broadband heterodyne wireless architectures. An electromagnetic wave received at a RF antenna feeds electrodes of the microphotonic modulator. The modulator directly converts the RF signal to an optical carrier via the electro-optic effect. The resulting phase-modulated optical signal is converted to amplitude-modulation through the use of a standard Mach-Zehnder configuration. After conversion to the optical domain, the signal is processed using all-optical techniques before down-converting to base-band at the PIN photodetector. 5
- Figure 3.** A graphic showing the electric field spectrum as the signal progresses through the microphotonic architecture. A received *mm*-wave carrier frequency with AM side-bands modulates the optical field which is resonant within the electro-optic microphotonic resonator. The incident RF signal is converted from a RF carrier frequency to an optical carrier frequency. The detected optical spectrum consists of an optical carrier frequency, Ω_{opt} , optical sub-carrier frequencies $\Omega_{opt} \pm f_{RF}$, and optical base-band modulation about each sub-carrier frequency. This modulated light may then be carrier suppressed and detected at the optical receiver. The low-pass frequency response of the optical receiver is used to detect and filter the base-band signal. 7
- Figure 4.** Photograph of a conventional 18 GHz LiNbO₃ Mach-Zehnder modulator manufactured by Lucent Technologies placed next to a *z*-cut LiNbO₃ disk with gold electrodes. The Lucent device is greater than 5 cm long compared to the disk, which has a radius of 3 mm. 9
- Figure 5.** Schematic detail of a microphotonic-based *mm*-wave RF detector. An electromagnetic wave received at a RF antenna feeds electrodes of the microphotonic modulator. The modulator directly converts the RF signal to an optical carrier via the electro-optic effect. The resulting phase-modulated optical signal is converted to amplitude modulation using a standard Mach-Zehnder configuration. 10

Figure 6. (a) Photograph of Cal Tech’s add-drop device using a 50 μm radius whispering gallery-mode silica microsphere with tapered fiber couplers. (b) Measured insertion loss for the resonator shown in (a). An optical coupling loss of less than 3 dB has been measured. As will be described in Chapter 3, the low intentionally loaded Q of 4×10^4 is the advantageous result of overcoupling.	14
Figure 7. (a) Scanning electron microscope image of an InGaAs/InGaAsP multiple quantum well whispering gallery mode microdisk laser with radius $R = 0.8 \mu\text{m}$ and thickness $L = 0.22 \mu\text{m}$. The 1 μm bar provides a scale. (b) Results of simulating the electromagnetic field intensity of a $M = 5, N = 1$, resonance for a microdisk similar to that shown in (a) with radius $R \sim M\lambda/2\pi n_{\text{eff}}$, where λ is the resonance wavelength and n_{eff} is the effective refractive index.	21
Figure 8. Basic LiNbO ₃ microphotonic modulator geometry. The active arm of this Mach-Zehnder geometry provides optical phase shifts by way of an optically resonant electro-optic LiNbO ₃ disk, while the passive reference arm converts optical phase modulation to amplitude modulation.	32
Figure 9. LiNbO ₃ molecular structure. Niobium atoms are represented as dark gray small spheres, Lithium as light gray small spheres and Oxygen as large spheres. (a) Vertical view of the LiNbO ₃ conventional hexagonal unit cell. (b) View along c (or z) axis. (c) Octahedral oxygen structure of LiNbO ₃ [60].	33
Figure 10. (a) Sketch of the geometry of a microdisk indicating disk radius R , disk thickness d and curved side-walls with radius of curvature R' . (b) Photograph of a large z -cut LiNbO ₃ disk-shaped resonator with solid-gold top and bottom flat-electrodes and optically-polished curved side-walls. The size of the disk is indicated. (c) Photograph of a small z -cut LiNbO ₃ disk-shaped resonator. The size of the disk is indicated.	37
Figure 11. Sketch showing (a) single prism-coupling and (b) two prism-coupling of the optical field to the microphotonic resonator	39
Figure 12 Schematic representation of prism coupling by FTIR. (a) Materials of refractive index n_{prism} and n_{opt} in intimate contact. (b) Materials of refractive index n_{prism} and n_{opt} with air gap.....	40

Figure 13. Cylindrically shaped prisms have been shown to increase coupling. Above we show a standard flat prism gap, cylindrically shaped gap, and ideal prism gap needed to have 100% coupling.....	41
Figure 14. Schematic diagram of low-capacitance metal-electrode structure for RF coupling to a z -cut LiNbO_3 optical disk resonator. (a) Metal electrodes placed on the flat top and bottom surfaces of the disk are patterned into an annulus whose outer circumference is the same as the disk. (b) Metal electrodes coat the outer curved surface of the disk.....	43
Figure 15. Photograph of a with radius $R = 3 \text{ mm}$ and thickness $d = 0.74 \text{ mm}$ z -cut LiNbO_3 disk-shaped resonator with optically polished curved side-walls. Gold electrodes are placed in an annulus around the disk to increase the overlap of RF and optical fields.....	43
Figure 16. (a) Resonant parallel or shunt LCR circuit which provides current gain across the capacitor. (b) Series LCR circuit used to understand maximum power transfer to the RF circuit with voltage gain across the capacitor.....	44
Figure 17 Schematic cross-section diagram of metal-walled RF cavity structure showing z -cut LiNbO_3 optical disk resonator coupling to electric field lines.....	48
Figure 18 Loaded Q of a tunable metal-walled RF cavity. The center frequency is tunable from 7 GHz to 11 GHz , and the electrical $Q = 325$	49
Figure 19 The coordinate system used to solve the electromagnetic modes of a spherical resonator.	53
Figure 20 Photograph of z -cut LiNbO_3 disk-shaped resonator with gold electrodes and optically polished curved side-walls.....	54
Figure 21. Normalized modal distributions for $l = m = 1, 5, \text{ and } 24$. (a) Projection of spherical harmonics on a unit sphere for $(l,m) = (1,1), (5,5), \text{ and } (24,24)$. The energy distribution becomes more concentrated near the equator as l and m increase. (b) Longitudinal cross section (x - z plane) showing WGM for $\eta = 1$, and $(l,m) = (1,1), (5,5), \text{ and } (24,24)$. The trend shows the concentration of field toward both the equator and disk edge as l and m increase. Note for $l = m = 5$, the mode number m is odd, and therefore two maxima in the cross section. (c) Equatorial cross section of WGM for $\eta = 1$, and $(l,m) = (1,1), (5,5), \text{ and } (24,24)$. The	

trend shows the increase in lobe number, and the concentration of field toward the disk edge as l and m increase. 59

Figure 22. Normalized modal distributions for $l = 24$, and $m = 23, 22$, and 21. (a) Projection of spherical harmonics on a unit sphere for $(l,m) = (24,23), (24,22)$, and $(24,21)$. At $l-m=0$, the mode is Gaussian and centered about the equator. As $l-m$ increases, the energy distribution spreads further from the equator. (b) Longitudinal cross section ($x-z$ plane) showing WGM for $\eta = 1$, and $(l,m) = (24,23), (24,22)$, and $(24,21)$. The trend shows the concentration of field expands away from the equator as m is increased. 61

Figure 23. WGM power distribution for disks of large $l = m$. (a) Normalized profile of spherical Bessel functions with $\eta = 1$ for a 2.0 mm ($l = 8690$), 3.5 mm ($l = 15,120$), and 5.84 mm ($l = 25,260$) disk. The full width half maximum (FWHM) of the modes are 2.6 μm , 3.7 μm , and 4.8 μm for the 2.0 mm, 3.5 mm, and 5.84 mm disks respectively, (b) Normalized profile of spherical harmonics using Hermite polynomial approximation for $N = l-m = 0, 1, 2$, and 3, for a 2.0, 3.5, and 5.84 mm disk. 62

Figure 24 (a) Single prism coupling. Light is coupled into the disk using a single prism. The output is a series of resonant dips. (b) Two prism coupling. Light is coupled into the disk in one prism, and output at another prism. The output is a series of resonant peaks. 64

Figure 25 Top view of two prism coupling using diamond prisms. Input light is coupled into the prism on the right. Light output from the disk is collected at the single mode fiber output coupler. 64

Figure 26. (a) Photograph of LiNbO₃ disk and prism-coupler viewed from above. (b) Infrared side-view of disk resonator and prism showing optical coupling at $\lambda = 1550 \text{ nm}$ wavelength. Coupled laser light on the disk periphery is indicated by the arrow. 65

Figure 27 Directional coupler model used to understand coupling principles. Photons incident on the input directional coupler are evanescently transferred into a ring or disk. After traveling around the disk, light is evanescently coupled out of the resonator at either output 1 or output 2. 67

Figure 28. Fraction of light coupled into the disk as a function of the coupling coefficient κ_1 for a disk of radius 3 mm with $Q \sim 4 \times 10^6$ ($\alpha_{01} = 0.02 \text{ cm}^{-1}$) assuming single prism coupling ($\kappa_2 = 0$). (a) In the

undercoupled region, not all of the input light couples into the disk. (b) With critically coupling all of the input light is coupled into the disk, and no light couples out. (c) Overcoupling occurs when all of the input light couples into the disk, but some couples back out. 72

Figure 29. Measured optical resonance near wavelength $\lambda = 1550 \text{ nm}$ of a z -cut LiNbO_3 disk-shaped resonator with gold electrodes and optically polished curved side-walls. The measured Q of this device is in excess of 4×10^6 74

Figure 30. (a) Optical spectrum of TE polarized light. The disk cross-section above the spectra show electric field polarization and z -axis orientation for TE polarized light. This shows the many modes observed when the alignment is optimized for maximum optical throughput. (b) Optical spectrum of TM polarized light. The disk cross-section above the spectra show electric field polarization and z -axis orientation for TM polarized light. The disk used has a diameter 5.85 mm and thickness of 0.7 mm . Wavelength is $1.5 \mu\text{m}$. (c) Optical spectrum for TE polarized light when alignment is optimized for single optical mode excitation. 76

Figure 31. (a) Optical pulse used to probe the rise and decay times of the passive optical cavity. The 80 ns pulse has a $1/e$ risetime of 700 ps . (b) Q limited optical pulse output of passive microresonator cavity. 78

Figure 32. (a) Picture and schematic showing the strip-line geometry used to couple the RF electromagnetic field into and out of the passive resonator. (b) Measured RF resonance near 19.15 GHz with a measured Q in the LiNbO_3 disk of 680. The LiNbO_3 disk is 8 mm in diameter and 3.3 mm thick. The z -axis of the crystal is oriented normal the plane of the striplines in (a). 79

Figure 33. (a) Top view of single prism coupling setup. (b) Side cross-section of single prism coupling setup. 83

Figure 34. (a) Photograph of a z -cut LiNbO_3 disk-shaped resonator with optically polished curved side-walls. Gold electrodes are placed in an annulus around the disk to increase the overlap of electrical bias and optical fields. The dimensions of the disk are radius $R = 5.8 \text{ mm}$ and thickness $d = 0.74 \text{ mm}$. (b) Measured shift in resonant wavelength due to application of 8 V DC bias between the top and bottom electrodes of the disk shown in (a). The change in resonant wavelength is 0.07 pm/V 85

Figure 35. (a) Detected small-signal RF optical modulation as a function of frequency for a LiNbO ₃ disk of radius $R = 3 \text{ mm}$. The inset shows the corresponding optical line-width of the high-Q whispering gallery mode resonance. (b) Time domain modulation of the LiNbO ₃ by application of a 10 MHz square wave.	87
Figure 36. (a) Base-band modulation mechanism. Maximum ($+V_0$) and minimum ($-V_0$) shift of resonance frequency during base-band modulation. Input at the wavelength λ_2 will result in amplitude modulation between points a and b. Input at the wavelength λ_1 will result in frequency doubling. (b) 100 kHz optical modulation amplitude versus wavelength for an applied 100 kHz modulation. Black line is for zero applied modulation. The gray band is the modulation amplitude vs. wavelength. Modulation at doubled frequencies (200 kHz) is not shown.	88
Figure 37. (a) Electrical RF pulse imparted on the ring electrode of the disk. Pulse width = 200 ns, repetition rate = 10 μs , and pulse risetime of 125 ps. (b) Detected optical pulse generated by the input electrical pulse. Overlaying this is a pulse generated by pulsing the input light with no applied RF.	89
Figure 38. (a) Electrical RF pulse imparted on the ring electrode of the disk. Pulse width = 200 ns, repetition rate = 10 μs , and pulse risetime of 125 ps. (b) Detected optical decay time generated by the input electrical pulse. Overlaying this is the decay time of a pulse generated by pulsing the input light with no applied RF.	91
Figure 39. Schematic showing the receiver proposed for mm-wave RF detection. An electromagnetic wave received at a RF antenna feeds electrodes of the microphotonic modulator. The modulator directly converts the RF signal to an optical carrier via the electro-optic effect. The resulting phase-modulated optical signal is converted to amplitude-modulation through the use of a standard Mach-Zehnder configuration.	94
Figure 40. Calculated response of a microphotonic-based opto-electronic modulator with the indicated periodic metal-electrode structures and $f_0 = 7 \text{ GHz}$. (a) A $R = 3.18 \text{ mm}$ LiNbO ₃ disk modulator with $\kappa = 1$ and a continuous ring-electrode. (b) $\kappa = 1$ optical-coupling with a split 4-segment ring-electrode showing a peak in opto-electronic response at 14 GHz.	97

- Figure 41.** Calculated response of a microphotonic-based opto-electronic modulator with the indicated periodic metal electrode structures. (a) A $R = 3.18 \text{ mm}$ LiNbO₃ disk modulator with $\kappa = 0.05$ and a continuous ring electrode. (b) $\kappa = 0.05$ with a split 2-segment ring-electrode showing resonant opto-electronic response at 7 GHz . (c) $\kappa = 0.05$ with 4 segments and response at 14 GHz . (d) $\kappa = 0.05$ with 10 segments showing response at 35 GHz 100
- Figure 42.** (a) Log scale of the $\kappa = 0.05$ with a split 2-segment ring-electrode calculated response. (b) Expanded view of the base-band response. (b) Expanded view of the fundamental 7 GHz modulation response showing a modulation dip at the center of the modulation peak. (d) Expanded view at 14 GHz showing a null in modulation at the second harmonic..... 102
- Figure 43.** (a) CW optical resonance peak centered at wavelength λ_{peak} . (b) Optical modulation response as a function of applied RF frequency for the two-section electrode in Figure 42(b). (c) Optical carrier and side-band wavelengths for the three indicated RF frequencies shown in part (b). The amplitude of each wavelength is optically filtered by the resonance peak. Therefore $f_{RF} = f_2$ will have the maximum modulation as shown in (b). 104
- Figure 44.** Calculated response of a microphotonic-based opto-electronic modulator with the indicated periodic metal electrode structures and finite scattering coefficient $\alpha = 0.01 \text{ cm}^{-1}$. (a) A $R = 3.18 \text{ mm}$ LiNbO₃ disk modulator with $\kappa = 0.05$ and a continuous ring electrode. (b) $\kappa = 0.05$ with a split 2-segment ring-electrode showing resonant opto-electronic response at 7 GHz . (c) $\kappa = 0.05$ with 4 segments and response at 14 GHz . (d) $\kappa = 0.05$ with 10 segments showing response at 35 GHz 105
- Figure 45.** (a) Log scale of the $\kappa = 0.05$ and finite scattering coefficient $\alpha = 0.01 \text{ cm}^{-1}$ with a split 2-segment ring-electrode calculated response. (b) Expanded view of the base-band response. (b) Expanded view of the fundamental 7 GHz modulation response showing a modulation dip at the center of the modulation peak. (d) Expanded view at 14 GHz showing a null in modulation at the second harmonic..... 106
- Figure 46.** Simulated comparison of modulation both with and without the use of a Mach-Zehnder geometry using the single coupler geometry. Amplitude modulation without the Mach-Zehnder is shown to result in larger modulation at coupling coefficients $\kappa_1 < 0.085$. Values used in the simulation are the same as those in Figure 41(b)..... 107

Figure 47. Direct-contact electrode geometry used to excite a “T-electrode” resonator. This RF resonator is used to couple RF power onto the LiNbO ₃ disk to achieve out-of-base-band modulation.	110
Figure 48. “T-electrode” (a) Simulation geometry, with microstrip width = 1.5 mm, substrate thickness = 0.5 mm, and relative dielectric constant, ϵ_r = 2.94. (b) Simulated RF power at the resonator sensor in (a).	111
Figure 49. Measured results showing optical modulation of a 5.8 mm diameter, 0.74 mm thick LiNbO ₃ microphotonic modulator at 7 GHz. (a) The reflected swept RF excitation response, S_{11} , of the resonant electrode (“T electrode”) structure show in the inset. (b) Detected optical response at base-band frequencies versus a swept RF input. (c) Detected optical response versus a swept RF input. The resulting modulation peak is at 7.6 GHz with a measured bandwidth of 150 MHz.	112
Figure 50. (a) Optical spectrum showing the WGM used for modulation and two smaller optical side-modes. (b) Detected optical modulation response on a linear scale. Existence of the optical side-modes in (a) are the cause of the modulation side-bands shown. (c) Same as (b) using a logarithmic scale.	113
Figure 51. Electrode structure used to achieve optical modulation at 30.25 GHz. The SMA launch was tapered to reduce loading on the relatively small electrode.	115
Figure 52. (a) Measured results showing optical modulation of a 5.8 mm diameter, 0.74 mm thick LiNbO ₃ microphotonic modulator at 30.25 GHz for a CW RF input. (b) Detected optical response when the optical wavelength is tuned off the optical resonance. (c) Detected optical response when the applied RF field is tuned off the RF resonant frequency.	116
Figure 53. Coupled-line filter in a band pass filter geometry.	117
Figure 54. (a) Side-coupled resonator geometry used to achieve simultaneous resonance with RF voltage gain. (b) Simulation results showing the RF intensity at the fundamental frequency of the RF resonator. The simulation assumed a dielectric thickness, $d = 0.508$ mm, relative dielectric constant, $\epsilon_r = 2.94$, line width, $w = 1.2$ mm, disk thickness, $t = 0.7$ mm, resonator width = 1.2 mm, resonator angle = 90 degree, and gap spacing, $x = 0.3$ mm. Scale is in arbitrary linear units. The simulation was generated using Ansoft HFSS [83].	120

Figure 55. Photograph showing the experimental setup used for the side-coupled electrode coupling scheme.	121
Figure 56. Measured reflected RF power S_{11} demonstrating maximum coupling of energy to the microstrip resonator at 7.56 GHz. An absorption $Q = 144$ is measured. The geometry of the side-coupled microstrip resonator approach is shown in the inset.	121
Figure 57. (a) Detected output optical power versus input RF frequency for a $R = 2.92$ mm LiNbO ₃ disk modulator. The light exiting the disk is optically modulated at 7.56 GHz, with a bandwidth of 80 MHz. (b) Detected output optical power as a function of optical frequency is shown. Both the optical carrier at 194 THz (1.55 μ m) and 7.56 GHz optical side-bands are shown. The measured optical line width is limited by the Fabry-Perot filter resolution which is $f_{-3dB} = 900$ MHz.	122
Figure 58. Detected optical modulation as a function of RF power launched onto the RF microstrip resonator. Optical power of 1.0 corresponds to the measured optical power at the maximum of the optical resonance with no modulation. This demonstrates that near 100% modulation is achievable at voltages comparable to conventional LiNbO ₃ Mach-Zehnder interferometers.	123
Figure 59. Graph showing modulation at the fundamental frequency as a function of applied electric field. Large applied electric fields drive modulation outside of the linear response region and couple energy into higher harmonic frequencies. The inset shows that at extremely large RF fields, a smaller peak in modulation at the fundamental occurs.	125
Figure 60. (a) Measured optical resonance of the LiNbO ₃ disk near wavelength $\lambda = 1.55$ μ m. The measured Q of this device is more than 4×10^6 . Inset shows a photograph of a z -cut LiNbO ₃ disk-shaped resonator with optically polished curved side-walls. Gold electrodes are placed in an annulus around the disk to increase the overlap of electrical bias and optical fields. The dimensions of the disk are radius $R = 2.92$ mm and thickness $d = 0.74$ mm. (b) Detected optical time-domain signal showing 7.56 GHz modulation. Modulation is shown at four wavelengths referenced in (a), and is maximum at a wavelength corresponding to the maximum slope of the optical resonance.	126
Figure 61. (a) Simulated optical resonance of the LiNbO ₃ disk near wavelength $\lambda = 1.55$ μ m. The radius of the simulated disk is $R = 2.92$	

<i>mm</i> . (b) Simulated optical time-domain signals showing 7.6 GHz modulation. Modulation is shown at four wavelengths referenced in (a), and is maximum at a wavelength corresponding to the maximum slope of the optical resonance.	127
Figure 62. Reflected RF power S_{11} from a side coupled microstrip resonator showing <i>mm</i> -wave RF coupling at 30.3 GHz.	128
Figure 63. (a) Demonstration of <i>mm</i> -wave modulation at 30.37 GHz with both the RF frequency, and optical wavelength tuned into resonance. (b) When the optical wavelength is tuned off resonance, while the RF frequency stays in resonance, we see no modulation. (c) In addition, no modulation results if the optical wavelength is kept tuned on resonance, while the RF frequency is tuned off resonance.....	129
Figure 64. Modulation of the LiNbO ₃ resonator at 37.9 GHz. This was achieved using the third harmonic of a 12.6 GHz microstrip resonator.	130
Figure 65. (a) Maximum modulation response of the microphotonic resonator when excited by the fundamental frequency $f_{RF} = 7.6$ GHz. The optical wavelength is tuned near the maximum slope of the optical resonance. (b) Frequency doubled modulation response at the second harmonic $2f_{RF} = 15.2$ GHz when excited by the same RF power as (a) at a frequency $f_{RF} = 7.6$ GHz. (c) Fundamental and second harmonic modulation response for an input frequency $f_{RF} = 7.6$ GHz versus optical wavelength. This shows that frequency doubling is maximum at the optical resonance peak λ_0	131
Figure 66. Block diagram of the noise model.....	134
Figure 67. Estimated signal to noise ratio (SNR) and noise figure (NF) versus the input RF signal to noise ratio.....	137
Figure 68. Shot noise imposed maximum signal to noise ratio SNR_{in} at the antenna for a 1 μW RF signal.....	138
Figure 69. Swept RF optical modulation response of the direct contact (“T” electrode) RF coupling method. The noise floor is that of the RF spectrum analyzer.	139
Figure 70. Atmospheric attenuation for millimeter waves.....	151

Chapter 1

Introduction

1.1 Motivation

With the apparent continuous and dramatic growth of the Internet, efficient communication and data access has become a key requirement in many facets of today's information systems. This demand for broadband communication has seemingly expanded beyond the home and office desktop to indoor wireless and micro-cell wireless systems. The wide-scale implementation of microwave cellular telephone networks in the last two decades, and the continued growth of the personal data assistant (PDA) market is driving the need to develop broadband indoor wireless technologies for hand-held communicator applications.

While electronic solutions to address this demand continue to be implemented, there is also an opportunity for new, innovative technologies. It is possible that opto-electronic solutions for indoor wireless systems may out-perform purely electronic versions because of the potential for reduced weight, size and power consumption.

In addition, it also offers a low-loss, ultra-fast photonic signal-processing environment.

Today, the challenge is to develop new microphotonic components with the required performance to act as building blocks for future advanced opto-electronic RF systems. The goal is to exploit the unique properties of electro-optic microphotonic resonators to create a base-technology for practical implementations of future systems. The technologies that will be developed target efficient opto-electronic RF receivers for *mm*-wave wireless and front-end antenna applications that may find an application in micro-cell based hand-held wireless communicators.

RF receivers operating at *mm*-wave frequencies are of interest for indoor wireless and micro-cell wireless systems [1]. Higher RF carrier frequencies permit increased available bandwidth as in many new *Ka*-band systems [2]. In addition, the 60 *GHz* band is being targeted for micro-cell and pico-cell zoning owing to the high atmospheric attenuation and thereby potential for channel reuse. In this thesis, a novel architecture for these wireless and front-end antenna applications is proposed. By exploiting the unique properties of a microphotonic modulator, efficient, low-power detection in a small volume can be achieved. This receiver uses high quality factor (Q) RF and microphotonic electro-optic resonators that are operated in simultaneous resonance. Central to such an architecture is the microphotonic optical

modulator. This active optical component directly converts the received RF carrier frequency to an optical carrier frequency by interaction of optical and RF electric fields via the electro-optic effect. This introduction of an active microphotonic modulator in an electro-optic material creates an entirely new dimension to contemporary microresonator research that has never before been investigated.

1.1.1 Conventional *mm*-wave electronic wireless receiver architecture

Previous work has focused on the development and integration of all-electronic components to address these system needs [1]. Figure 1 shows the basic building blocks of a conventional *mm*-wave electronic wireless receiver architecture consisting of an analog RF front-end and a digital signal-processing (DSP) module. Typically, most power is consumed in the analog monolithic microwave integrated circuit (MMIC). A state-of-the-art 60 GHz transmit / receive *electronic* analog RF front-end module developed by NEC consumes 1.2 W of which 0.4 W is used for the receiver [1]. Key components used by the NEC group are 0.15 μm gate-length AlGaAs / InGaAs heterojunction FETs with $f_{max} > 220$ GHz for electronic circuitry and a Ba(Mg,Ta)O₃ dielectric resonator for a *fixed-frequency*, low phase-noise, local oscillator (LO) used in the receiver module. Receiver functions include pass-band filtering, low-noise electronic amplification, down-conversion using an intermediate frequency oscillator, and low-pass filtering. The analog RF front-end of the receiver has a reported digital FSK data bandwidth of greater than 10 Mb/s (6 MHz equivalent

analog bandwidth), sensitivity of $10 \mu W$, and a volume of 900 mm^3 . This work represents the present state-of-the-art. Any improvement in performance which results in significantly reduced power consumption and size will probably require a completely new approach to system design.

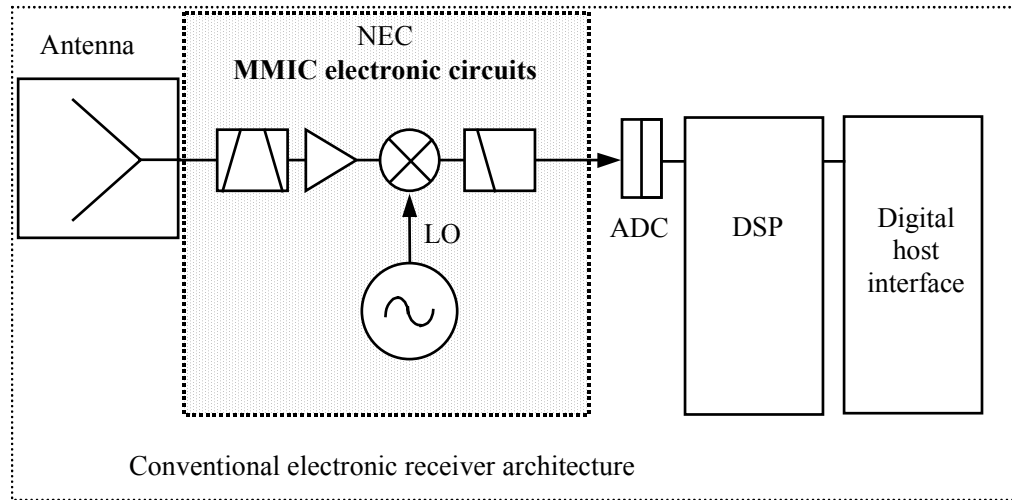


Figure 1. Schematic of basic conventional wireless receiver architecture consisting of analog electronic circuitry in monolithic microwave integrated circuit (MMIC) modules and a Digital Signal Processing (DSP) module. An electromagnetic wave received at a RF antenna is pass-band filtered, amplified, and fed to a mixer. A local oscillator (LO) also feeds the mixer whose output is filtered to obtain base-band.

1.1.2 Microphotonic architecture for a *mm*-wave electronic wireless receiver

In this thesis, I propose and present initial experimental results which use a novel, non-electronic, microphotonic architecture for these wireless applications. Operation is targeted for the RF carrier frequency range 10 GHz to 100 GHz (3 cm to 3 mm wavelength). By exploiting the unique properties of a microphotonic modulator, efficient, low-power, all-optical detection in a small volume can be achieved. Figure

2 is a schematic of the proposed architecture. An electromagnetic wave is received at a RF antenna integrated with the modulator. This *mm*-wave signal feeds the electrodes of the microphotonic resonator where the RF signal is directly converted via the electro-optic response of the modulator to a 200 THz optical carrier frequency supplied by a distributed feedback (DFB) laser. The resulting phase-modulated optical signal is converted to amplitude modulation using a standard Mach-Zehnder configuration. After all-optical signal processing, which may include filtering to suppress the optical carrier, the intensity of the amplitude-modulated optical carrier is detected by the optical receiver that is sensitive to only base-band frequencies.

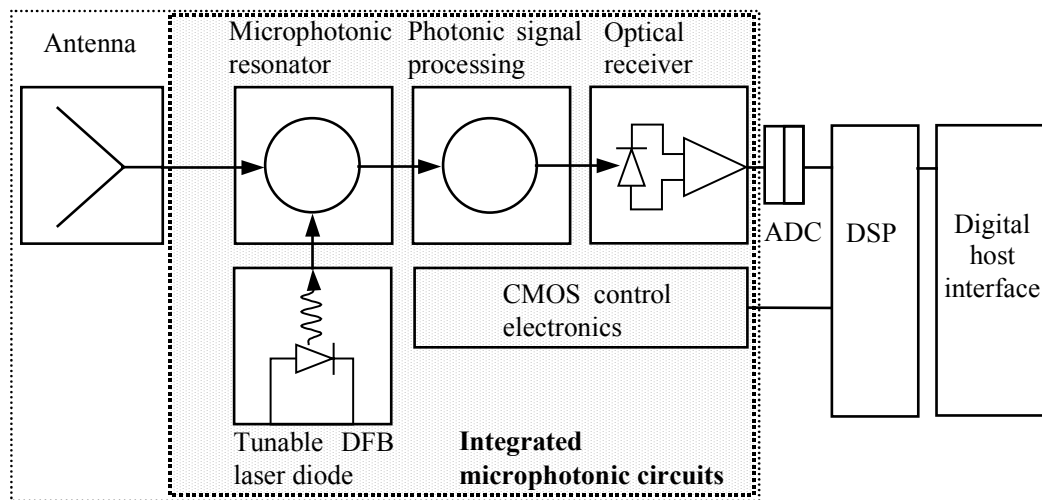


Figure 2. Insertion of *mm*-wave microphotonic device technologies in future broadband heterodyne wireless architectures. An electromagnetic wave received at a RF antenna feeds electrodes of the microphotonic modulator. The modulator directly converts the RF signal to an optical carrier via the electro-optic effect. The resulting phase-modulated optical signal is converted to amplitude-modulation through the use of a standard Mach-Zehnder configuration. After conversion to the optical domain, the signal is processed using all-optical techniques before down-converting to base-band at the PIN photodetector.

Figure 3 illustrates the RF electric field spectrum as the signal progresses through the microphotonic architecture. The received RF electric field at the antenna is composed of a *mm*-wave carrier frequency, f_{RF} , with modulation side-bands (shown in the figure using amplitude modulation (AM) as an example). The RF electric field modulates the optical field which is resonant within the electro-optic microphotonic resonator. As will be shown, if the RF carrier is a multiple of the FSR of the optical cavity, the optical field in the cavity will be modulated efficiently at the RF carrier frequency. If the base-band modulation falls within the optical Q of the photonic resonator, the detected optical spectrum will consist of an optical carrier frequency, Ω_{opt} , optical sub-carrier frequencies $\Omega_{opt} \pm f_{RF}$, and optical base-band modulation about each sub-carrier frequency. The incident RF signal has thereby been converted from a RF carrier frequency to an optical carrier frequency. This modulated light may then be carrier suppressed by a passive optical filter and detected at the optical receiver. The low-pass frequency response of the optical receiver is used to detect and filter the base-band signal.

A microphotonic optical resonator is fabricated from an electro-optic material. The resonator's optical quality-factor (Q) is high to increase the effective interaction length of photons with an applied RF electric-field. When combined with a *simultaneously* resonant RF electrical feed for voltage gain and a patterned electrode structure, high-sensitivity at *mm*-wave frequencies is achievable.

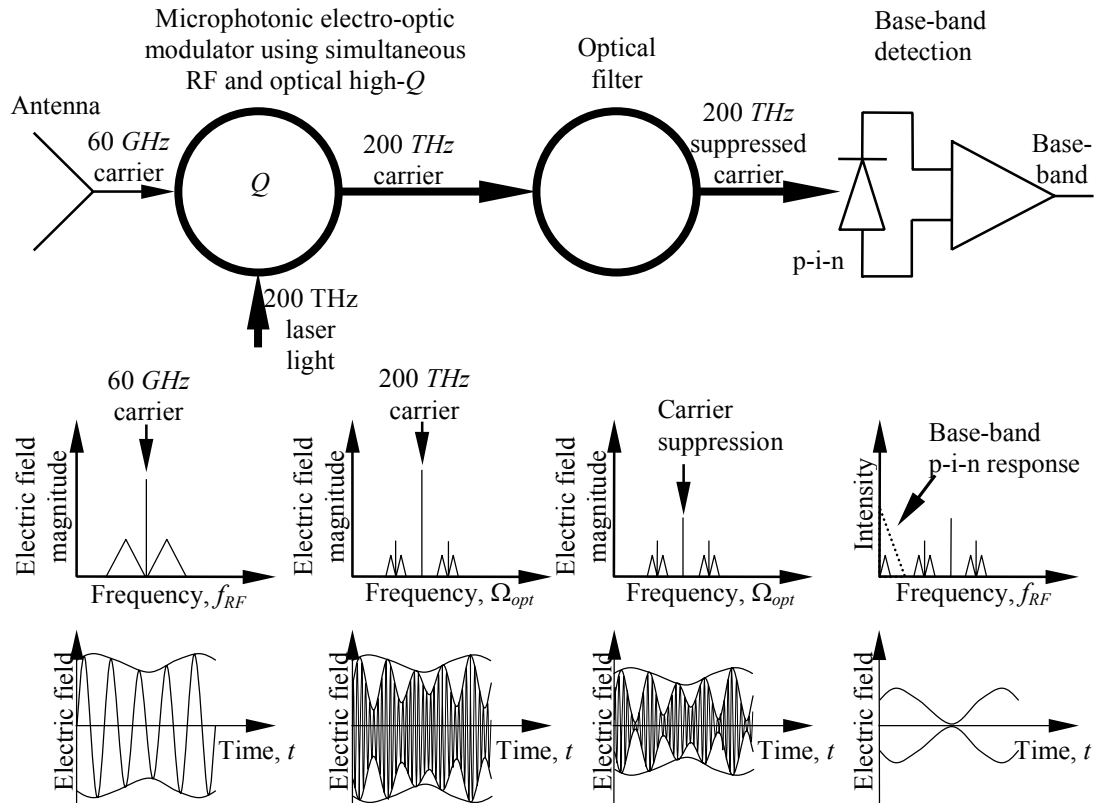


Figure 3. A graphic showing the electric field spectrum as the signal progresses through the microphotonic architecture. A received *mm*-wave carrier frequency with AM side-bands modulates the optical field which is resonant within the electro-optic microphotonic resonator. The incident RF signal is converted from a RF carrier frequency to an optical carrier frequency. The detected optical spectrum consists of an optical carrier frequency, Ω_{opt} , optical sub-carrier frequencies $\Omega_{opt} \pm f_{RF}$, and optical base-band modulation about each sub-carrier frequency. This modulated light may then be carrier suppressed and detected at the optical receiver. The low-pass frequency response of the optical receiver is used to detect and filter the base-band signal.

An initial approach to develop a microphotonic optical modulator uses a *z*-cut Lithium Niobate (LiNbO_3) disk-shaped resonator with optically-polished curved side-walls. The components are fabricated from the LiNbO_3 material system because of its high electro-optic coefficient, and its low loss at both optical and RF frequencies. Standard evanescent prism-coupling [3] is used to couple laser light

into and out of a resonant TE-polarized high- Q optical whispering-gallery mode (WGM) which exists at the periphery of the disk. A metal electrode structure fed by a RF signal is designed to overlap and be in simultaneous resonance with the optical field.

Existing methods to manipulate RF signals often involve the use of bulky, power hungry, Mach-Zehnder LiNbO₃ modulators, glass fiber, and relatively large optical filters formed from bulk optical elements or array waveguides. The reduced size advantage we expect to achieve is illustrated in Figure 4 which is a photograph of a commercially available Mach-Zehnder LiNbO₃ modulator placed next to a 3 mm radius optically polished z -cut LiNbO₃ disk with gold electrodes. An electric field between the metal electrodes of the disk interacts with photons via the electro-optic effect and not a resistive electrical load. Consequently no damping of the RF Q due to a load resistor occurs for the LiNbO₃ disk. In contrast, the conventional Mach-Zehnder modulator is a travelling wave RF design terminated with an approximately 50 Ω load. This approach results in relatively high power consumption and significant damping of simple resonant RF circuits.

The research challenges include manufacture of the high- Q microresonators, low-loss optical coupling, and efficient coupling of RF power to the microresonator. In

addition, future system integration requires development of device design and packaging.

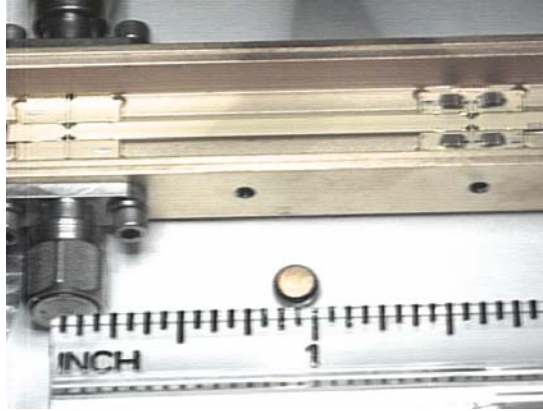


Figure 4. Photograph of a conventional 18 GHz $LiNbO_3$ Mach-Zehnder modulator manufactured by Lucent Technologies placed next to a z -cut $LiNbO_3$ disk with gold electrodes. The Lucent device is greater than 5 cm long compared to the disk, which has a radius of 3 mm .

1.2 Research approach

Figure 5 shows the schematic detail of research approach. An electromagnetic wave is received at a RF antenna integrated with the modulator. This mm -wave signal feeds the electrodes of the microphotonic resonator where the RF signal is directly converted via the electro-optic response of the modulator to a 200 THz optical carrier frequency supplied by a DFB laser. The resulting phase-modulated optical signal is converted to amplitude-modulation through use of a standard Mach-Zehnder configuration. The intensity of the amplitude-modulated optical carrier is detected using an optical receiver whose response is sensitive only to base-band frequencies.

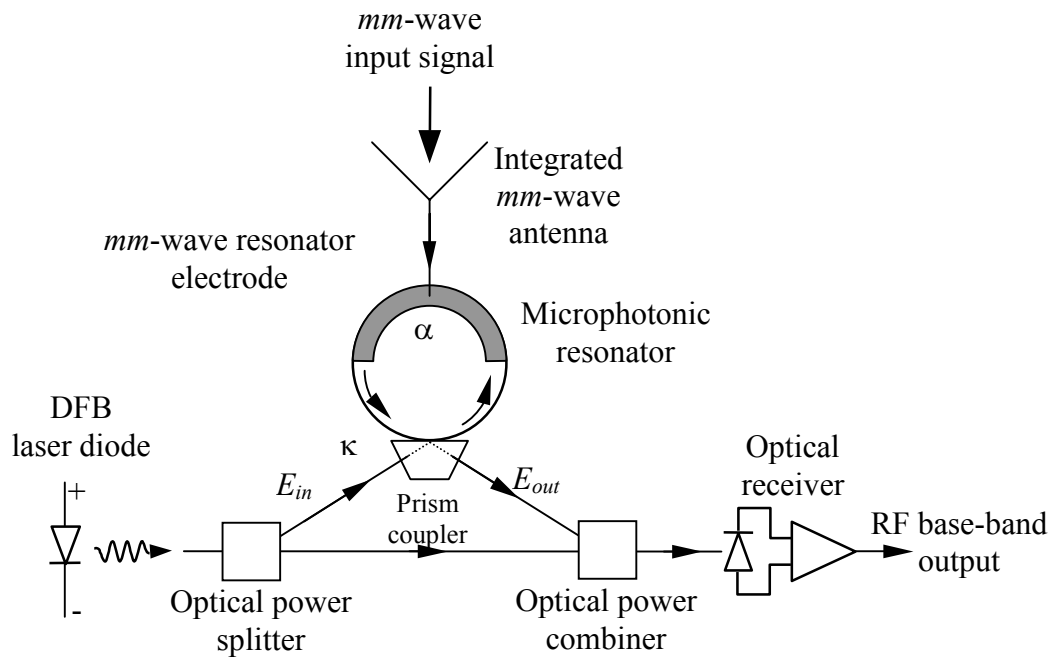


Figure 5. Schematic detail of a microphotonic-based *mm*-wave RF detector. An electromagnetic wave received at a RF antenna feeds electrodes of the microphotonic modulator. The modulator directly converts the RF signal to an optical carrier via the electro-optic effect. The resulting phase-modulated optical signal is converted to amplitude modulation using a standard Mach-Zehnder configuration.

Technology developed to produce the high-quality polished curved sidewalls for the LiNbO_3 disk has achieved smoothness sufficient for high- Q optical resonance within the disk. RF coupling to the basic optical resonator has been developed using two approaches. The first approach uses direct contact of the RF source to metal electrodes placed on the LiNbO_3 resonator. This method provides a simplified method to achieve modulation without additional complexities from the RF resonator. The second approach uses evanescent side-coupling of the RF source to metal electrodes placed on the LiNbO_3 resonator. This permits RF electric field

amplification in the system. From this we have achieved electrical to optical conversion at frequencies up to 38 GHz. In addition, models explaining these results have been confirmed through simulation. These results justify asking the following thesis question:

Thesis question:

Can simultaneous RF and optical resonance in LiNbO₃ microresonators be used for efficient mm-wave receivers?

This question is addressed through development of more refined fabrication techniques and a better understanding of device operation. Advanced polishing methods have been implemented to reduce the size of the disk both in radius and thickness to improve both electric field and optical coupling to the disk. Electrode design and manufacture has been developed to increase overlap of the electrical and optical fields in the disk. In addition, a theoretical analysis and simulation of device operation provided new ideas toward an increase of electrical to optical conversion efficiency of the LiNbO₃ microphotonic resonator.

1.3 Brief survey of related research

This research is the first to investigate high- Q optical whispering gallery mode (WGM) resonators fabricated with an electro-optic based material system. This

introduction of active microphotonic resonators in anisotropic, electro-optic material creates a new dimension to the contemporary microresonator research discussed below.

Use of whispering gallery modes permit high- Q confinement of optical power to a very small volume. These modes were first identified by Lord Rayleigh in the field of acoustics in 1910. He found that high-frequency sound waves tend to cling to concave surfaces. An example given was that of the dome of Saint Paul's Cathedral [4]. Electromagnetic propagation of WGM in dielectric cylinders was first studied by Wait in 1967 [5]. Arnaud was the first to initiate research work on WGM of RF dielectric resonators in 1981 [7].

Current work in photonic high- Q devices employs either a disk or spherical geometry for whispering gallery mode propagation. As will be discussed, the disk shaped geometry has typically been used for passive filters and semiconductor microdisks for microlasers. The principle advantage of this geometry is its two-dimensional nature, which lends itself to monolithic device design using standard lithographic patterning and etching techniques. In addition, the optical coupling structures can be defined and processed along with the device with a high degree of precision. However, etching roughness typically limits device $Q \sim 10^4$ [6]. Spherical WGM resonators have been proposed for passive filtering, sensor

applications, and investigation into the limits of high- Q physics. Spheres are more difficult to manufacture with optical coupling still a significant challenge. However, as will be mentioned, large Q 's in excess of 10^8 are regularly reported. More recent work into active devices, such as lasers is ongoing.

Finally, microsphere sensors, optical coupling methods for spherical devices, conventional LiNbO_3 modulators, and related work in resonant Fabry-Perot modulators and comb generators will be discussed.

1.3.1 Optical whispering gallery mode microspheres

Passive optical whispering gallery mode microsphere resonators are a type of optical cavity that combines small size (25 μm to 4 mm radius) with a potentially very high quality factor [8]. Microspheres are generally made by fusing the end of a fine silica fiber, while the residual stem is used for positioning and support. The current passive fused silica-based optical whispering gallery mode resonators were inspired by research into aerosol microdroplets by Hill and Brenner in the late 1980's [9] and have been investigated experimentally since 1987 [10]. Most research before the late 1990's explored methods to increase the Q of the resonator, and understand the experimentally observed mode dynamics. Recent work at JPL [11] and other institutions [12] have explored the limits of very high- Q passive optical resonator design. Quality factors exceeding $Q = 10^9$ for fused-silica microspheres

have been reported [12]. Figure 6(a) shows a photograph of a tapered-fiber coupled $50\ \mu\text{m}$ radius whispering gallery-mode silica microsphere photonic resonator. Overcoupling of this device results in an intentionally low loaded optical Q of 4×10^4 shown in Figure 6(b) [13]. Optical insertion loss for this coupling scheme is typically $3\ \text{dB}$. Experiments indicate that optical coupling loss of less than $3\ \text{dB}$ is routinely achievable. Work at Caltech [14] and JPL [15] has been reported on the fiber pig-tailing of these devices as will be discussed in the next section.

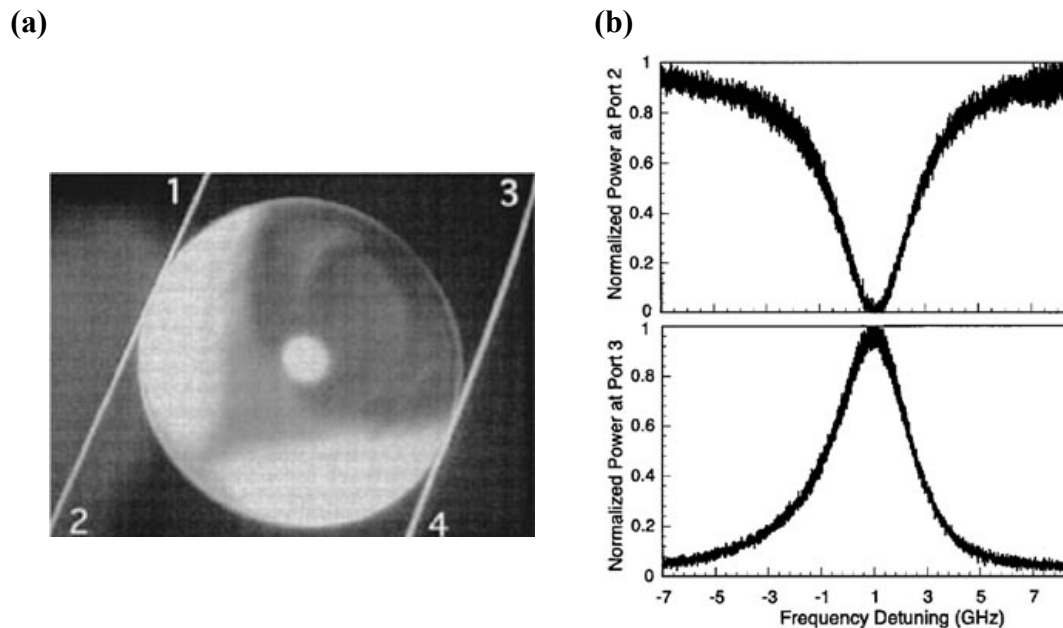


Figure 6. (a) Photograph of Cal Tech’s add-drop device using a $50\ \mu\text{m}$ radius whispering gallery-mode silica microsphere with tapered fiber couplers. (b) Measured insertion loss for the resonator shown in (a). An optical coupling loss of less than $3\ \text{dB}$ has been measured. As will be described in Chapter 3, the low intentionally loaded Q of 4×10^4 is the advantageous result of overcoupling.

Historically, fundamental physics and signal processing applications were among the first motivations for research in the area of fused silica-based microresonators. Basic

understanding of the ultimate Q of optical microsphere resonators [8], and mode analysis [16] has been investigated by V. S. Ilchenko in the mid 1990's at Moscow State University. Microspheres have also been viewed as possible enabling technologies to explore the physics of cavity quantum electro-dynamic (QED) effects. Among proposed experiments are quantum-non-demolition measurements by quantized scattering of slow resonant atoms [17] and trapping atoms by dipole forces in stable orbits around microspheres [18]. After 8 years, work continues to realize these topics experimentally. Most difficulty seems to lie in the cooling of the atoms before interaction with the microsphere [17].

More likely, the first successful application of a microsphere will come as an optical sensor or as a building block for fiber-optic applications for signal routing and filtering. Microspheres have been used by Vahala's group at Caltech for a high- Q narrow-band filter and a fiber-optic wavelength add-drop device which achieved a 5 Gbit/s BER performance with a mode spacing of several GHz . This is notable because high- Q devices typically have resonant mode widths of 10-100 MHz . By going to smaller spheres ($\sim 40 \mu m$), the dual-tapered coupled mode width was 3.8 GHz with 30 GHz mode spacing. [19]. These numbers are the closest yet to those needed for current dense wavelength division multiplexing (DWDM) applications which currently use 100 GHz (0.8 nm) and 50 GHz (0.4 nm) channel spacing [20],

however the 3 *dB* insertion loss should be improved. Drawbacks of the tapered fiber system will be addressed in the next section.

Other applications, such as a means to achieve laser diode emission wavelength stabilization have been suggested by groups in Russia [21] and whispering gallery mode microlasers with 200 *nW* thresholds in silica microspheres doped with Nd ions have been investigated by groups in France [22]. Low power output from these lasers make them novelties at this time.

All of these devices suffer from common wavelength stability, optical coupling, and packaging issues that are usually ignored in the literature, and will keep them from becoming commercially viable until these issues are addressed.

1.3.2 Microsphere sensors

Sensors using whispering gallery mode microspheres have been proposed on the premise that the evanescent field of a microsphere outside the dielectric may enable high sensitivity of the quality factor Q to conditions near the interface. In addition, the external environment, such as temperature, stress, and pressure will have an effect on the resonant frequency of the WGM. Devices such as a strain-tunable microsphere has been demonstrated experimentally [23] with optical coupling again

the key failure. Proposed research into high- Q microspheres as atmospheric trace-gas sensor are also of current interest [24].

In 1990, an experimental result from a 60 *Hz* high voltage electro-optic sensor was presented with applications in the electric power industry [25]. This spherical electro-optic sensor (SEOS) used laser interference figures produced from a single pass of laser light through a 3 *mm* LiNbO₃ sphere. Changes in the index of refraction of the sphere in the presence of a strong electric field changed the pattern of light refracted out of the sphere. The LiNbO₃ sphere had a sphericity of $6-12 \times 10^{-7}$ *m*, surface flatness of $0.5-1 \lambda$ (632.8 *nm*), and a scratch/dig of less than 5.5 [26]. At the time this paper was written, WGM research was in its infancy and the authors were probably not aware of this WGM research. In addition, their focus was sensing free-space electric fields, and the concept of electrode design to focus those fields into the sphere was not conceived. This research has now been in the literature for 10 years. That people driving the emerging microsphere WGM programs didn't use this concept demonstrates that the focus of early WGM research was more academic, and not a vision of practical commercial device development.

1.3.3 Optical coupling into spherical devices

The presence of the whispering gallery mode evanescent field outside the resonator allows efficient coupling of light both into and out of the resonator. However, the

prospect for microsphere applications have suffered from a lack of a simple coupler that could be easily incorporated into existing fiber optic applications. Theoretical investigations to remedy this are ongoing at institutions such as MIT (B. Little and H. Haus) with tapered fibers [27], while experiments continue with existing coupling methods. Planar single mode waveguide coupling has been investigated by Arnold and Griffel's groups at the Polytechnic Univ. of New York [28], and more recently by MIT using silica integrated optical waveguides known as SPARROWS [29]. The most successful of these methods experimentally are the silica fiber taper with efficiency up to 99.8% ([30] and [31]), the angle polished silica fiber coupler of Maleki's group at JPL with an efficiency $\sim 60\%$ [32], and the prism coupler at Moscow State University with efficiency $\sim 78\%$ [33]. Prism couplers are the most robust, and easiest to align. However, as will be mentioned in Chapter 3, standard flat prisms theoretically cannot have 100% coupling. Therefore, to make these couplers commercially practical an added manufacturing process to shape the coupling interface of the prism would be necessary. Angle polished silica fiber couplers have a fixed geometry, and therefore no method to vary the coupling constant to achieve efficient coupling. Tapered fibers have very good coupling efficiency, and an ability to change the coupling constant by moving the point of contact of the sphere with respect to the taper position. However, these tapered fibers typically have diameters less than $10\ \mu\text{m}$, and therefore alignment, and stability in any commercial packaging scheme is questionable. Recent experimental

results using waveguide couplers in silica have claimed power extraction of 95% into a high- Q optical mode (although no insertion loss numbers were given) [34]. In addition, work had been done on a dual coupler, wavelength drop device which demonstrates coupling into one waveguide port, and out another with 55 % power transfer [35]. This work is still in its early stages, however the robustness and practical commercial possibilities for this coupling method lends hope to future commercial realization of microsphere products.

As will be shown in Chapter 3, both tapered silica fiber couplers and angle polished silica fibers couplers would have a significantly lower efficiency if used for coupling light into LiNbO₃ disks. This is a result of the high index of refraction ($n = 2.1$) of the disk compared to silica ($n = 1.5$). In the absence of high index fibers designed for efficient coupling to LiNbO₃, these coupling methods are unlikely candidates for the microphotonic modulator.

1.3.4 Passive ring and disk shaped waveguide resonators

Small resonant waveguide based disk or ring cavities have been explored for use in photonic signal routing and processing. Microring waveguide resonators are currently being pursued to serve as building blocks for integration of wavelength division multiplexing (WDM) components [36]. Specifically wavelength switching, routing [37], and filtering are the main current focus of research. The lead work is

being done by Little and Haus at MIT. Mode coupling analysis of multipole filters have been investigated theoretically [38], and channel add drop filters have been fabricated [39]. Theoretical work in possible geometries for active coupling for waveguide resonators is currently being developed for optical switching, routing, and modulation by Yariv's group at Cal. Tech [40]. Possible material systems or experimental paths forward have not yet been suggested. Finally, some proof of concept work has been done in polymer based ring waveguides showing relatively low loss material at $1.3 \mu\text{m}$ ($Q \sim 10^5$ or 0.1 dB/cm) [41]. The information that seems to be missing in almost all the papers written on this topic is insertion loss. Although research should continue in this area, solving the insertion loss problem should be a high priority. Without low insertion loss, large scale WDM integration is unlikely.

1.3.5 Active ring and disk shaped microlaser cavities

Optical resonators with passive Q greater than 10^4 have been demonstrated in semiconductor microdisks of $0.9 \mu\text{m}$ radius [42]. In addition, the high optical confinement and high- Q of resonant modes, even for small diameter disks, makes this geometry suitable for microlaser cavities. Initial work on the design and fabrication of multi-quantum well microdisk lasers focused on reducing the size of these photonic devices [43]. Figure 7(a) shows a microdisk laser with radius $R = 0.8 \mu\text{m}$ and lasing wavelength $\lambda \approx 1.5 \mu\text{m}$ [44]. Detailed studies and modeling of these

active optical devices have revealed much of the physics governing device operation [45].

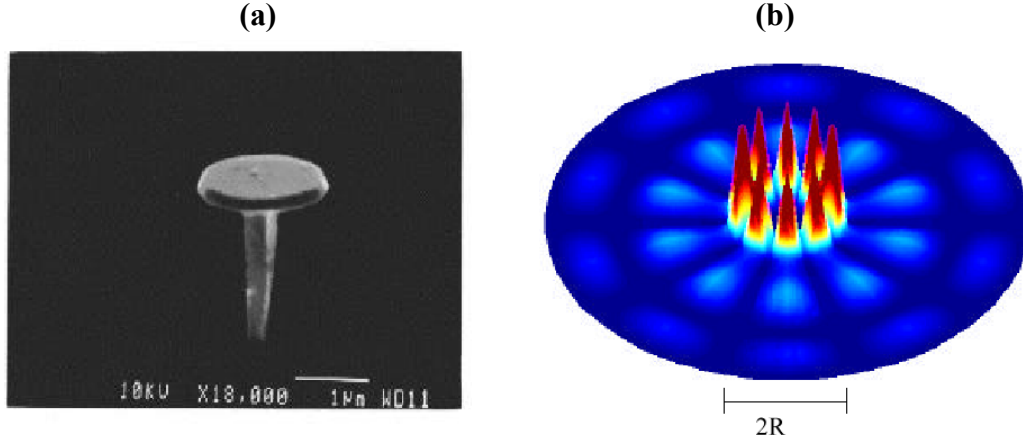


Figure 7. (a) Scanning electron microscope image of an InGaAs/InGaAsP multiple quantum well whispering gallery mode microdisk laser with radius $R = 0.8 \mu\text{m}$ and thickness $L = 0.22 \mu\text{m}$. The $1 \mu\text{m}$ bar provides a scale. (b) Results of simulating the electromagnetic field intensity of a $M = 5$, $N = 1$, resonance for a microdisk similar to that shown in (a) with radius $R \sim M\lambda/2\pi n_{\text{eff}}$, where λ is the resonance wavelength and n_{eff} is the effective refractive index.

Figure 7(b) shows results of calculating the photon field intensity for the $M = 5$, $N = 1$, lasing mode of the structure in (a). Continuous room-temperature operation of optically [46] and electrically [47] driven microdisk lasers have also been achieved. The realization of lasing in optically active microdisk resonators opens up the possibility for future opto-electronic signal-processing functions on a single chip. Appropriate RF-to-optical conversion device technologies such as the microphotonic resonator may contribute to any potential vision of RF signal-processing. However, the inability to couple a significant amount of light out of microdisk lasers hamper efforts to truly investigate the usefulness of this device.

1.3.6 Conventional optical modulators

The advantages of the microphotonic modulator is easily seen by a comparison to the conventional optical modulators. Direct current modulation of semiconductor injection lasers typically is restricted from the *mm*-wave domain by technological limitations. High-speed modulation is therefore typically limited to integrated optical waveguide technologies using electro-optic materials. Polymer electro-optic devices are still too technologically immature to be commercially feasible [48]. LiNbO₃ is the dominant electro-optic material in the marketplace, with Mach-Zehnder (MZ) interferometric optical modulators achieving bandwidths of 10's of GHz with V_π in the 5 - 6 V range [49].

Ti:LiNbO₃ waveguide fabrication is achieved through photolithographic patterning and deposition of a Titanium dopant metal on a LiNbO₃ substrate. Titanium indiffusion is carried out in a furnace at temperatures of ~1000 °C for several hours. After diffusion, SiO₂ buffer layers are deposited for phase matching and reduction of optical attenuation from metal electrodes. Metal electrode patterning and end face preparation (polishing and AR coating) follow.

These devices are phase-velocity matched along a typically 2 cm length and 50 Ω terminated. Termination results in a power consumption of 0.5 W, while walkoff of the electrical and optical waves and electrical attenuation limit bandwidth

performance. Typical electrode geometries have approximately 30% optical field overlap with fringing non-uniform RF electric fields [50].

The 2 *cm* length, large power consumption, small field overlap, and large V_π make it evident that conventional LiNbO₃ MZ optical modulators are of no practical use for lightweight compact receiver architectures. In comparison, the microphotonic modulator architecture has the potential promise of 1 μW sensitivity, large optical / RF field overlap, and *mm* dimensions.

1.3.7 Resonant Fabry-Perot modulators and comb generators

Optical frequency comb generators (OFCG) are usually based on optical modulators placed inside a Fabry-Perot (FP) cavity [51]. Ho and Kahn used a single arm LiNbO₃ phase modulator in the path of a single optically amplified loop which is a lossy bulk version of the LiNbO₃ microphotonic resonator [52]. I discuss them because the LiNbO₃ microresonator is essentially a modulator inside a disk cavity. Therefore the physics are similar. OFCG are generally targeted toward measurement of absolute frequency standards, and optical wavelength division multiplexing. OFCG's typically result in a comb of frequencies, which are integral multiples of the cavity free spectral range. Comb generators differ from our research in that they are driven with large voltages in a very non-linear region of the modulator. Therefore the non-linearities seen in OFCG's are much larger than what is expected in our

modulator. This research points out that the non-linear response of the microphotonic resonator is not insignificant, and must be investigated.

Bulk RF electrically resonant FP optical modulators are commercially available [53]. These modulators use resonant tank circuits (RF microwave cavities) to maximize RF power transfer to a bulk electro-optic LiNbO₃ material. Frequencies of operation for New Focus models can be mechanically tuned from 0.5 to 4.6 GHz with 2-4% RF resonant bandwidths ($Q = 50$), or fixed at 9.2 GHz. The lack of optical resonance requires a long optical interaction length, and therefore an increase in operational RF frequency is probably limited by the bulk size of the crystal.

1.4 Thesis Organization

This thesis is divided into 5 chapters as follow:

Chapter 1 Introduction: This chapter provides the thesis motivation, and thesis question. I also include a brief discussion of work related to this proposal.

Chapter 2 LiNbO₃ microphotonic modulator design and fabrication: A discussion of the material properties of LiNbO₃, and an introduction to the fabrication of optical and RF electrical coupling schemes.

Chapter 3 Passive LiNbO₃ microphotonic modulator: The passive physics of the resonator are introduced. Experimental results of optical spectra, optical pulse

response, and optical coupling are presented. Electrical material properties are presented.

Chapter 4 LiNbO₃ microphotonic modulator: Theory and experimental results are presented for base-band electrical modulation of the modulator. Theory, simulation and experimental results extending modulation to *mm*-waves are also shown. In addition, system efficiencies are discussed.

Chapter 5 Conclusion: This chapter summarizes the results presented, and directions for future research are outlined.

Appendix A Microwave band designations: This appendix is provided to clarify published RF band designations.

1.5 References

- [1] Ohata, K., Inoue, T., Funabashi, M., Inoue, A., Takimoto, Y., Kuwabara, T., Shinozaki, S., Maruhashi, K., Hosaya, K., and Nagai, H.: ‘Sixty-GHz-Band Ultra-Miniature Monolithic T/R Modules for Multimedia Wireless Communication Systems’, IEEE Trans. Microwave Theory Techn., 1996, **44**, pp. 2354-2360
- [2] Gargione, F. and Iida T.: ‘Services, technologies, and systems at *Ka* band and beyond – a survey’, IEEE J. Select. Areas Commun., 1999, **17**, (2), pp. 225-229
- [3] Tien, P.K., Ulrich, R.: ‘Theory of Prism-Film Coupler and Thin-Film Light Guides’, J. Opt. Soc. Am., 1970, **60**, pp. 1325-1337
- [4] Lord Rayleigh (J. W. Strutt): ‘The problem of the whispering gallery’, Phil. Mag., 1910, **20**, pp. 1001-1004
- [5] Wait, J. R.: ‘Electromagnetic whispering-gallery modes in a dielectric rod’, 1967, Radio Sci., **14**, (9), pp. 1005-1017

- [6] Gayral, B., Gérard, J. M., Lemaître, A., Dupuis, C., Manin, L., and Pelouard, J. L.: 'High-Q wet-etched GaAs microdisks containing InAs quantum boxes', *Appl. Phys. Lett.*, 1999, **75**, pp. 1908-1910
- [7] Vedrenne, C., and Arnaud, J.: 'Whispering-gallery modes of dielectric resonators', *Proc. Inst. Elec. Eng. pt. H*, 1982, **129**, pp. 183-187
- [8] Gorodetsky, M. L.; Savchenkov, A. A.; and Ilchenko, V. S.: 'Ultimate Q of optical microsphere resonators' *Opt. Lett.*, 1996, **21**, pp. 453-455
- [9] Hill, S.C., and Benner, R.E.: 'Optical Effects Associated With Small Particles', (World Scientific, Singapore, 1988), pp. 182-195
- [10] Braginsky, V. B.; Gorodetsky, M. L.; and Ilchenko, V. S.: *Sov. Phys. Dokl.*, 1987, **32**, pp. 306-309
- [11] Braginsky, V. B.; Gorodetsky, M. L.; and Ilchenko, V. S.: 'Quality-factor and nonlinear properties of optical whispering-gallery modes', *Phys. Lett. A*, 1989, **137**, pp. 393-395
- [12] Collot, L.; Lefevre-Seguin, V.; Brune, M.; Raimond, J. M.; and Haroche, S.: *Europhys. Lett.*, 1993, **23**, pp. 327-334
- [13] Cai, M., Hedekvist, P. O., Bhardwaj, A., and Vahala, K.: '5-Gbit/s BER performance on an all fiber-optic add/drop device based on a taper-resonator-taper structure', *IEEE Photon. Tech. Lett.*, 2000, **12**, (9), pp. 1177-1187
- [14] Cai, M., Hunziker, G., and Vahala, K.: 'Fiber-optic add-drop device based on a silica microsphere-whispering gallery mode system', *IEEE Photon. Tech. Lett.*, 1999, **11**, pp. 686-687
- [15] Ilchenko, V. S.; Yao, X. S.; and Maleki, L.: 'Pigtailling the high-Q microsphere cavity: a simple fiber coupler for optical whispering-gallery modes', *Optics Lett.*, 1999, **24**, pp. 723-725
- [16] Gorodetsky, M. L. and Ilchenko, V. S.: 'High-Q optical whispering-gallery microresonators: precession approach for spherical mode analysis and emission patterns with prism couplers', *Opt. Comm.*, 1994, **113**, pp. 133-143
- [17] Treussart, F.; Hare, J.; Collot, L.; Lefevre, V.; Weiss, D. S.; Sandoghdar, V.; Raimond, J. M.; and Haroche, S.: 'Quantized atom-field force at the surface of a microsphere', *Opt. Lett.*, 1994, **19**, pp. 1651-1693

- [18] Mabuchi, H. and Kimble, H. J.: ‘Atom galleries for whispering atoms: binding atoms in stable orbits around an optical resonator’, *Opt. Lett.*, 1994, **19**, pp. 749-751
- [19] Cai, M., Hedekvist, P. O., Bhardwaj, A., and Vahala, K.: ‘5-Gbit/s BER performance on an all fiber-optic add/drop device based on a taper-resonator-taper structure’, *IEEE Photon. Tech. Lett.*, 2000, **12**, pp. 1177-1178
- [20] Hecht, J.: ‘Long-haul DWDM systems go the distance’, *Laser Focus World*, 2000, **36**, (10), pp. 23-28
- [21] Vassiliev, V. V.; Velichansky, V. L.; Ilchenko, V. S.; Gorodetsky, M. L.; Hollberg, L.; and Yarovitsky, A. V., ‘Narrow-line-width diode laser with a high-Q microsphere resonator’, *Opt. Comm.*, 1998, **158**, pp. 305-312
- [22] Sandoghdar, V.; Treussart, F.; Hare, J.; Lefevre-Seguin, V.; Raimond, J. M.; and Haroche, S.: ‘Very low threshold whispering-gallery-mode microsphere laser’, *Phys. Rev. A*, 1996, **54**, pp. 1777-1780
- [23] Ilchenko, V. S., Volikov, P. S., Velichansky, V. L., Treussart, F., Lefevre-Seguin, V., Raimond, J. M., and Haroche, S.: ‘Strain-tunable high-Q optical microsphere resonator’, *Opt. Comm.*, 1998, **145**, pp. 86-90
- [24] Rosenberger, A. T., and Rezac, J. P.: ‘Evanescent wave sensor using microsphere whispering-gallery modes’, *Proc. SPIE*, 2000, **3930**, pp. 186-187
- [25] McKinley, M. C., Smith Jr., C. V., Nunnally, W. C., Magnusson, R., and Black, T. D.: ‘Laser interference figure measurement of 60 Hz high voltages using a LiNbO₃ spherical electrooptic sensor’, *IEEE Photon. Tech. Lett.*, 1990, **2**, (6), pp. 447-449
- [26] McKinley, M. C., Smith Jr., C. V., Nunnally, W. C., Magnusson, R., and Black, T. D.: ‘A spherical electro-optic high-voltage sensor’, *Pulsed Power Conference*, 1989, **7**, pp. 380 – 383
- [27] Little, B. E.; Laine, J. P.; and Haus, H. A.: ‘Analytic theory of coupling from tapered fibers and half-blocks into microsphere resonators’, *IEEE J. Lightwave Tech.*, 1999, **17**, pp. 704-715
- [28] Serpenguzel, A.; Arnold, S.; and Griffel, G.: ‘Excitation of resonances of microspheres on an optical fiber’ *Opt. Lett.*, 1995, **20**, pp. 654- 656

- [29] Little, B. E., Laine, J. P., Lim, D. R., Haus, H. A., Kimerling, L. C., and Chu, S. T.: ‘Pedestal antiresonant reflecting waveguides for robust coupling to microsphere resonators and for microphotonic circuits’, *Optics Letters*, 2000, **25**, (1), pp. 152-153
- [30] Knight, J. C.; Cheung, G.; Jacques, F.; and Birks, T. A.: ‘Phase-matched excitation of whispering-gallery-mode resonances by a fiber taper’, *Opt. Lett.*, 1997, **15**, pp. 1129-1131
- [31] Cai, M., and Vahala, K.: ‘Highly efficient optical power transfer to whispering-gallery modes by use of a symmetrical dual-coupling configuration’, *Opt. Lett.*, 2000, **25**, (4), pp. 260-262
- [32] Ilchenko, V. S.; Yao, X. S.; and Maleki, L.: ‘Pigtailling the high-Q microsphere cavity: a simple fiber coupler for optical whispering-gallery modes’, *Opt. Lett.*, 1999, **24**, pp. 723-725
- [33] Gorodetsky, M. L.; and Ilchenko, V. S.: ‘Optical microsphere resonators: optimal coupling to high-Q whispering-gallery modes’, *J. Opt. Soc. Am. B.*, 1999, **16**, pp. 147-154
- [34] Laine, J. P., Little, B. E., Lim, D. R., Tapalian, H. C., Kimerling, L. C., and Haus, H. A.: ‘Microsphere resonator mode characterization by pedestal antiresonant reflecting waveguide coupler’, *IEEE Photon. Tech. Lett.*, 2000, **12**, (8), pp. 567-569
- [35] Laine, J. P., Little, B. E., Lim, D. R., Tapalian, H. C., Kimerling, L. C., and Haus, H. A.: ‘Planar integrated wavelength-drop device based on pedestal antiresonant reflecting waveguides and high- Q silica microspheres’, *Opt. Lett.*, 2000, **25**, (22), pp. 1225-1234
- [36] Hryniewicz, J. V.; Absil, P. P.; Little, B. E.; Wilson, R. A.; and Ho, P. T.: ‘Higher order filter response in coupled microring resonators’, *IEEE Photon. Tech. Lett.*, 1999, **12**, pp. 320-322
- [37] Little, B. E.; Haus, H. A.; Foresi, J. S.; Kimerling, L. C.; Ippen, E. P.; and Ripin, D.: ‘Wavelength switching and routing using absorption and resonance’, *IEEE Photon. Tech. Lett.*, 1998, **10**, pp. 816-818
- [38] Khan, M. J.; Manolatou, C.; Shanhui, F.; Villeneuve, P. R.; Haus, H. A.; and Joannopoulos, J. D.: ‘Mode-coupling analysis of multipole symmetric resonant add/drop filters’ *IEEE J. Quan. El.*, 1999, **35**, pp. 1451-1460

- [39] Chu, S. T.; Pan, W.; Suzuki, S.; Little, B. E.; Sato, S.; and Kokubun, Y.: 'Temperature insensitive vertically coupled microring resonator add/drop filters by means of a polymer overlay', *IEEE Photon. Tech. Lett.*, 1999, **11**, pp. 1138-1140
- [40] Yariv, A.: 'Voltage controlled micro cavity-waveguide coupling for switching, routing, and modulation of optical waves', *Darpa/MTO workshop*, 2000, pp. 56-68
- [41] Hida, Y., Imamura, S., and Izawa, T.: 'Ring Resonator Composed of low loss polymer waveguides at 1.3 μm ', *Electron. Lett.*, 1994, **28**, (14), pp. 1314-1316
- [42] Gayral, B., Gerard, J. M., Lamaitre, A., Dupuis, C., Manin, L., and Pelouard, J. L.: 'High Q wet-etched GaAs microdisks containing InAs quantum boxes', *Appl. Phys. Lett.*, 1999, **75**, pp. 1908-1910
- [43] McCall, S. L., Levi, A. F. J., Slusher, R. E., Pearton, S. J., and Logan, R. A.: 'Whispering mode microdisk lasers', *Appl. Phys. Lett.*, 1992, **60**, pp. 289-291
- [44] Levi, A. F. J.; McCall, S. L.; Pearton, S. J.; and Logan, R. A.: 'Room temperature operation of submicrometre radius disk laser' *Electron. Lett.*, 1993, **29**, pp. 1666-1667
- [45] Frateschi, N. C.; and Levi, A. F. J.: 'The spectrum of microdisk lasers', *J. Appl. Phys.*, 1996, **80**, pp. 644-653
- [46] Thiagarajan, S. M. K.; Levi, A. F. J.; Lin, C. K.; Kim, I.; Dapkus, P. D.; and Pearton, S. J.: 'Continuous room-temperature operation of optically pumped InGaAs/InGaAsP microdisk lasers' *Electron. Lett.*, 1998, **34**, pp. 2333-2334
- [47] Thiagarajan, S. M. K.; Cohen, D. A.; Levi, A. F. J.; Ryu, S.; Li, R.; and Dapkus, P. D.: 'Continuous room-temperature operation of microdisk laser diodes', *Electron. Lett.*, 1999, **35**, pp. 1252-1254
- [48] Steier, W. H., Chen, A., Lee, S., Garner, S., Zhang, H., Chuyanov, V., Dalton, L. R., Wang, F., Ren, A. S., Zhang, C., Todorova, G., Harper, A., Fetterman, H. R., Chen, D., Udupa, A., Bhattacharya, D., and Tsap, B.: 'Polymer electro-optic devices for integrated optics', *Chemical Physics*, 1999, **245**, pp. 487-506
- [49] Noguchi, K., Mitomi, O., and Miyazawa, H.: 'Millimeter-wave Ti:LiNbO₃/optical modulators', *J. Lightwave Tech.*, 1998, **16**, pp. 615-619

- [50] Korotky, S. K., and Alferness, R. C.: 'Integrated optical circuits and components', (Marcel Dekker, Inc., New York, 1987), ISBN 8-8247-7575-9
- [51] Saitoh, T.; Kouroggi, M.; and Ohtsu, M.: 'A waveguide-type optical-frequency comb generator' IEEE Photon. Tech. Lett., 1995, 7, pp. 197-199
- [52] Ho, K. P., and Kahn, J. M.: 'Optical frequency comb generator using phase modulation in amplified circulating loop', IEEE Photon. Tech. Lett., 1993, 5, (6), pp. 254-256
- [53] New Focus Corp., available at <http://www.newfocus.com>

Chapter 2

LiNbO₃ microphotonic modulator design and fabrication

2.1 Introduction

Conventional Mach-Zehnder LiNbO₃ amplitude modulators are typically composed of two 2 *cm* long Ti-indiffused optical waveguide arms fabricated in a LiNbO₃ wafer. Phase-matched 50 Ω coplaner electrodes are used to maximize overlap of the optical and RF electric fields. As shown in Figure 8, the basic LiNbO₃ microphotonic modulator also uses a Mach-Zehnder configuration with the distinction that the single pass active arm of the conventional modulator is replaced by a multiple-pass optically resonant disk geometry. Light is coupled to the disk by means of evanescent coupling. Methods of RF electric field coupling will be discussed later in this chapter.

The ability to fabricate the LiNbO₃ microphotonic resonator introduces four significant challenges. (a) Understanding the advantages and limitations of bulk

LiNbO₃ must be first be achieved. (b) Polishing optically flat surfaces from LiNbO₃ is a standard industrial procedure. However, polishing curved sidewalls to an optical finish in LiNbO₃ is not standard practice, and practical fabrication methods must be developed. (c) Geometries needed to couple electric fields into the resonator must also be explored. Maximum overlap of the electrical and optical field is desired to use the electro-optic effect to its fullest. (d) In addition, high optical efficiency from the evanescent coupling of laser light into the optical cavity must be achieved for this device to be significant component for future RF-photonic systems.

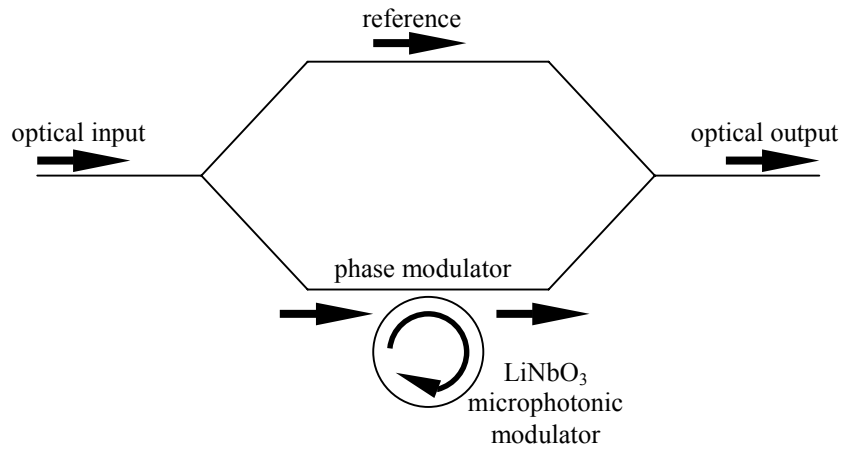


Figure 8. Basic LiNbO₃ microphotonic modulator geometry. The active arm of this Mach-Zehnder geometry provides optical phase shifts by way of an optically resonant electro-optic LiNbO₃ disk, while the passive reference arm converts optical phase modulation to amplitude modulation.

2.2 Material properties

The components to be developed are fabricated from the crystalline LiNbO₃ material system because of its high electro-optic coefficient, and its low loss at both optical and RF frequencies. LiNbO₃ is widely used as a frequency doubler for wavelengths

$> 1 \mu\text{m}$, optical parametric oscillator (OPO), electro-optic Q -switch, optical phase modulator, piezoelectric transducer, and for surface acoustic wave (SAW) devices ([54], [55], and [56]). Because of this variety of practical and commercialized applications LiNbO_3 has become a very mature material system.

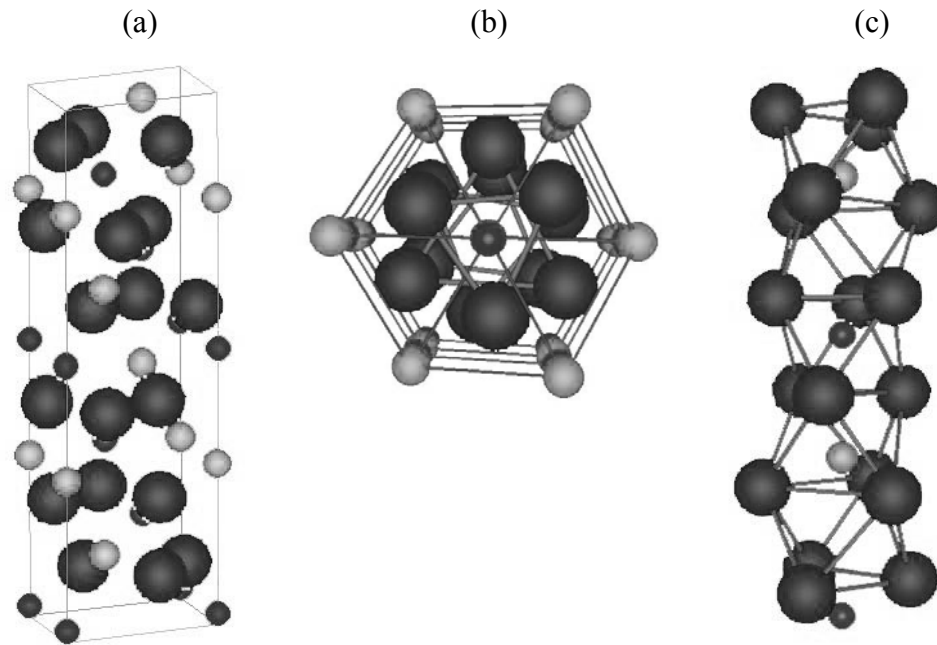


Figure 9. LiNbO_3 molecular structure. Niobium atoms are represented as dark gray small spheres, Lithium as light gray small spheres and Oxygen as large spheres. (a) Vertical view of the LiNbO_3 conventional hexagonal unit cell. (b) View along c (or z) axis. (c) Octahedral oxygen structure of LiNbO_3 [60].

In an isotropic medium, the induced polarization is related to the applied electric field by a scalar susceptibility. In an anisotropic media such as LiNbO_3 , the induced polarization will depend on the magnitude and direction of the applied field. This is because the crystal is made of a periodic array of atoms arranged in a certain symmetry as shown for LiNbO_3 in Figure 9. At temperatures below its ferroelectric

Curie temperature ($\sim 1210^\circ\text{C}$), LiNbO_3 is a negative uniaxial ferroelectric crystal with a crystal symmetry of the trigonal $3m$ point group and $R3c$ space group [59].

An applied electric field changes the distribution of charge in the crystal (possibly including a slight deformation of the ion lattice) thereby changing the susceptibility. In such an anisotropic media, the susceptibility is denoted as a tensor. The largest effect is the linear electro-optic change of refractive index in noncentrosymmetric crystals. In LiNbO_3 the index of refraction along the extraordinary axis (z -axis) is $n_e = 2.138$, and along the ordinary axes $n_o = 2.21$ at an optical wavelength $\lambda = 1.55 \mu\text{m}$. The electro-optic effect in LiNbO_3 for electric field $E(z)$ along the crystal's z -axis is $\Delta n_z = n_e^3 r(33)E(z)/2$, where $r(33) \sim 30.8 \times 10^{-12} \text{ m/V}$, and $\Delta n_{x,y} = n_o^3 r(13)E(z)/2$, where $r(13) \sim 8.6 \times 10^{-12} \text{ m/V}$. The ratio $\Delta n/\Delta E(z)$ is therefore 3.24 times larger for light polarized along the z -axis compared to light polarized in the x - y plane, and in addition, the electric field does not change the orientation of the principle axes of the crystal. It should also be noted that the refractive index differs significantly between optical and RF frequencies. This difference may be exploited to obtain simultaneous resonance between optical and RF fields inside the disk. Other properties for bulk LiNbO_3 are summarized in Table 1.

It should also be mentioned that at low frequencies ($< 40 \text{ MHz}$) LiNbO_3 is a very good material for acoustic wave applications such as SAW and transducer devices

[54]. These waves may be problematic if one were to use this material as a modulator at these low frequencies. However, in this thesis frequencies of interest are at tens of *GHz* where acoustic waves are too lossy to propagate.

Table 1 Bulk properties of LiNbO₃ ([57], [58], and [59]).

Property	Value	Notes
Optical index or refraction (o-axis)	2.21	at $\lambda = 1.55 \mu m$
Optical index of refraction (e-axis)	2.14	at $\lambda = 1.55 \mu m$
RF dielectric coefficient (o-axis)	42.5	\approx constant from 100 MHz to 140 GHz
RF dielectric coefficient (e-axis)	26	\approx constant from 100 MHz to 140 GHz
RF refractive index (o-axis)	6.5	\approx constant from 100 MHz to 140 GHz
RF refractive index (e-axis)	5.1	\approx constant from 100 MHz to 140 GHz
Electrical conductivity	$1 \times 10^{-18} \text{ } 1/\Omega\text{-cm}$	at DC
Thermal conductivity	$5.6 \text{ } W/m^{\circ}C$	
Thermal expansion (o-axis)	$14 \times 10^{-6} \text{ } ^{\circ}C^{-1}$	
Thermal expansion (e-axis)	$4 \times 10^{-6} \text{ } ^{\circ}C^{-1}$	
Thermal effect on index (o-axis)	$1.85 \times 10^{-6} \text{ } ^{\circ}C^{-1}$	$1/n_o \text{ } dn_o/dT$
Thermal effect on index (e-axis)	$1.60 \times 10^{-6} \text{ } ^{\circ}C^{-1}$	$1/n_e \text{ } dn_e/dT$
Melting point	$1253 \text{ } ^{\circ}C$	
Density	$4.635 \text{ } g/cm^3$	
Band gap	$4 \text{ } eV$	
Electro-optic coefficient	$r_{33} = 30.8 \text{ } pm/V$ $r_{13} = 8.6 \text{ } pm/V$ $r_{22} = 3.4 \text{ } pm/V$ $r_{51} = 28.0 \text{ } pm/V$	$r_{ij} = \begin{pmatrix} 0 & -r_{22} & r_{13} \\ 0 & r_{22} & r_{13} \\ 0 & 0 & r_{33} \\ 0 & r_{51} & 0 \\ r_{51} & 0 & 0 \\ -r_{22} & 0 & 0 \end{pmatrix}$
Nonlinear electro-optic coefficient	$d_{31} = 11.6$ $d_{33} = 86.0$ $d_{22} = 5.6$	defined as $d_{ij}/d_{36 \text{ KDP}}$
Piezoelectric strain coefficient	$d_{15} = 69.20 \text{ } pm/V$ $d_{22} = 20.80 \text{ } pm/V$ $d_{31} = -0.85 \text{ } pm/V$ $d_{33} = 6.00 \text{ } pm/V$	$d_{ij} = \begin{pmatrix} 0 & 0 & 0 & 0 & d_{15} & -d_{22} \\ -d_{22} & d_{22} & 0 & d_{15} & 0 & 0 \\ d_{31} & d_{31} & d_{33} & 0 & 0 & 0 \end{pmatrix}$

2.3 Microphotonic optical resonator fabrication

Disk resonator geometry and polishing technique play an important role in determining optical Q and optical coupling. The optical resonators are fabricated from disk shaped z -cut LiNbO_3 . As shown in Figure 10(a), the basic geometry of the LiNbO_3 resonator is a disk of radius R , where $1 \text{ mm} \leq R \leq 3 \text{ mm}$, and thickness d , where $0.2 \text{ mm} \leq d \leq 1 \text{ mm}$ for devices presently under test. The side-wall of the disk is optically polished with a radius of curvature, R' , typically equal to the radius of the disk. In addition, the equator of the disk's curved side-wall should be accurately maintained at height $d/2$.

While polishing optically flat surfaces with LiNbO_3 is a routine industrial procedure, polishing curved sidewalls to an optical finish in LiNbO_3 is not a standard practice. Figure 10(b) is a photograph of a $R = 4 \text{ mm}$, $d = 3.6 \text{ mm}$ disk which clearly shows the optically polished curved sidewalls of the disk. Figure 10(c) shows a smaller $R = 1 \text{ mm}$, $d = 200 \text{ }\mu\text{m}$ thick z -cut LiNbO_3 disk prior to metalization. As will be discussed later, optical Q in excess of 4×10^6 near $\lambda = 1550 \text{ nm}$ wavelength is measured in high quality disks.

Polishing of the resonator is achieved by first thinning the disk to the desired thickness by a series of $30 \text{ }\mu\text{m}$ and $5 \text{ }\mu\text{m}$ grit Alumina powder. The sidewalls are

then shaped to the desired curvature using a sequence of $30\ \mu\text{m}$, $9\ \mu\text{m}$, and $5\ \mu\text{m}$ Alumina powder. Optical polish is achieved using $2.5\ \mu\text{m}$ Cerium Oxide powder.

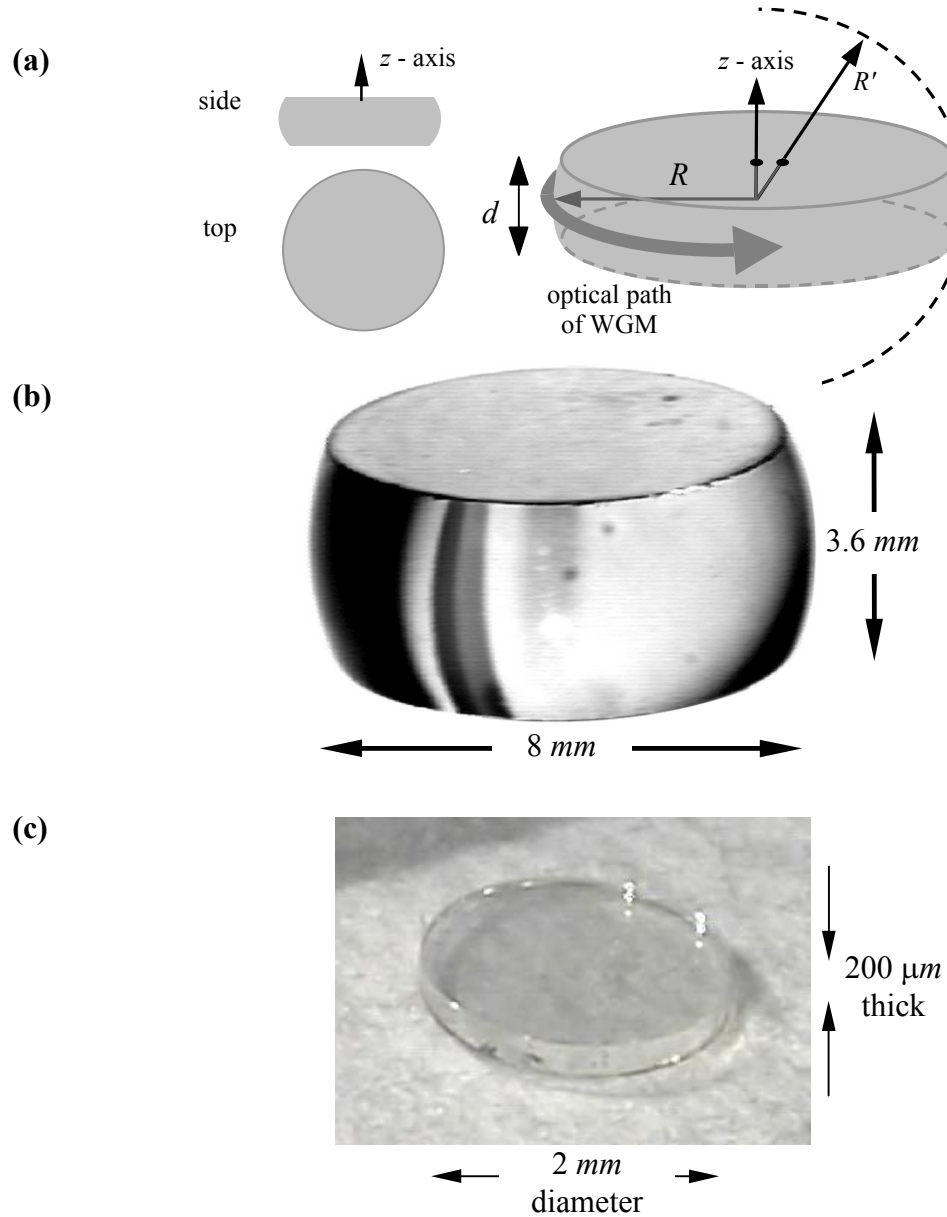


Figure 10. (a) Sketch of the geometry of a microdisk indicating disk radius R , disk thickness d and curved side-walls with radius of curvature R' . (b) Photograph of a large z -cut LiNbO_3 disk-shaped resonator with solid-gold top and bottom flat-electrodes and optically-polished curved side-walls. The size of the disk is indicated. (c) Photograph of a small z -cut LiNbO_3 disk-shaped resonator. The size of the disk is indicated.

The quality of the sidewall polish is evaluated by observation through an optical microscope with a 150× objective and Nymarsky optics. No surface roughness could be seen along the disk equator. Measurements of optical Q confirm the quality of the polish.

2.4 Optical coupling

A significant challenge in the development of an optical resonator-based system is zero-loss coupling of optical power both into and out of the resonator. This must be achieved to reduce coupling losses that are inherent in other systems such as conventional Mach-Zehnder LiNbO₃ modulators. Optical whispering gallery modes cannot be excited directly by simple propagating beams. Instead, coupling is achieved through indirect excitation of the whispering gallery modes using evanescent fields. There are numerous methods for evanescent coupling of light into guided modes as discussed in Section 1.3.3, however prism coupling is particularly convenient because of the large refractive index of LiNbO₃. Basic prism-coupled optical configurations are shown schematically in Figure 11.

The mechanism for coupling between prisms of index n_{prism} and disks with index n_{opt} is that of frustrated total internal reflection. Light at a wavelength λ incident on the coupling face of a prism at an angle θ_{prism} with respect to the normal (where θ_{prism} is greater than the critical angle) is totally internally reflected. An evanescent field

extends beyond the prism face and into the coupling region with a skin depth δ given by

$$\delta = \lambda \cdot \cos(\theta) / \sqrt{4 \cdot \pi^2 (n_{prism}^2 \sin^2(\theta) - 1)}$$

with a value typically around 100 nm at a wavelength of 1.55 μm [61]. Therefore the higher the prism index of refraction, the more tightly confined the light will be to the face of the prism.

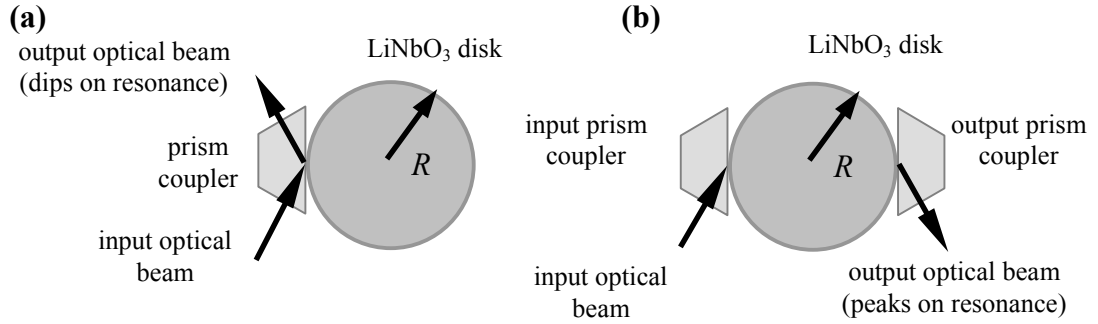


Figure 11. Sketch showing (a) single prism-coupling and (b) two prism-coupling of the optical field to the microphotonic resonator

The prominent component of the propagation constant β_{nlm} for whispering gallery modes lies along the annulus of the disk for the high- Q modes we are interested in exciting [62][63]. To phase match with these modes, the angle of incidence of light with respect to the normal of the coupling face should be at an angle greater than or equal to $\theta_{prism} = \arcsin(n_{opt} / n_{prism})$. This is fundamentally a result of Snell's law and results in the requirement that $n_{prism} \geq n_{opt}$. If two materials of refractive index n_{prism} and n_{opt} are placed in intimate contact as shown in Figure 12(a), the light refracts at

some angle θ_{opt} given by Snell's law $\theta_{opt} = \arcsin (n_{prism} \sin \theta_{prism} / n_{opt})$. In the case of a plane wave, the insertion of an air gap between these two materials has no effect on the value of this refracted angle (Figure 12(b)). Our goal is to improve the overlap of the input optical beam with the WGM that has propagation constants along the annulus of the disk edge. We therefore require that θ_{opt} be 90 degrees, or $\theta_{prism} = \arcsin (n_{opt} / n_{prism})$.

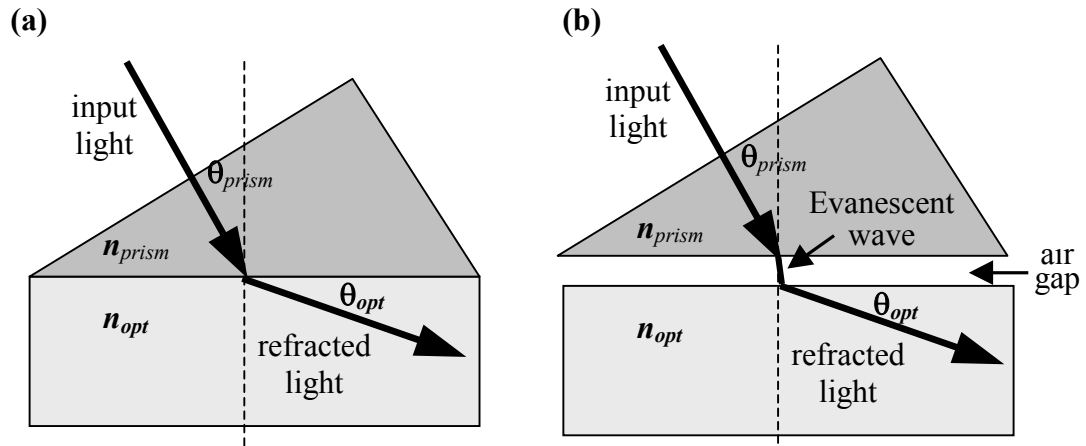


Figure 12 Schematic representation of prism coupling by FTIR. (a) Materials of refractive index n_{prism} and n_{opt} in intimate contact. (b) Materials of refractive index n_{prism} and n_{opt} with air gap.

The factors found by experiment to have most influence on optical coupling are the input beam's spatial profile and the shape of the coupling gap. Both theoretically and experimentally, there exists an optimum gap shape where prism coupling of Gaussian beams into planar waveguides can achieve close to 100% coupling efficiency [64]. Experiments show that a linearly tapered gap, as a first approximation to the optimum gap shape, resulted in up to 88% coupling efficiency.

Using cylindrically shaped prisms as a better approximation to the theoretically optimized gap shape, 92% efficiencies were obtained (see Figure 13) [65]. Therefore, optical throughput can be improved by modifying or adding optical elements to critically couple the optical input beam to the disk resonance.

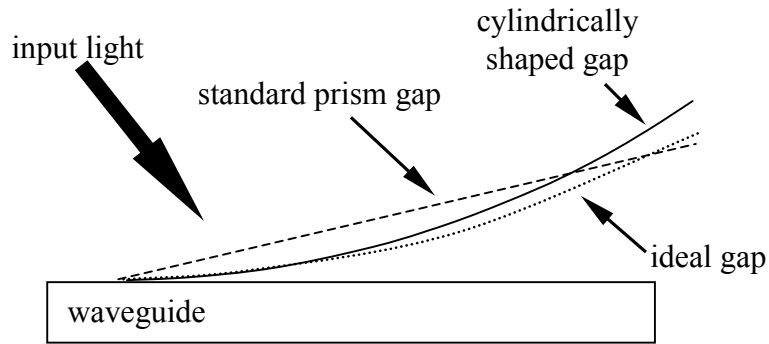


Figure 13. Cylindrically shaped prisms have been shown to increase coupling. Above we show a standard flat prism gap, cylindrically shaped gap, and ideal prism gap needed to have 100% coupling.

2.5 Electrical coupling to the microphotonic modulator

An important advantage to the LiNbO_3 microresonator is the ability to significantly overlap the optical and electromagnetic fields inside the disk. The WGM nature of the optical field strongly confines light to the edge of the disk. We can improve sensitivity by tailoring the RF excitation to overlap with this edge. Methods used to couple RF electric fields to the dielectric disk were lithographic patterning and e-beam evaporating of metal electrodes directly on the disk, placing small metal electrodes directly on the LiNbO_3 disk as a component in a resonant RF circuit, and placing the dielectric resonator in a metal-walled RF cavity.

2.5.1 Patterned metal electrodes

One method to couple the electric field detected at the RF antenna to the microphotonic modulator is lithographic patterning followed by e-beam deposition of metal electrodes onto the LiNbO_3 disk. These electrodes may be part of a resonant RF circuit used to amplify the RF electric field, thereby increasing optical modulation. Since the WGM nature of the optical field strongly confines light to the edge of the disk, the electrodes can be patterned to significantly overlap the optical and electromagnetic fields inside the disk. Optimizing the overlap improves RF field sensitivity. One way to achieve this for static electric measurements is to use a metal electrode ring geometry placed on the top flat surface of a thin disk as is schematically shown in Figure 14(a). The inner and outer radius of the metal annulus, the metal thickness, and the disk thickness should be designed to optimize capacitance and inductance and minimize resistance. The use of thin disks increase the electric field and hence the electro-optic effect in the region of optical resonance. Figure 15 is a photograph of a thin z -cut LiNbO_3 disk-shaped resonator with optically polished curved side-walls and gold electrodes placed in an annulus around the disk to increase the overlap of RF and optical fields. Figure 14(b) shows another patterning scheme where electrode structures are placed on the outer curved surface of the LiNbO_3 disk to allow electrode spacing d smaller than $25 \mu\text{m}$. The advantage of this approach is that electrode spacing may be varied essentially independently of

disk thickness. This three-dimensional patterning is quite challenging, and techniques to accomplish this must still be developed.

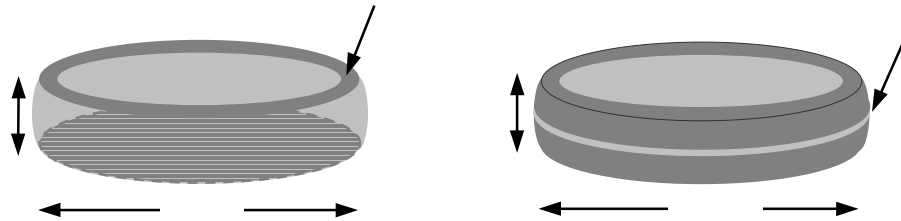


Figure 14. Schematic diagram of low-capacitance metal-electrode structure for RF coupling to a z-cut LiNbO_3 optical disk resonator. (a) Metal electrodes placed on the flat top and bottom surfaces of the disk are patterned into an annulus whose outer circumference is the same as the disk. (b) Metal electrodes coat the outer curved surface of the disk.



Figure 15. Photograph of a with radius $R = 3 \text{ mm}$ and thickness $d = 0.74 \text{ mm}$ z-cut LiNbO_3 disk-shaped resonator with optically polished curved side-walls. Gold electrodes are placed in an annulus around the disk to increase the overlap of RF and optical fields.

Optical modulation in the microphotonic modulator is most efficient when the RF and optical electric fields are simultaneously in resonance. As will be discussed in Chapter 4, two schemes were used to achieve resonant RF electrical coupling to the

microphotonic modulator. Initially, a direct-contact patterned metal electrode with no RF electric field gain was used to allow investigation of optical modulation independent of the effects of RF electric gain. Finally, a side-coupled patterned metal electrode with RF voltage gain was implemented.

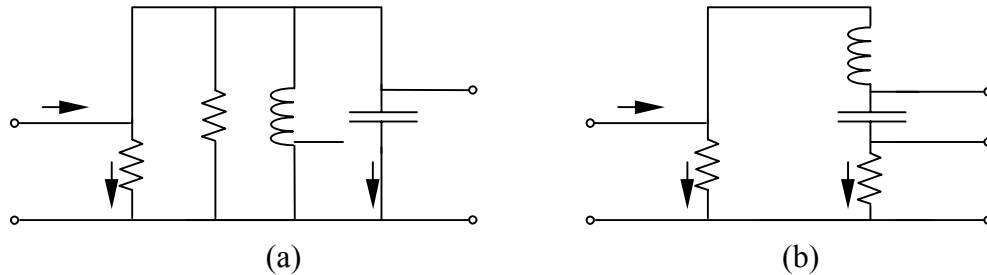


Figure 16. (a) Resonant parallel or shunt LCR circuit which provides current gain across the capacitor. (b) Series LCR circuit used to understand maximum power transfer to the RF circuit with voltage gain across the capacitor.

Maximization of power transfer to the RF circuit can be understood through the use of a resonant LCR network as shown in Figure 16. In this case, the small dielectric resonator responds as a capacitor C to applied electric fields. At the resonant frequency of the circuit, an inductor L in series with the resonator provides the needed impedance to minimize the total series impedance ($i\omega L + 1/i\omega C$). In the case of the parallel LCR circuit, the voltage across the capacitor V_C is in parallel with the driving voltage V_1 , and therefore the resonant circuit provides current gain, but no voltage gain. The advantage of the resonant series LCR network is that the impedance minimum provides a maximum current resulting in an enhancement of

the voltage across the capacitor. Therefore, in a series LCR circuit there is an amplification of the electric field across the disk. The total voltage V_1 , and voltage modulus $|V_1|$ across the LCR part of the circuit is

$$V_1 = I_2 \left(R + i\omega L + \frac{1}{i\omega C} \right) \quad |V_1| = |I_2| \sqrt{R^2 + \left(\omega L - \frac{1}{\omega C} \right)^2}$$

The voltage V_C , and voltage modulus $|V_C|$ across the capacitor is

$$V_C = I_2 \left(\frac{1}{i\omega C} \right) \quad |V_C| = \frac{|I_2|}{\omega C}$$

Combining these two equations gives

$$|V_C| = |V_1| \left(\omega C \sqrt{R^2 + \left(\omega L - \frac{1}{\omega C} \right)^2} \right)^{-1}$$

At the resonant frequency ω_r , the capacitor voltage $|V_C|$ is maximized at an amplified value of

$$|V_C| = \frac{1}{\omega_r RC} |V_1| \quad \omega_r^2 = \frac{1}{LC}$$

The quality factor Q is defined for this circuit to be $Q = \omega_r / \Delta\omega$, where $\Delta\omega$ is the full width half maximum of the RF power resonance peak. It is easiest to find $\Delta\omega$ from the voltage resonance peak of the resistor R . The voltage across the resistor V_R is

$$|V_R| = |V_1| \frac{R^2}{\sqrt{R^2 + \left(\omega L - \frac{1}{\omega C} \right)^2}}$$

Solving for ω when V_R is $1/\sqrt{2}$ gives the result

$$\Delta\omega = \frac{R}{L} + \frac{R^2 C^{1/2}}{L^{3/2}}$$

For large values of Q , the second term is small, and is ignored. Therefore, we find that $\Delta\omega = R/L$ and

$$Q = \omega_r L/R = 1/(\omega_r RC) = \sqrt{\frac{1}{R^2} \frac{L}{C}}$$

$$|V_2| = Q |V_1|$$

at the resonance frequency $\omega_r = (LC)^{-1/2}$. This shows that the voltage gain is equal to the quality factor Q of the circuit. Therefore for a $Q = 100$, with $1V$ driven across the circuit, the instantaneous voltage across the disk resonator is $100 V$.

The trend of Q with increasing frequency depends on the change in the ratio of L/C . If the value of L/C grows with increasing frequency, the Q of the circuit will also increase. This results from an increased value of the total circuit reactance as compared to the resistance R .

Within a fixed geometry, resistance and impedance change with increasing frequency. Resistive losses resulting from decreasing skin depth increase as $R \sim \omega^{1/2}$. Inductance L is composed of an external inductance L_{ext} that remains largely constant with frequency, and an internal inductance correction term L_{int} . This latter

term is a result of magnetic field lines inducing currents within the skin depth of the metal conductor. At large frequency, this correction term becomes important with the resulting impedance ωL_{int} equal in magnitude to the resistance R . Therefore $L_{ext} \sim \omega^{1/2}$ [66]. Because this is a correction term, it does not have the large effect on the circuit as the frequency dependence of R . Mention of the frequency dependence of capacitance was not readily found in the literature. In the specific case of high quality ceramic capacitors, changing phase response at high frequencies lead to inductive behavior. In addition, as frequencies increase, currents inside metal conductors transition to a sheet of current along the skin depth of the metal. It is therefore assumed that the change in fringing electric field lines from this redistribution of current only introduces small correction terms to the total value of C . Overall, the resistance R contributes the largest frequency dependence.

In addition, the RF electric field on the metal electrodes of the disk interacts with photons via the electro-optic effect and not a resistive electrical load. Consequently no damping of the RF Q due to a load resistor occurs for the LiNbO₃ disk. This is an inherent property of the optical isolation provided by use of a LiNbO₃ resonator in the system. Lumped element RF resonant circuit designs should be able to provide a $Q > 100$ at frequencies approaching 60 GHz. Resistive losses resulting from decreasing skin depth increase as $R \sim \omega^{1/2}$, whereas $Q = \sqrt{\frac{1}{R^2} \frac{L}{C}}$ [67]. Therefore,

although the resistance goes up with increasing frequency, in the absence of other material losses one expects that L/C must increase by design change for Q to remain fixed.

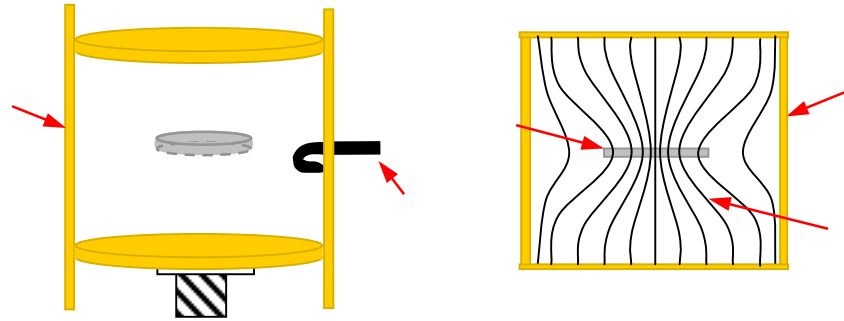


Figure 17 Schematic cross-section diagram of metal-walled RF cavity structure showing z -cut LiNbO_3 optical disk resonator coupling to electric field lines.

2.5.2 Metal-walled RF cavity

Metal-walled RF cavity structures for electromagnetic coupling to the microphotonic resonator have also been designed and investigated. A tunable metal-walled RF cavity similar to that shown schematically in Figure 17 has been designed and implemented to explore electrode-less RF coupling to LiNbO_3 microphotonic resonators. The resulting loaded cavity Q is shown in Figure 18. The resonant frequency of the metal-walled cavity may be tuned by mechanically by varying the height. The key design challenge was the coupling of light into the disk while maintaining efficient RF coupling. This challenge was overcome by first drilling small holes in the cavity. These holes were small enough to let light in and out of the cavity, while preserving the RF Q . As will be discussed in Chapter 4, optical

modulation cannot be achieved in this type of symmetric cavity. However, at frequencies beyond 60 GHz (where V-connectors begin to become lossy), RF propagation challenges may require that a non-symmetric version of this method of RF coupling be revisited.

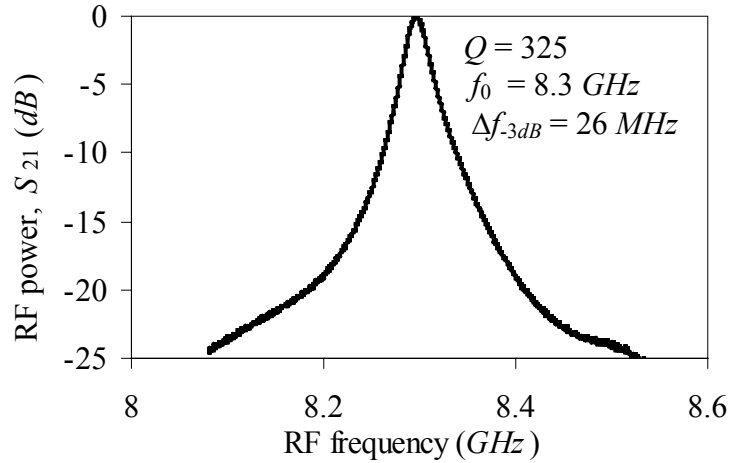


Figure 18 Loaded Q of a tunable metal-walled RF cavity. The center frequency is tunable from 7 GHz to 11 GHz, and the electrical $Q = 325$.

2.6 Summary

Although the LiNbO₃ optical disk resonator is challenging to fabricate, high quality results can be achieved. Optical polishing of LiNbO₃ has led to optical Q 's greater than 10^6 . Decreasing the radius of the disk to 2 mm, and the thickness to 200 μm has been achieved. As a complication of the high index of LiNbO₃, optical coupling methods are limited and challenging. In our initial experiments, prism coupling has provided up to 25 % coupling of light. Initial patterning of electrodes and RF cavity

development have been successful, and have been used to obtain the results in following chapters.

2.7 References

- [54] Valpey Fisher website, available at <http://www.valpeyfisher-ud.com/>
- [55] Hutcheson, L. D.: 'Integrated Optical circuits and components', (Merrel Dekker, Inc., New York, 1987), ISBN 8-8247-7575-9
- [56] Yariv, A., Yeh, P.: 'Optical waves in crystals', (John Wiley and Sons, New York, 1984), ISBN 0-471-09142-1
- [57] Robertson, W. M., Arjavalingam, G., and Kopcsay, G. V.: 'Broadband microwave dielectric properties of LiNbO₃', *Electron. Lett.*, 1991, **27**, pp. 175-176
- [58] Wong, K. K.: 'Properties of lithium niobate', (INSPEC, Institution of Electrical Engineers, London, 1989), ISBN 0 85296 7993
- [59] Weis, R. S. and Gaylord, T. K.: 'Lithium Niobate: Summary of Physical Properties and Crystal Structure', *Appl. Phys. A*, 1985, **37**, pp. 191-203
- [60] LiNbO₃ Group Home Page, University of Padova, Italy, available at <http://solidi4.padova.infm.it/research.html>
- [61] Klien, M. V., and Furtak, T. E.: 'Optics', (John Wiley and Sons, New York, 1986), ISBN 0-471-87297-0
- [62] Hill, S. C., and Benner, R. E.: 'Optical Effects Associated With Small Particles', (World Scientific, Singapore, 1988)
- [63] Braginsky, V. B.; Gorodetsky, M. L.; and Ilchenko, V. S.: 'Quality-factor and nonlinear properties of optical whispering-gallery modes', *Phys. Lett. A*, 1989, **137**, pp. 393-397
- [64] Ulrich, R.: 'Optimum excitation of optical surface waves', *J. Opt. Soc. Am.*, 1971, **61**, pp. 1467-1477

- [65] Chelnokov, A.V., and Lourtioz, J. M.: 'Optimized coupling into planar waveguides with cylindrical prisms' *Electron. Lett.*, 1995, **31**, pp. 269-271
- [66] Hoffman, R. K.: 'Handbook of microwave integrated circuits', (Artech House, Norwood, MA, 1987) ISBN 0-89006-163-7
- [67] Rizzi, P. A.: 'Microwave Engineering Passive Circuits', (Prentice Hall, Englewood Cliffs, NJ, 1988), ISBN 0-13-586702-9

Chapter 3

Passive LiNbO₃ microphotonic modulator

3.1 Introduction

Much of the fundamental physics of the LiNbO₃ microphotonic resonator can be understood through investigation of the passive (absence of applied RF electric field) response of the cavity. Optical excitation of whispering gallery modes provide information such as the passive optical cavity spectrum, cavity response times, and cavity Q . Coupling into RF modes using microstrip-line excitation can provide information on the RF properties of the resonator.

3.2 Whispering gallery mode excitation

Whispering gallery modes (WGM) in spherical and disk-shaped dielectric resonators arise from the solution to Maxwell's equations describing the behavior of electromagnetic fields. The large dielectric discontinuity between air and resonator result in modes that for the sake of simplicity can be ascribed to total internal reflection. These whispering gallery resonances are characterized by very high

electric-field intensity close to the air-dielectric interface and very high- Q . Loss due to finite curvature becomes small when the resonator dimension is significantly greater than the optical resonance wavelength. Hence, for optical wavelengths near $\lambda = 1.55 \mu m$, the Q of optical dielectric resonators greater than $\sim 10 \mu m$ in diameter is typically limited by attenuation due to scattering from surface imperfections.

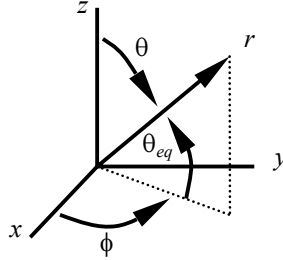


Figure 19 The coordinate system used to solve the electromagnetic modes of a spherical resonator.

The electromagnetic solutions to the disk resonator are found by defining the disk to be a sphere with part of the top and bottom hemispheres removed. The geometry for this resonator is shown in Figure 19, with a photograph of a LiNbO_3 disk in Figure 20. The problem of electromagnetic oscillation in a dielectric sphere has been solved explicitly for a lossless, linear medium with no sources [68].

Assuming monochromatic solutions of the form $\mathbf{E}(\mathbf{r}, t) = \mathbf{E}(\mathbf{r})e^{-i\omega t}$ the vector Helmholtz equation is

$$\nabla^2 \mathbf{E}(\mathbf{r}) + \mu\epsilon \frac{\omega^2}{c^2} \mathbf{E}(\mathbf{r}) = 0$$

where ε and μ are the relative permittivity and permeability, and $\omega = 2\pi f$, where f is the frequency of the electric field. We would like to express the vector \mathbf{E} in terms of radial (E_r), meridional (E_θ), and azimuthal (E_ϕ) components. However, the Laplacian of the vector \mathbf{E} results in three partial differential equations each involving E_r , E_θ , and E_ϕ . Therefore the simple separation of the Helmholtz equation in the rectangular coordinate system, does not occur in the spherical coordinate system.

It can be shown that the three solutions

$$\mathbf{E} = (\nabla\psi), \quad \mathbf{E}_{TE} = (\mathbf{r} \times \nabla\psi), \quad \text{and} \quad \mathbf{E}_{TM} = \frac{ic}{\omega} \nabla \times (\mathbf{r} \times \nabla\psi)$$

are also independent vector solutions which result in three separable partial differential equations. Using these solutions, the scalar Helmholtz equation is solved for ψ , where the scalar equation is given by

$$\nabla^2\psi + \mu\varepsilon \frac{\omega^2}{c^2}\psi = 0$$

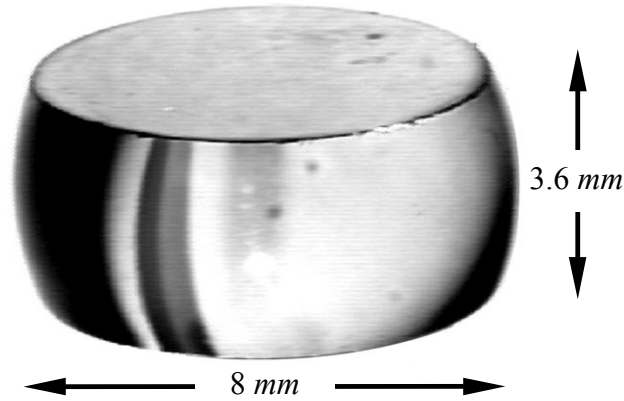


Figure 20 Photograph of z -cut LiNbO_3 disk-shaped resonator with gold electrodes and optically polished curved side-walls.

The solutions \mathbf{E}_{TE} and \mathbf{E}_{TM} are those of interest for electromagnetic solutions called whispering gallery modes (WGM) excited by evanescent coupling along the equator of the sphere. The first is named the transverse electric (TE) solution because \mathbf{E}_{TE} is tangent to the spherical surface, while the second is the transverse magnetic (TM) solution because the magnetic field \mathbf{H}_{TM} is tangent to the spherical surface [69]. This notation is opposite to that used with microdisks [70] where TE polarization is along the radial unit vector. The microdisk definition comes from optical confinement similarities to optical waveguides.

Although this problem can be solved explicitly, a simplification is achieved by assuming that the electromagnetic field polarization can be approximated as constant along one coordinate axis [71]. Then the TE and TM modes are redefined as those with vector electric field components

$$\mathbf{E}_{TM} = \hat{\theta}E_{\theta} \equiv \hat{\theta}\Psi$$

$E_r = E_{\phi} = 0$, and TM modes defined as those with vector magnetic field components

$$\mathbf{H}_{TM} = \hat{\theta}H_{\theta} \equiv \hat{\theta}\Psi$$

$H_r = H_{\phi} = 0$. This was verified numerically by Little, et al. using the case of a sphere surrounded by air with a 25 μm radius and refractive index of 1.45 [71]. The simulated TE (TM) modes show 99.8% of the mode energy along the E_{θ} (H_{θ}) polarization, while 0.2% lies along the orthogonal component. It was also found that

this fraction of energy increases as the disk becomes larger, and therefore this approximation is even better for our case of a 2 mm or larger disk.

This approximation permits the separation of the vector Helmholtz equation as seen with rectangular coordinates. Again starting with the vector Helmholtz equation, and using the definitions for E_{TE} (H_{TM}) above, the resulting scalar equation

$$\nabla^2 \psi + \mu \epsilon \frac{\omega^2}{c^2} \psi = 0$$

can easily be solved in the spherical coordinate system. Defining $k^2 = \mu \epsilon \omega^2 / c^2$, the scalar equation becomes

$$\nabla^2 \psi + k^2 \psi = 0$$

where

$$\nabla^2 = \frac{1}{r^2} \frac{\partial}{\partial r} \left(r^2 \frac{\partial}{\partial r} \right) + \frac{1}{r^2 \sin \theta} \frac{\partial}{\partial \theta} \left(\sin \theta \frac{\partial}{\partial \theta} \right) + \frac{1}{r^2 \sin^2 \theta} \frac{\partial^2}{\partial \phi^2}$$

The solution to this is separable, and of the form $\psi(r, \theta, \phi) = \psi_r(r) \psi_\theta(\theta) \psi_\phi(\phi)$. By substituting this into the scalar wave equation, we find a simultaneous system of three scalar equations

$$\frac{d^2}{d\phi^2} \psi_\phi - m^2 \psi_\phi = 0$$

$$\frac{1}{\sin \theta} \frac{d}{d\theta} \left(\sin \theta \frac{d}{d\theta} \psi_\theta \right) - \frac{m^2}{\sin^2 \theta} \psi_\theta + l(l+1) \psi_\theta = 0$$

$$\frac{d^2}{dr^2} \psi_r + \frac{2}{r} \frac{d}{dr} \psi_r + k^2 - \frac{l(l+1)}{r^2} \psi_r = 0$$

The solutions to the angular equations for θ and ϕ give [68]

$$\begin{aligned}\psi_\phi(\phi) &= e^{\pm jm\phi} \\ \psi_\theta(\theta) &= P_l^m(\cos\theta) \\ Y_{lm}(\theta, \phi) &= P_l^m(\cos\theta)e^{\pm jm\phi}\end{aligned}$$

where m is an integer, $l \geq 0$, and $|m| \leq l$, $\psi_\theta(\theta)$ are the associated Legendre polynomials, and Y_{lm} are the spherical harmonics.

The radial solutions $\psi_r(r)$ are found to be spherical Bessel functions from the radial equation above by letting $x \equiv kr$, and $\psi_r(r) \equiv x^{1/2}u_l(x)$. Then the equation becomes

$$\frac{d^2}{dx^2}u_l(x) + \frac{1}{x}\frac{d}{dx}u_l(x) + 1 - \frac{(l + \frac{1}{2})^2}{x^2}u_l(x) = 0$$

which is just Bessel's equation. Boundary conditions are then applied to obtain the characteristic equations and normalization constants. By applying the boundary condition at the disk radius R_0 , and restricting the spherical Bessel function from diverging at the origin,

$$E_{TE}(H_{TM}) = \sum \psi(r, \theta, \phi) = \sum_{lm} \psi_r^l(r) Y_{lm}(\theta, \phi)$$

$$\begin{aligned}\psi_r^l(r) &\propto j_l(kr) & r \leq R_0 \\ \psi_r^l(r) &\propto e^{-\alpha_s(r-R_0)} & r > R_0\end{aligned}$$

The radial solution outside the disk was found by defining $r = R_0(1+x^2/R_0)$ and expanding the solution about $x^2 \ll 1$. This exponential decay defines only the bound

portion of the field outside the sphere. Radiation modes are ignored. In the equations above $k = 2\pi n_s / \lambda$, where n_s is the refractive index of the sphere. The third eigenvalue η is found from the characteristic equations resulting from the boundary condition that the interior and exterior tangential fields at the surface of sphere must be equal.

From these solutions, we find the eigenmodes of the microresonator are characterized by polarization (TE or TM), and the three eigenvalues η , l , and m . The radial eigenvalue $\eta \geq 1$ is the number of field maxima in the direction of the sphere radius, l is approximately the number of wavelengths that fit into the optical length of the resonator, and m is the number of field maxima in the equatorial plane. We will show later that the number of polar intensity maxima is $l-m+1$.

Figure 21(a) shows a projection of the spherical harmonics on a unit sphere for low values of $l = m$. We see that as $l = m$ increases, the optical power begins to concentrate closer to the equator. The longitudinal cross section of the x - z plane in Figure 21(b) displays the concentration of field toward both the equator and disk edge as l and m increase. Figure 21(c) shows a cross section of the mode in the x - y plane. This demonstrates the increase of the number of field maxima, and the trend of the mode to become more tightly confined to the disk edge.

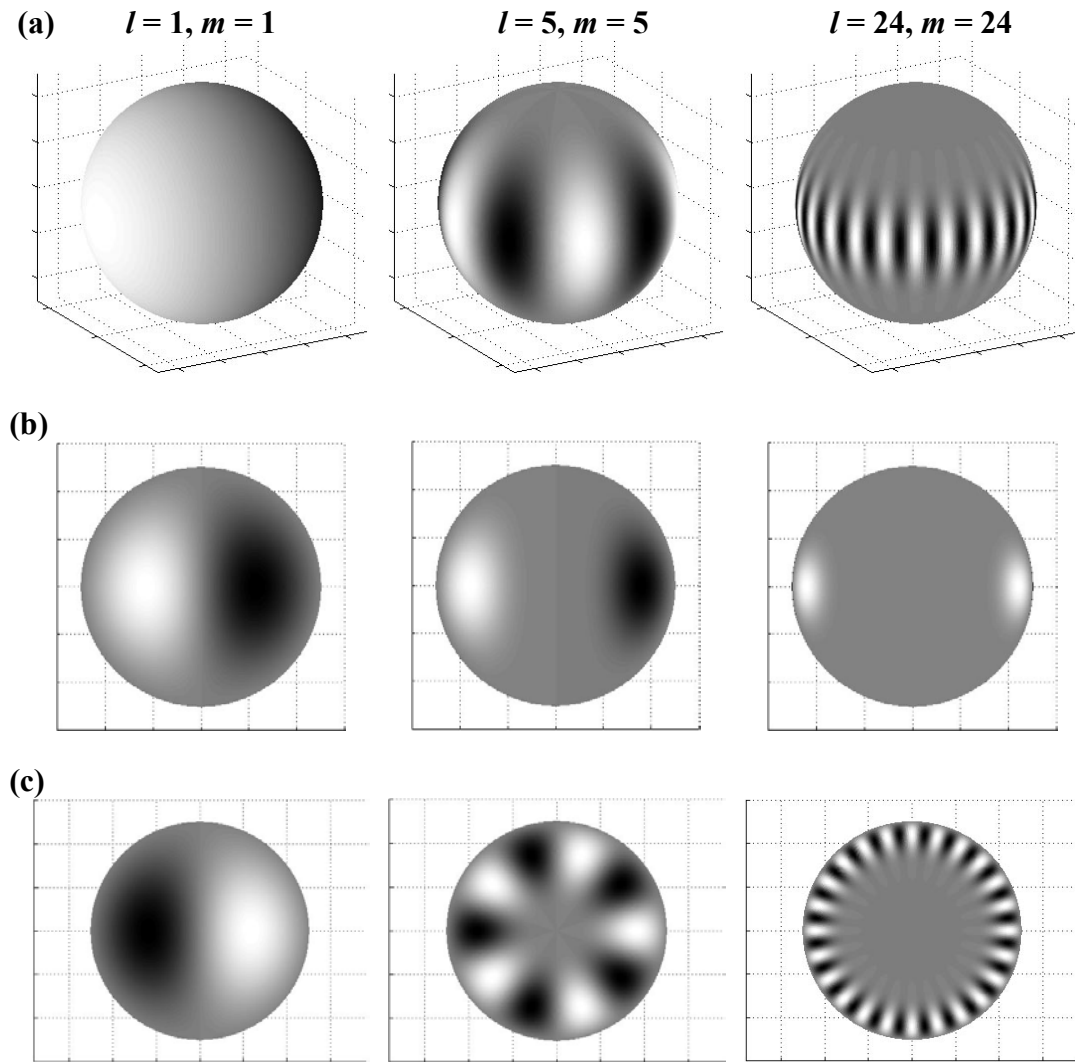


Figure 21. Normalized modal distributions for $l = m = 1, 5,$ and 24 . (a) Projection of spherical harmonics on a unit sphere for $(l, m) = (1, 1), (5, 5),$ and $(24, 24)$. The energy distribution becomes more concentrated near the equator as l and m increase. (b) Longitudinal cross section (x - z plane) showing WGM for $\eta = 1$, and $(l, m) = (1, 1), (5, 5),$ and $(24, 24)$. The trend shows the concentration of field toward both the equator and disk edge as l and m increase. Note for $l = m = 5$, the mode number m is odd, and therefore two maxima in the cross section. (c) Equatorial cross section of WGM for $\eta = 1$, and $(l, m) = (1, 1), (5, 5),$ and $(24, 24)$. The trend shows the increase in lobe number, and the concentration of field toward the disk edge as l and m increase.

A significant approximation can be made with the polar dependence [72]. The result demonstrates that the most strongly coupled modes are those of mode numbers $l = m$.

The radius of a typical microresonator leads to values of m and l that are very large (6 mm disk has $l \approx 25,000$). This will also result in the mode being very tightly confined to the equator.

To understand the angular distribution of the mode along the polar axis, we define a new coordinate $\theta_{eq} = \theta - \pi/2$, such that $\theta_{eq} = 0$ along the equator as shown in Figure 19. Making the approximations $\theta_{eq} \ll 2\pi$, and $m \gg 1$, and including this in the polar differential equation, $\psi_\theta(\theta_{eq})$ becomes

$$\psi_\theta(\theta_{eq}) \propto e^{-m/2\theta_{eq}^2} H_N(\sqrt{m}\theta_{eq})$$

$$N = l - m$$

where $H_N(x)$ are the Hermite polynomials, with $H_0(x) = 1$, $H_1(x) = 2x$, $H_2(x) = 4x^2 - 2$, etc. This shows in the case of large m , and $l \approx m$ the resulting WGM is Gaussian in nature. From this approximation, and the nature of Hermite polynomials, we see that there are $l-m+1$ polar intensity maxima. Figure 22 shows a projection of spherical harmonics on a unit sphere for $l - m = 0, 1$, and 2 . At $l-m=0$, the mode is Gaussian and centered about the equator. As $l-m$ increases, the energy distribution spreads further from the equator. Because input laser light typically has a Gaussian beam profile, we expect that the $l=m$ Gaussian modes are those that are most strongly coupled [72].

Fundamental whispering gallery modes are usually defined as those where the light is confined closest to the disk edge. These modes occur when $\eta = 1$ and $l = m$. Other modes are considered higher order modes. In a perfect sphere, whispering gallery mode frequencies depend only on η and l , and are $2m+1$ degenerate in frequency. However, in any real sphere, there is some ellipticity that breaks the degeneracy of the eigenvalue m [73].

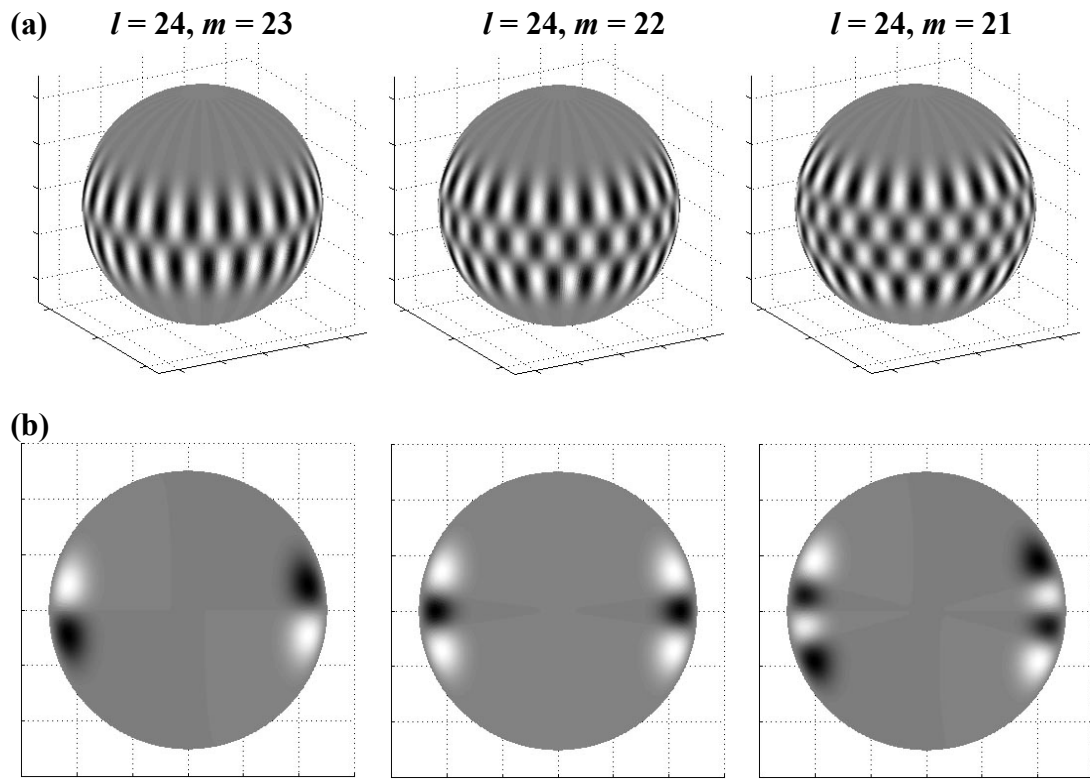
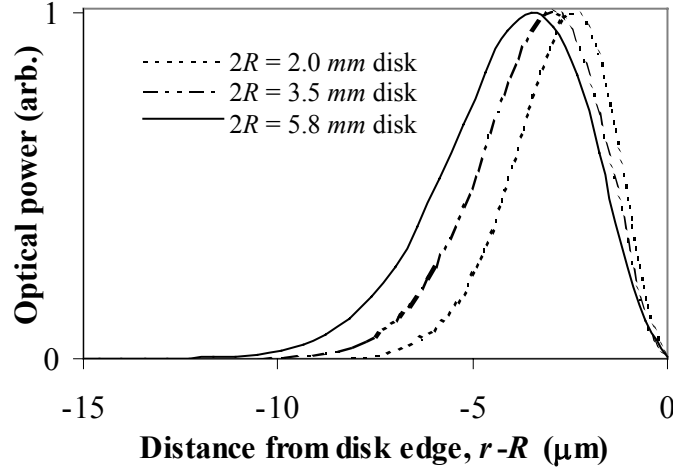


Figure 22. Normalized modal distributions for $l = 24$, and $m = 23, 22$, and 21 . (a) Projection of spherical harmonics on a unit sphere for $(l,m) = (24,23)$, $(24,22)$, and $(24,21)$. At $l-m=0$, the mode is Gaussian and centered about the equator. As $l-m$ increases, the energy distribution spreads further from the equator. (b) Longitudinal cross section ($x-z$ plane) showing WGM for $\eta = 1$, and $(l,m) = (24,23)$, $(24,22)$, and $(24,21)$. The trend shows the concentration of field expands away from the equator as m is increased.

(a)



2.0 mm diameter disk

3.5 mm diameter disk

5.84 mm diameter disk

(b)

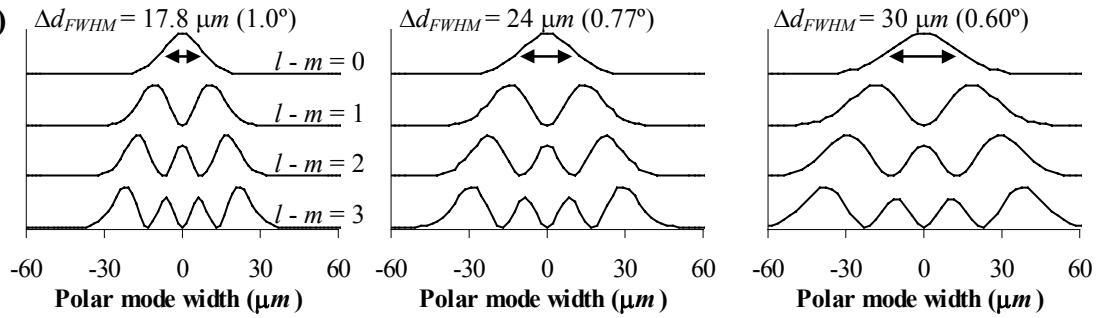


Figure 23. WGM power distribution for disks of large $l = m$. (a) Normalized profile of spherical Bessel functions with $\eta = 1$ for a 2.0 mm ($l = 8690$), 3.5 mm ($l = 15,120$), and 5.84 mm ($l = 25,260$) disk. The full width half maximum (FWHM) of the modes are 2.6 μm , 3.7 μm , and 4.8 μm for the 2.0 mm, 3.5 mm, and 5.84 mm disks respectively, (b) Normalized profile of spherical harmonics using Hermite polynomial approximation for $N = l - m = 0, 1, 2$, and 3, for a 2.0, 3.5, and 5.84 mm disk.

Figure 23 shows the simulated WGM power distribution for disks typical of that used in experimentation. These disks are of large $l = m$, with l typically in the thousands. Figure 23(a) shows the normalized radial profile of the spherical Bessel function with $\eta = 1$ for a 2.0 mm ($l = 8690$), 3.5 mm ($l = 15,120$), and 5.84 mm ($l =$

25,260) disk. The full width half maximum (FWHM) of the modes are $2.6 \mu\text{m}$, $3.7 \mu\text{m}$, and $4.8 \mu\text{m}$ for the 2.0 mm , 3.5 mm , and 5.84 mm disks respectively. Normalized profile along the z -axis for $N = l - m = 0, 1, 2,$ and 3 , for a $2.0, 3.5,$ and 5.84 mm disk. This shows that although the angular distribution of the mode increases with decreasing disk radius, the mode height along the z -axis decreases.

3.3 Experimental setup

A schematic of the experimental setup is shown in Figure 24. Laser light with $\lambda = 1.55 \mu\text{m}$ is incident on the side face of the input prism. Light is then evanescently coupled into WGM modes of the disk. Output light is monitored using two different configurations. Figure 24(a) shows one prism coupling, where light is monitored at the output of the first prism. In the second case, a second prism is added, and light is monitored at the output as shown in Figure 24(b). Figure 25 shows a photograph of the two prism coupling method using diamond prisms, and a lensed single mode fiber output.

Figure 26(a) is a photograph of a prism coupler placed next to a LiNbO_3 disk viewed from above. The side-view in Figure 26(b) shows scattered laser light on only the right side of the disk periphery (the bright spots on the left side are prism reflections) which is consistent with a traveling wave excitation of the disk.

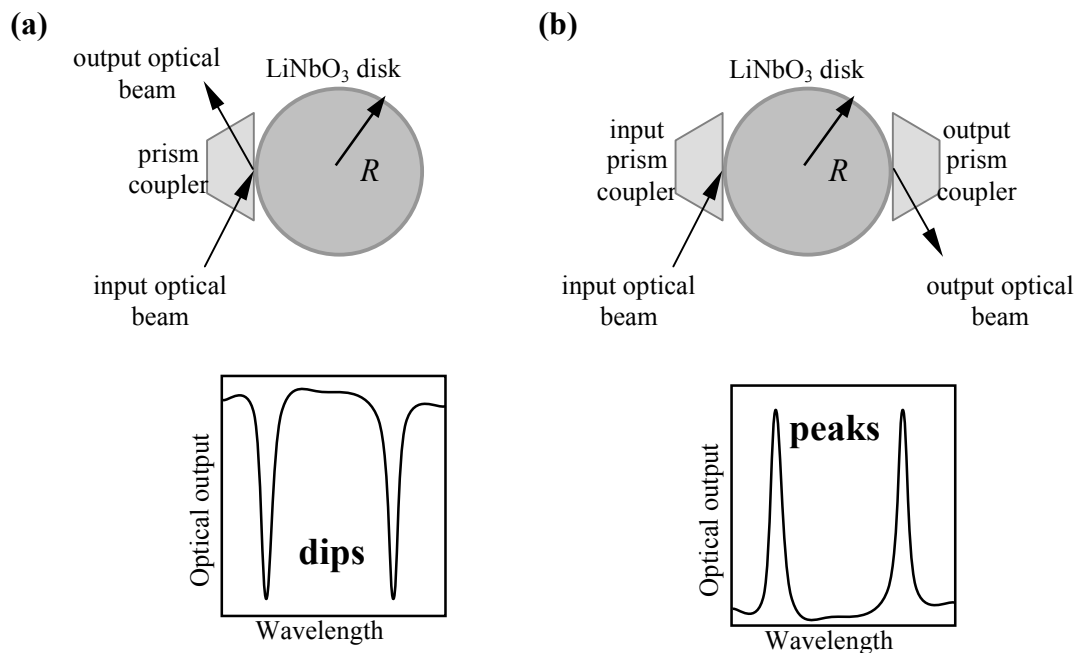


Figure 24 (a) Single prism coupling. Light is coupled into the disk using a single prism. The output is a series of resonant dips. (b) Two prism coupling. Light is coupled into the disk in one prism, and output at another prism. The output is a series of resonant peaks.

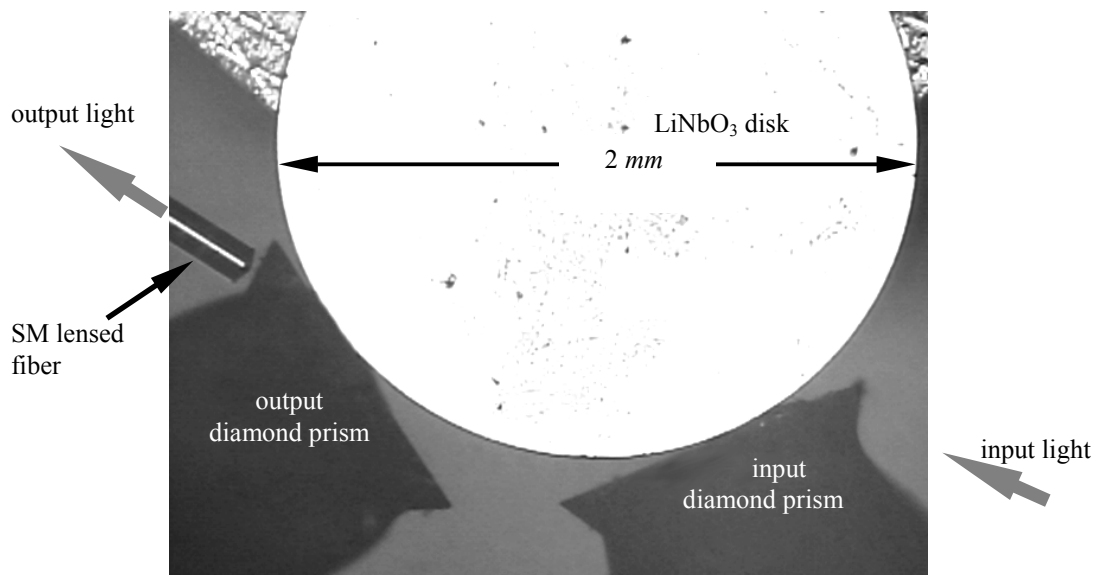


Figure 25 Top view of two prism coupling using diamond prisms. Input light is coupled into the prism on the right. Light output from the disk is collected at the single mode fiber output coupler.

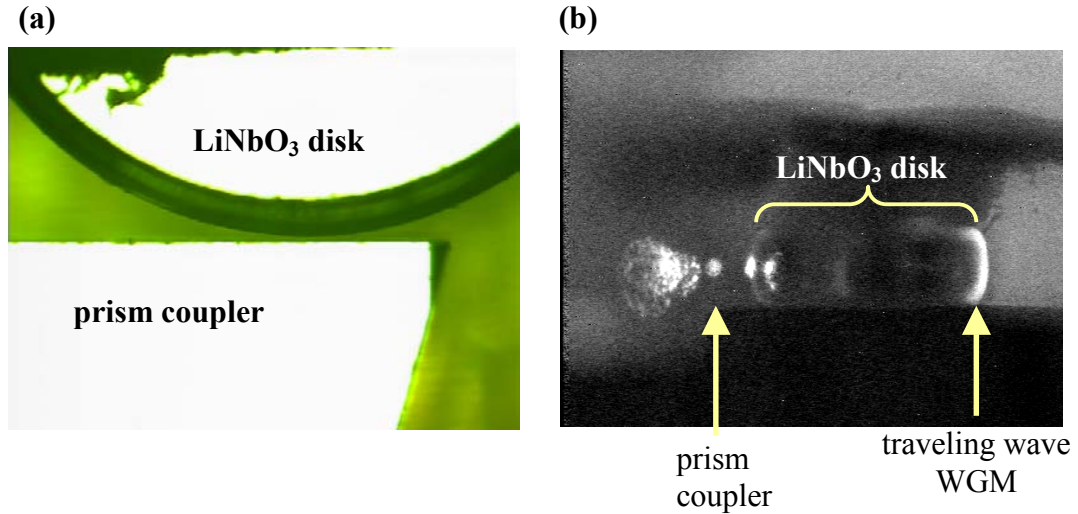


Figure 26. (a) Photograph of LiNbO₃ disk and prism-coupler viewed from above. (b) Infrared side-view of disk resonator and prism showing optical coupling at $\lambda = 1550 \text{ nm}$ wavelength. Coupled laser light on the disk periphery is indicated by the arrow.

Two different coupling prism materials have been utilized. The first was an xy-cut LiNbO₃ prism. Light polarized along the extraordinary z -axis of the disk sees the ordinary axis of the prism. This therefore satisfies the coupling condition in Chapter 2, $n_{prism} (2.21) > n_{opt} (2.14)$.

Improved optical coupling was achieved with diamond prisms ($n_{diamond} = 2.4$). These $1 \text{ mm} \times 0.4 \text{ mm} \times 0.4 \text{ mm}$ prisms provided a total 25% optical coupling efficiency in the two-prism coupling scheme shown in Figure 25. Enhanced coupling with diamond vs. xy-cut LiNbO₃ is a result of the larger refractive index difference eliminating excitation of higher order radial modes deeper in the disk (see penetration depth, δ in Chapter 2).

3.4 Principles of the coupler-resonator system

Basic principles regarding the coupling of photons into and out of the microphotonic resonator can be understood through a directional coupler approach. Figure 27 shows the generic approach to model the coupling of light from any evanescent coupler (e.g. prism) into a disk or ring structure. Input light is incident on coupling region 1 with an electric field coupling coefficient $i\kappa_1$, and output from coupling regions 1 and 2 with electric field coupling coefficients $-i\kappa_1^*$ and $-i\kappa_2^*$ respectively. In analogy with Figure 24, one prism coupling is defined when monitoring output 1 with $\kappa_2 = 0$, and two prism coupling when monitoring output 2 with $\kappa_2 \neq 0$.

Using the steady-state loop approach [73], A_1 is defined as the steady state electric field amplitude for input light entering coupling region 1, B_1 is the field exiting coupling region 1, and A_2 and B_2 are the fields inside the resonator before and after coupling region 1. Similarly, D_1 is the field exiting coupling region 2, and C_2 and D_2 are the fields inside the resonator before and after coupling region 2. For simplicity, a lossless symmetric coupler is assumed, with field coupling constant $i\kappa_1 = -i\kappa_1^*$ in region 1, and $i\kappa_2$ in region 2. The transmission coefficient $T_{A_1B_1}$ from A_1 to B_1 is $T_{A_1B_1} = (1-\kappa^2)^{1/2}$. In the case of the prism coupler, the coupling coefficient κ is a function of gap spacing, coupler geometry, and disk size.

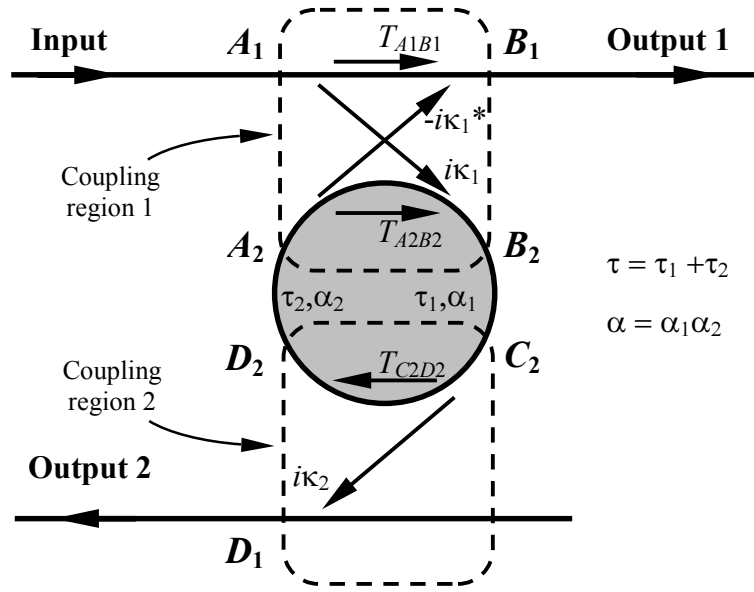


Figure 27 Directional coupler model used to understand coupling principles. Photons incident on the input directional coupler are evanescently transferred into a ring or disk. After traveling around the disk, light is evanescently coupled out of the resonator at either output 1 or output 2.

The roundtrip disk electric optical field transmission coefficient $\alpha = \alpha_1\alpha_2$, where $\alpha_1 = \exp(-\alpha_{01}L_1/2)$ is the electric field transmission coefficient for the length L_1 between coupling region 1 and 2, and $\alpha_2 = \exp(-\alpha_{02}L_2/2)$ is the electric field transmission coefficient for the length L_2 between coupling region 2 and before region 1. The constants α_{01} and α_{02} are the optical power loss per unit length for the regions L_1 and L_2 respectively. The refractive index of the resonator is n_d . Finally, the round trip time of the disk is $\tau = \tau_1 + \tau_2$, where $\tau_1 = n_dL_1/c$, and $\tau_2 = n_dL_2/c$. The self-consistent relations between field amplitudes at a time t for the two coupling regions are

$$\begin{aligned}
B_1(t) &= (1 - \kappa_1^2)^{1/2} A_1(t) + i\kappa_1 A_2(t) \\
B_2(t) &= i\kappa_1 A_1(t) + (1 - \kappa_1^2)^{1/2} A_2(t) \\
D_1(t) &= i\kappa_2 C_2(t) \\
D_2(t) &= (1 - \kappa_2^2)^{1/2} C_2(t)
\end{aligned}
\quad
\begin{pmatrix} B_1(t) \\ B_2(t) \end{pmatrix} = \begin{pmatrix} (1 - \kappa_1)^{1/2} & i\kappa_1 \\ i\kappa_1 & (1 - \kappa_1)^{1/2} \end{pmatrix} \begin{pmatrix} A_1(t) \\ A_2(t) \end{pmatrix}$$

$$\begin{pmatrix} D_1(t) \\ D_2(t) \end{pmatrix} = \begin{pmatrix} (1 - \kappa_2)^{1/2} & \kappa_2 \\ \kappa_2 & (1 - \kappa_2)^{1/2} \end{pmatrix} \begin{pmatrix} 0 \\ C_2(t) \end{pmatrix}$$

while optical propagation between coupling regions give

$$C_2(t) = \alpha_1 e^{-i\phi_1(t)} B_2(t - \tau_1)$$

$$A_2(t) = \alpha_2 e^{-i\phi_2(t)} D_2(t - \tau_2)$$

Where $\phi_1(t)$, and $\phi_2(t)$ are the electrically induced optical phase shift along lengths L_1 and L_2 . The imaginary coupling terms are understood from either coupled mode theory [75], or as a complex transmission coefficient due to the evanescent nature of the coupling [76].

We can solve this system of equations for either of the outputs $B_1(t)$ or $D_1(t)$ as a function of the input $A_1(t)$ and the field inside the disk $B_2(t)$, where

$$B_1(t) = (1 - \kappa_1^2)^{1/2} A_1(t) + i\kappa_1 (1 - \kappa_2^2)^{1/2} \alpha_1 \alpha_2 e^{-i((\phi_2(t) + \phi_1(t - \tau_2)))} B_2(t - \tau)$$

$$D_1(t) = -\kappa_1 \kappa_2 \alpha_1 e^{-i\phi_1(t)} A_1(t - \tau_1) + i\kappa_2 (1 - \kappa_1^2)^{1/2} (1 - \kappa_2^2)^{1/2} \alpha_1^2 \alpha_2 e^{-i(\phi_1(t) + \phi_2(t - \tau_1) + \phi_1(t - \tau))} B_2(t - \tau - \tau_1)$$

where in addition the recursion relation is evaluated to be

$$B_2(t) = i\kappa_1 A_1(t) + (1 - \kappa_1^2)^{1/2} (1 - \kappa_2^2)^{1/2} \alpha_1 \alpha_2 e^{-i(\phi_2(t) + \phi_1(t - \tau_2))} B_2(t - \tau)$$

Using the recursion relation, the total output field from coupling region 1,

$$E_{out1}(t) \equiv B_1(t) \text{ as a function of the field input to coupling region 1, } E_{in}(t) \equiv A_1(t)$$

$$E_{out1}(t) = \sqrt{1 - \kappa_1^2} E_{in}(t) - \frac{\kappa_1^2}{\sqrt{1 - \kappa_1^2}} \sum_{p=1}^{\infty} r^p e^{i \sum_{q=0}^{p-1} [\phi_1(t - \tau_2 - q\tau) + \phi_2(t - q\tau)]} E_{in}(t - p\tau)$$

where

$$r \equiv \alpha_1 \alpha_2 \sqrt{1 - \kappa_1^2} \sqrt{1 - \kappa_2^2}$$

If we assume a monochromatic input, $E_{in}(t) = E_0 e^{-i\omega t}$, where ω is the optical frequency, then $E_{in}(t - p\tau) = E_{in}(t) e^{-i\omega p\tau}$, and

$$E_{out1}(t) = \left[\sqrt{1 - \kappa_1^2} - \frac{\kappa_1^2}{\sqrt{1 - \kappa_1^2}} \sum_{p=1}^{\infty} \rho_1^p e^{i \sum_{q=0}^{p-1} [\phi_1(t - \tau_2 - q\tau) + \phi_2(t - q\tau)]} \right] E_{in}(t)$$

$$\rho_1 \equiv \alpha \sqrt{1 - \kappa_1^2} \sqrt{1 - \kappa_2^2} e^{i\omega\tau}$$

This equation is easily simplified to the single prism coupling case by setting $\kappa_2=0$.

Similar to the above method, the recursion relation is used to find the total electric field output from coupling region 2, $E_{out2}(t) \equiv D_1(t)$ as a function of $E_{in}(t)$. This gives

$$E_{out2}(t) = \left[-\kappa_1 \kappa_2 \alpha_1 e^{i(\omega\tau_1 + \phi_1(t))} \left(1 + \sum_{p=1}^{\infty} \rho_2^p e^{i \sum_{q=0}^{p-1} [\phi_1(t - (q+1)\tau) + \phi_2(t - \tau_1 - q\tau)]} \right) \right] E_{in}(t)$$

$$\rho_2 \equiv \alpha \sqrt{1 - \kappa_1^2} \sqrt{1 - \kappa_2^2} e^{i\omega\tau}$$

For single prism coupling using a solid metal ring when the RF frequency $\omega_{RF} = 2\pi f_{RF}$ is an integral multiple of the optical round trip period, $\omega_{RF}\tau = 2\pi m$, where m is an integer, it can be shown that

$$\sum_{q=0}^{p-1} [\phi_1(t - \tau_2 - q\tau) + \phi_2(t - q\tau)] = p[\phi_1(t - \tau_2) + \phi_2(t)] \equiv p\phi_{tot1}(t)$$

$$E_{out1}(t) = \left[\sqrt{1 - \kappa_1^2} - \frac{\kappa_1^2}{\sqrt{1 - \kappa_1^2}} \sum_{p=1}^{\infty} (\rho e^{i\phi_{tot1}(t)})^p \right] E_{in}(t)$$

where ϕ_{tot1} is the total phase shift on one round trip. This equation can be easily summed to give

$$E_{out1}(t) = \left[\sqrt{1 - \kappa_1^2} - \frac{\kappa_1^2}{\sqrt{1 - \kappa_1^2}} \left\{ \frac{\rho'_1}{1 - \rho'_1} \right\} \right] E_{in}(t)$$

$$\rho'_1 \equiv \alpha \sqrt{1 - \kappa_1^2} \sqrt{1 - \kappa_2^2} e^{i(\omega\tau + \phi_{tot1}(t))}$$

For the output of the second coupling region it can be shown that

$$\sum_{q=0}^{p-1} [\phi_1(t - (q+1)\tau) + \phi_2(t - \tau_1 - q\tau)] = p[\phi_1(t) + \phi_2(t - \tau_1)] \equiv p\phi_{tot2}(t)$$

$$E_{out2}(t) = \left[-\kappa_1 \kappa_2 \alpha_1 e^{i(\omega\tau_1 + \phi_1(t))} \left(\frac{1}{1 - \rho'_2} \right) \right] E_{in}(t)$$

$$\rho'_2 \equiv \alpha \sqrt{1 - \kappa_1^2} \sqrt{1 - \kappa_2^2} e^{i(\omega\tau + \phi_{tot2}(t))}$$

Regions for critical coupling of input optical power

An interesting condition occurs when the optical power coupled out of coupling region 1 goes to zero. This state is called *critical coupling* and maximizes the optical power coupled into the cavity.

An understanding of the coupling regions is easily given in the passive optical case.

The output from coupling region 1 is

$$E_{out1}(t) = \left[\sqrt{1 - \kappa_1^2} - \left\{ \frac{\alpha \kappa_1^2 \sqrt{1 - \kappa_2^2} e^{i\omega\tau}}{1 - \alpha \sqrt{1 - \kappa_1^2} \sqrt{1 - \kappa_2^2} e^{i\omega\tau}} \right\} \right] E_{in}(t)$$

$$= \frac{\sqrt{1 - \kappa_1^2} - \alpha \sqrt{1 - \kappa_2^2} e^{i\omega\tau}}{1 - \alpha \sqrt{1 - \kappa_1^2} \sqrt{1 - \kappa_2^2} e^{i\omega\tau}} E_{in}(t)$$

Therefore the two conditions that must be met for the output of coupling region 1 to equal zero are

$$\omega t = 2\pi n_s / \lambda (L_1 + L_2) = 2\pi m \quad (m \text{ any integer})$$

$$\alpha (1 - \kappa_2^2)^{1/2} = (1 - \kappa_1^2)^{1/2} = T_{A1B1}$$

The first is the optical field must be in resonance in the disk. The second condition results from conservation of energy. For example with single prism coupling $\kappa_2 = 0$, critical coupling implies that all input power couples into the disk, while no power couples out of the disk. Therefore, energy conservation requires that all power coupled into the disk during one round trip be lost, or $B_2^2 - A_2^2 = A_1^2$. Using the self-consistent relations above, we find that $\kappa_1 = (1 - \alpha^2)^{1/2}$, as is expected from condition 2.

There are three coupling regions in any coupling system, overcoupling, critical coupling, and undercoupling. Figure 28 shows the theoretical fraction of optical input power E_{in}^2 that is coupled into the disk using the single prism coupling scheme.

Overcoupling is shown to occur when $\kappa_1 > (1-\alpha^2)^{1/2}$. In this weakly coupled region only part of the input light is coupled into the disk. *Critical coupling* occurs when $\kappa_1 = (1-\alpha^2)^{1/2}$, and all of the input optical power is transferred into the disk, with no light coupling out of the disk. *Undercoupling* occurs in the strongly coupled region $\kappa_1 < (1-\alpha^2)^{1/2}$. Here all of the input power is coupled into the disk. However, strong coupling takes part of the input power and couples it back out of the disk. [77].

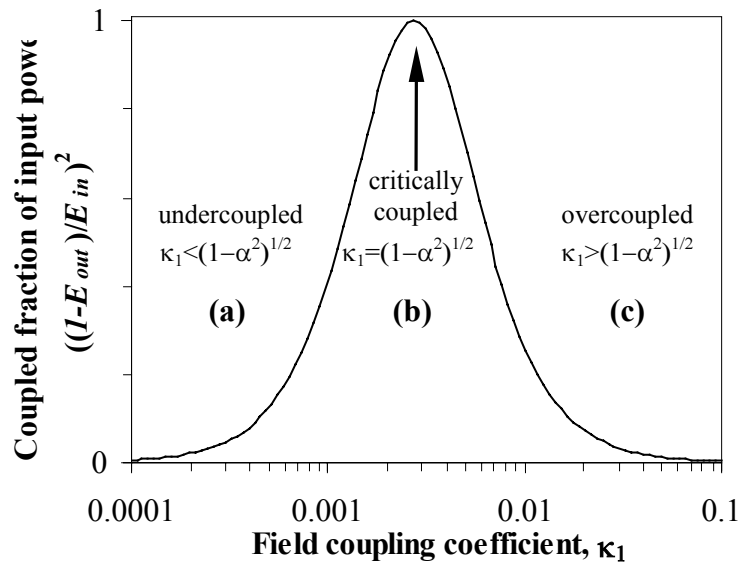


Figure 28. Fraction of light coupled into the disk as a function of the coupling coefficient κ_1 for a disk of radius 3 mm with $Q \sim 4 \times 10^6$ ($\alpha_{01} = 0.02 \text{ cm}^{-1}$) assuming single prism coupling ($\kappa_2 = 0$). (a) In the undercoupled region, not all of the input light couples into the disk. (b) With critically coupling all of the input light is coupled into the disk, and no light couples out. (c) Overcoupling occurs when all of the input light couples into the disk, but some couples back out.

It should be noted that from an electric field point of view, the total power coupled out of the disk is a superposition of light that is not coupled into the disk, $T_{AB}A_1$, and

light that is coupled out of the disk $i\alpha_1 A_2$. Therefore critical coupling is seen when resonant light inside the disk just achieves the correct phase and amplitude to cancel the input light that is not coupled into the disk, $|i\alpha_1 A_2| = |T_{AB} A_1|$. Therefore, overcoupled output electric field has a π phase shift as compared to the input optical field, since $|i\alpha_1 A_2| > |T_{AB} A_1|$ the . Similarly, undercoupled light is in phase with the input light since $|i\alpha_1 A_2| < |T_{AB} A_1|$.

3.5 Optical losses and the quality factor Q

Optical losses and photon lifetime of the resonator can be extrapolated from the quality factor Q . The quality factor is defined as $Q \equiv \omega E / P = f / \Delta f_{FWHM} = \lambda / \Delta \lambda_{FWHM} = \omega \tau_c$ where $\omega = 2\pi f$, E is the energy stored in the resonant mode, P is the power dissipated in the cavity, Δf_{FWHM} is the full-width at half maximum of the spectral peak at optical frequency f , and τ_c is the $1/e$ photon lifetime. The measured optical Q of a LiNbO₃ disk with diameter 5.85 mm is shown in Figure 29. This mode was measured using the two-prism coupling scheme and a wavelength tunable DFB laser input with linewidth < 0.5 MHz.

The total measured optical Q including the effects of coupler loading is greater than 4×10^6 near $\lambda = 1550$ nm wavelength and $\Delta f_{FWHM} = 48$ MHz. We find for this Q , the photon cavity lifetime is $\tau_c = 3.4$ ns, resulting in an effective photon interaction

length with the RF field of greater than 50 *cm*. The effective number of round trips per photon from $(c\tau_c)/(n_{opt}2\pi R)$ is approximately 26. Although one sacrifices bandwidth with this resonant configuration, the effective photon interaction length, and hence voltage sensitivity, is more than 25 times that of a conventional Mach-Zehnder LiNbO₃ modulator. Assuming the Q is dominated by optical scattering at the disk edge, we define a distributed loss constant α as the loss per unit length, where $\alpha = n_{opt}/(c\tau_c) = 0.02 \text{ cm}^{-1}$. This is 10 to 100 times better than typical waveguide scattering in semiconductor and conventional LiNbO₃ waveguides, and demonstrates an ability to obtain a high-quality, low-loss optical polish.

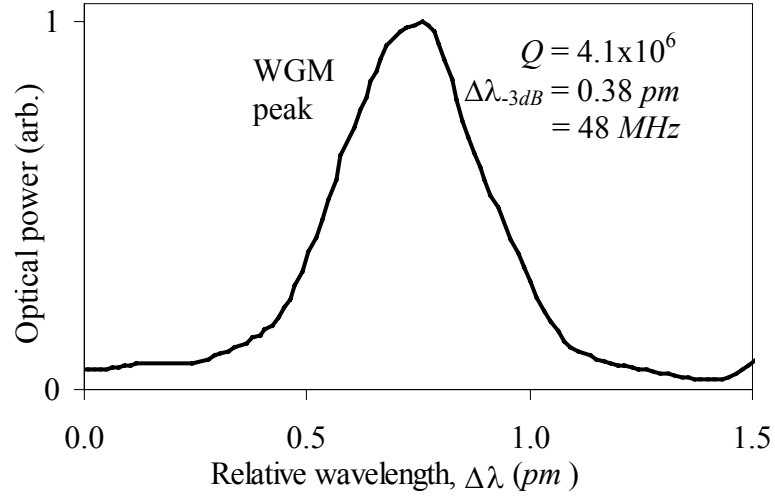


Figure 29. Measured optical resonance near wavelength $\lambda = 1550 \text{ nm}$ of a z-cut LiNbO₃ disk-shaped resonator with gold electrodes and optically polished curved side-walls. The measured Q of this device is in excess of 4×10^6 .

3.6 Optical spectrum

As discussed in section 3.2 both TE and TM polarized WGM modes can be excited in the LiNbO₃ microphotonic resonator. When TE-polarized WGM modes are excited within the LiNbO₃ microphotonic resonator the detected optical spectrum shows peaks corresponding to the free spectral range (FSR) of the resonant cavity. This FSR is defined as $\Delta f_{FSR} \approx c/(n_{opt}2\pi R)$, where n_{opt} is the optical refractive index, and R is the radius of the disk. It should be noted that $1/\Delta f_{FSR}$ is equal to the round trip time of the cavity $\tau_{disk} = (n2\pi R)/c$.

Figure 30 shows typical experimental results using the two-prism coupling scheme and a tunable DFB laser to scan the entire free spectral range of the disk. A disk of diameter $2R = 5.85 \text{ mm}$, and thickness $d = 0.74 \text{ mm}$ exhibited a FSR of 7.57 GHz (60.6 pm) for TE optical modes, and FSR = of 7.57 GHz (63 pm) for TM optical modes. Within the uncertainty of the measured disk radius, these values agree with the equation for Δf_{FSR} .

Experimental spectra consistently show TM modes are easier to couple, where TE modes tend to have higher Q . In addition, Figure 30(a) shows the numerous TE polarized optical modes excited when the alignment is optimized for maximum optical throughput. Figure 30(c) shows the resulting optical spectrum when alignment is optimized for single mode excitation.

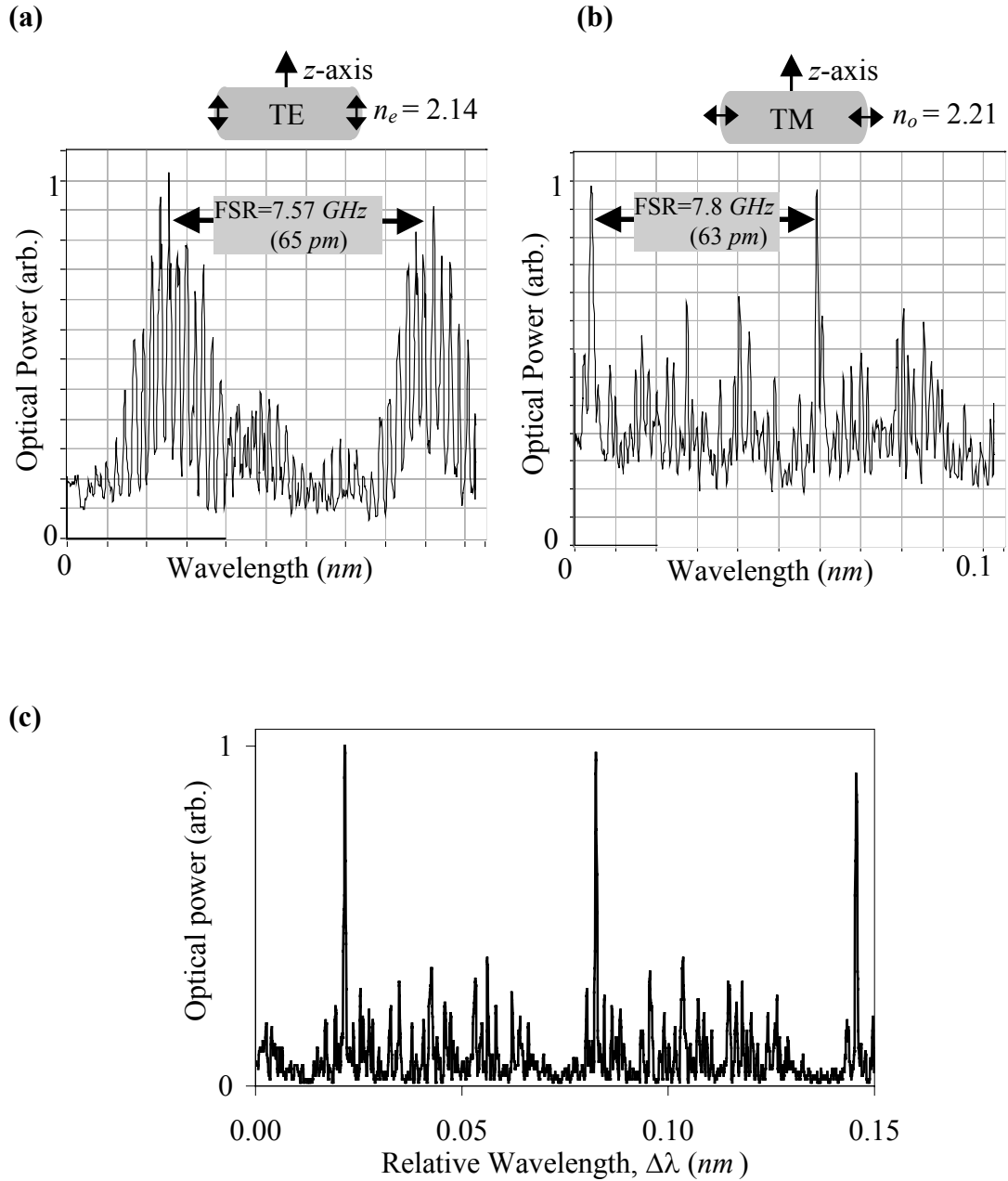


Figure 30. (a) Optical spectrum of TE polarized light. The disk cross-section above the spectra show electric field polarization and z -axis orientation for TE polarized light. This shows the many modes observed when the alignment is optimized for maximum optical throughput. (b) Optical spectrum of TM polarized light. The disk cross-section above the spectra show electric field polarization and z -axis orientation for TM polarized light. The disk used has a diameter 5.85 mm and thickness of 0.7 mm . Wavelength is $1.5 \mu\text{m}$. (c) Optical spectrum for TE polarized light when alignment is optimized for single optical mode excitation.

3.7 Optical pulse response

Injecting optically pulsed light into the passive resonator allows us to monitor the optical build-up and decay times of the cavity. Laser light from a continuous wave (CW) 1.55 μm DFB laser is on-off modulated by passing the light through a LiNbO₃ Mach-Zehnder optical modulator (MZ). An electrical 80 ns pulse with 800 ns repetition rate is applied to the MZ modulator with a resulting 0.7 ns 1/e risetime as shown in Figure 31(a). The light is then coupled into the microresonator using the two-prism coupling scheme.

The optical pulse output is shown in Figure 31(b). An exponential fit to the data shows a risetime $\tau_{1/e}$ of 13.8 ns. This results in a calculated -3dB rolloff of $\Delta f = (2\pi\tau_{1/e})^{-1} = 12 \text{ MHz}$. The cavity decay time was similar. The full-width-half-max of the optical decay time is $2\Delta f = 24 \text{ MHz}$ (to account for $\pm\Delta f$). The experimentally measured spectral width of the optical cavity mode (which is equally represented by the cavity Q) is 65 MHz.

The difference in these numbers are attributed to the excitation of a higher Q mode during the optical pulse response experiment. That these numbers are close and within a factor of three demonstrate that passive optical rise and fall times are limited by the buildup time of the optical resonance (Q limited).

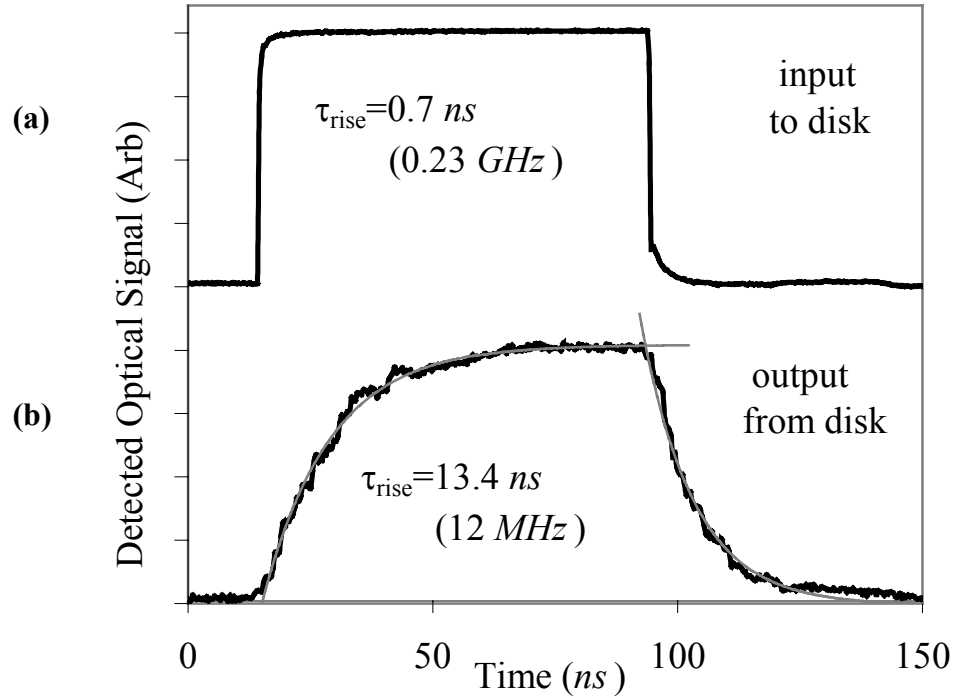


Figure 31. (a) Optical pulse used to probe the rise and decay times of the passive optical cavity. The 80 ns pulse has a $1/e$ risetime of 700 ps. (b) Q limited optical pulse output of passive microresonator cavity.

3.8 Electrical material properties

An important technical issue concerns the material properties of LiNbO_3 at high RF frequencies. Poor quality material can have dielectric losses that limit Q in RF circuits. Experimental results have shown that LiNbO_3 should be able to support low loss RF fields to at least 140 GHz [78]. To verify this ourselves, and in addition begin to understand resonant RF fields in the LiNbO_3 disk, we side-couple the RF field from a strip-line into a passive LiNbO_3 disk where we excite RF frequency WGM. The LiNbO_3 disk is 8 mm in diameter and 3.3 mm thick. The z -axis of the crystal is oriented normal the plane of the microstriplines as shown in Figure 32(a). In Figure 32(b) we see the resulting RF WGM Q in the range of 700 at 19 GHz. This

relatively large Q shows promise that the low loss electrical nature of the material will not limit operation at large RF frequencies.

It is also noted that the dielectric response of LiNbO_3 changes significantly from optical frequencies (refractive index near 2.1) to RF frequencies (refractive index greater than 5). It is these properties which may permit simultaneous resonance of RF and optical fields in the LiNbO_3 disk architecture.

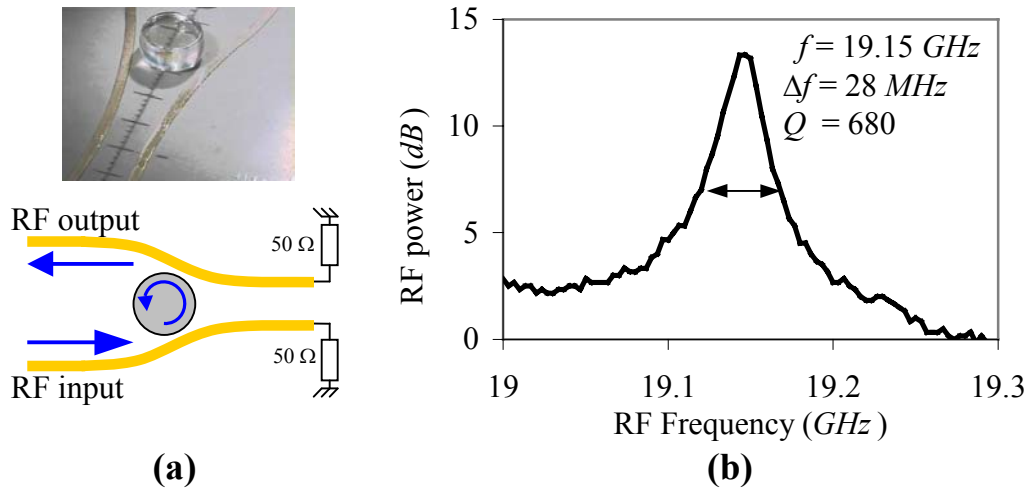


Figure 32. (a) Picture and schematic showing the strip-line geometry used to couple the RF electromagnetic field into and out of the passive resonator. (b) Measured RF resonance near 19.15 GHz with a measured Q in the LiNbO_3 disk of 680. The LiNbO_3 disk is 8 mm in diameter and 3.3 mm thick. The z -axis of the crystal is oriented normal the plane of the striplines in (a).

3.9 Summary

An introduction to the whispering gallery modes, and principles for coupling to those modes will permit a deeper understanding of the results presented in the next chapter. This understanding has been put to use experimentally to achieve 25% optical coupling into whispering gallery mode resonances of the LiNbO_3

microphotonic resonator. Optical Q of 4×10^6 has been achieved, and proves the ability to fabricate LiNbO_3 disks with high-quality polished curved sidewalls. RF WGM excitation using stripline coupling demonstrates that the LiNbO_3 material system will not limit the extension of experiments to large RF frequencies. In addition, resonance spectra and pulse response of the passive LiNbO_3 cavity shows features similar to that of silica spheres. Therefore, WGM coupling is not limited by the birefringent nature of LiNbO_3 .

3.10 References

- [68] Stratton, J.A.: 'Electromagnetic theory', (McGraw-Hill Book Company, New York, 1941)
- [69] Reitz, J. R., Milford, F. J., and Christy, R. W., 'Foundations of electromagnetic theory, third edition', (Addison-Wesley Publishing Company, NY, 1980), ISBN 0-201-06332-8
- [70] Frateschi, N. C.; and Levi, A. F. J.: 'The spectrum of microdisk lasers', *J. Appl. Phys.*, 1996, **80**, pp. 644-653
- [71] Little, B. E., Laine, J. P., and Haus, H. A.: 'Analytic theory of coupling from tapered fibers and half-blocks into microsphere resonators', *J. Lightwave Technol.*, 1999, **17**, (4), pp. 704-708
- [72] Knight, J. C.; Dubreuil, N.; Sandoghdar, V.; Hare, J.; Lefevre-Seguin, V.; Raimond, J. M.; and Haroche, S.: 'Mapping whispering-gallery modes in microspheres with a near-field probe', *Opt. Lett.*, 1995, **20**, pp. 1515-1517
- [73] Gorodetsky, M. L. and Ilchenko, V. S.: 'High-Q optical whispering-gallery microresonators: precession approach for spherical mode analysis and emission patterns with prism couplers', *Opt. Comm.*, 1994, **113**, pp. 133-143
- [74] Little, B., Laine, J., and Chu, S.: 'Surface-roughness-induced contradirectional coupling in ring and disk resonators', *Optics Lett.*, 1997, **22**, (1), pp. 4-6
- [75] Lee, D. L.: 'Electromagnetic Principles of Integrated Optics', (John Wiley & Sons, NY, 1986)

- [76] Hecht, E.: 'Optics', (Addison-Wesley Publishing Company, Inc., NY, 1987)
- [77] Schiller, S., Yu, I., Feher, M., and Byer, R.: 'Fused-silica monolithic total-internal-reflection resonator', *Optics Lett.*, 1992, **17**, (5), pp. 378-380
- [78] Robertson, W. M., Arjavalingham, G., Kopsay, G. V., 'Broadband microwave dielectric properties of Lithium Niobate', *Electron. Lett.*, 1991, **27**, pp. 175-176

Chapter 4

LiNbO₃ microphotonic modulator

4.1 Introduction

The central attribute of the LiNbO₃ microphotonic resonator is that of direct electrical-to-optical conversion. An important design innovation is the resonator's ability to have both optical and RF signals simultaneously in resonance. To exploit these attributes, we first investigate the DC electrical response of the LiNbO₃ disk. We then investigate the modulation response of the resonator.

There are two RF modulation bands of interest. Base-band modulation at frequencies on the order of the optical Q of the modulator (10's of MHz), and out-of-base-band modulation at frequencies of 10's of GHz . The experimental results of base-band modulation and theory explaining these results are presented. Theory, simulation, and data to show efficient out-of-band modulation at frequencies up to 38 GHz are then presented. Finally, linearity measurements and system issues are addressed.

4.2 Direct-contact static and base-band experimental setup

A schematic of the experimental setup used for simultaneous electrical and optical coupling is shown in Figure 33. A tunable DFB laser of wavelength $1.55 \mu\text{m}$ and linewidth less than 500 kHz is incident on the side face of the input diamond prism. Light is coupled out of the disk using either the one or two prism coupling configuration. Electrical contact to the microphotonic modulator is achieved by either patterning metal ring electrodes directly on the disk, or by placing a flat, thin, highly conductive metallic ring directly on top of the disk. The ring geometry is used to increase overlap of the RF and optical field. Placing the disk on a gold plated copper block serves as the ground plane. Some disks have metal patterned on the bottom of the disk for better grounding. Electrical contact to the ring is by direct SMA launch.

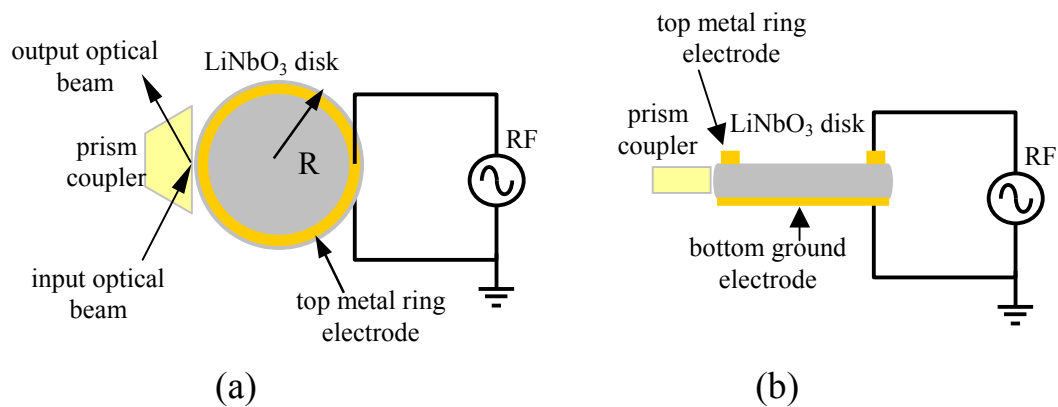


Figure 33. (a) Top view of single prism coupling setup. (b) Side cross-section of single prism coupling setup.

4.3 Static voltage response of the microphotonic resonator

Ideally, the electro-optic effect in z -cut LiNbO_3 changes only the optical refractive index of the medium as a function of time, $n(t)$. For time $t > 0$ the resonant frequency of light in the cavity changes adiabatically as the index of refraction changes, $f(t) \sim f_0 n_0 / n(t)$, where f_0 is the unperturbed resonant frequency at time $t \leq 0$ and n_0 is the refractive index at time $t \leq 0$. Application of a static voltage V_{DC} along the crystal's z -axis will shift the WGM resonant wavelength $\lambda_0 = 2\pi c / \omega_0$ due to a change of refractive index Δn_{opt} . If the applied DC electric field is $E_{DC} = V_{DC} / d$, where d is the thickness of the disk, the electro-optic effect changes the refractive index along the z -axis by $\Delta n_{opt} = n_e^3 r(33) E_{DC} / 2$, where $r(33) \sim 30.8 \times 10^{-12} \text{ m/V s}$ at an optical wavelength of $\lambda = 1.55 \mu\text{m}$. Similarly, if the electric field is applied in the x - y plane, the change in the refractive index would be given by $\Delta n_{x,y} = n_o^3 r(13) E_{DC} / 2$, where $r(13) \sim 8.6 \times 10^{-12} \text{ m/V}$ at an optical wavelength $\lambda = 1.55 \mu\text{m}$. As described in Chapter 3, m_{opt} is approximately the number of optical wavelengths along the disk circumference, and from $m_{opt} \lambda = n_{opt} 2\pi R$, the shift of the WGM resonant wavelength by a DC electric field is $\Delta \lambda_{DC} = 2\pi R \Delta n_{opt} / m_{opt}$.

To demonstrate electrically controlled optical resonance tuning in a microphotonic disk, an electric field is applied perpendicular to the top disk face (parallel to the z -axis). This was accomplished by applying a DC voltage to a metal ring on a LiNbO_3

resonator similar to that shown in Figure 34(a). As shown in Figure 34(b), a TE-polarized mode may be tuned 70 MHz (0.56 pm) with an applied DC electric field of 10.8 V/mm (8 V, $d_{\text{disk}} = 0.74$ mm). Theoretically, we expect the frequency to shift by ~ 140 MHz. The difference is attributed to incomplete overlap of the metal ring electrode with the disk edge. By rotating the optical input polarization, we find that $\Delta\lambda_{TE} / \Delta\lambda_{TM} = 3.5$ which agrees well with theory.

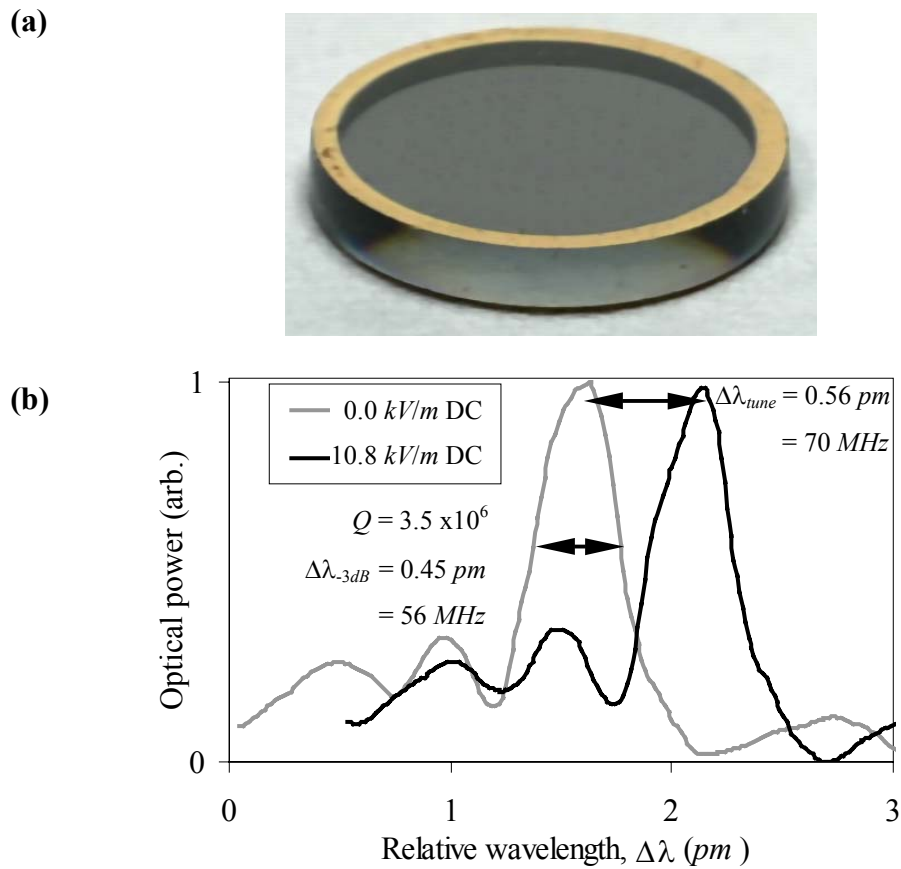


Figure 34. (a) Photograph of a z-cut LiNbO₃ disk-shaped resonator with optically polished curved side-walls. Gold electrodes are placed in an annulus around the disk to increase the overlap of electrical bias and optical fields. The dimensions of the disk are radius $R = 5.8$ mm and thickness $d = 0.74$ mm. (b) Measured shift in resonant wavelength due to application of 8 V DC bias between the top and bottom electrodes of the disk shown in (a). The change in resonant wavelength is 0.07 pm/V.

4.4 Base-band RF modulation

Initial base-band RF modulation experimental results are obtained using a LiNbO_3 disk with a radius $R = 3 \text{ mm}$, a thickness of $d = 0.74 \text{ mm}$, and a non-optimized RF electrode annulus of 0.5 mm width. For this disk, the capacitance of $C = 5 \text{ pF}$ results in a $50 \text{ } \Omega$ RC limited -3 dB roll-off in electrical response of greater than 600 MHz . With base-band modulation, the Q of the cavity determines the small-signal RF response of this modulator. This is evident from results of measurement shown in Figure 35(a) in which the 32 MHz -3 dB bandwidth of the RF response is half of the 60 MHz full-width-half-maximum of the optically measured spectral resonance. Figure 35(b) shows time domain results of direct modulation of the same LiNbO_3 disk through application of a 10 MHz square wave. The small distortion in the square wave is due to improper electrical impedance matching. The results shown in this Figure also demonstrate that the natural acoustic and piezoelectric response of LiNbO_3 is not a limiting factor for frequencies beyond tens of kHz .

Base-band modulation can be understood from the diagram in Figure 36(a) where we vary the optical resonance by modulating the microresonator with a sinusoidal voltage V_0 at some frequency ω_0 . The two peaks shown are resonance peaks at $\pm V_0$ for photons exiting the LiNbO_3 resonator. For modulation frequencies less than the Q of the modulator (base-band), the optical field inside the disk builds up or decays faster than the applied voltage can shift the resonant frequency of the optical cavity.

This is similar to the response of a RC circuit to applied frequencies below the RC time constant.

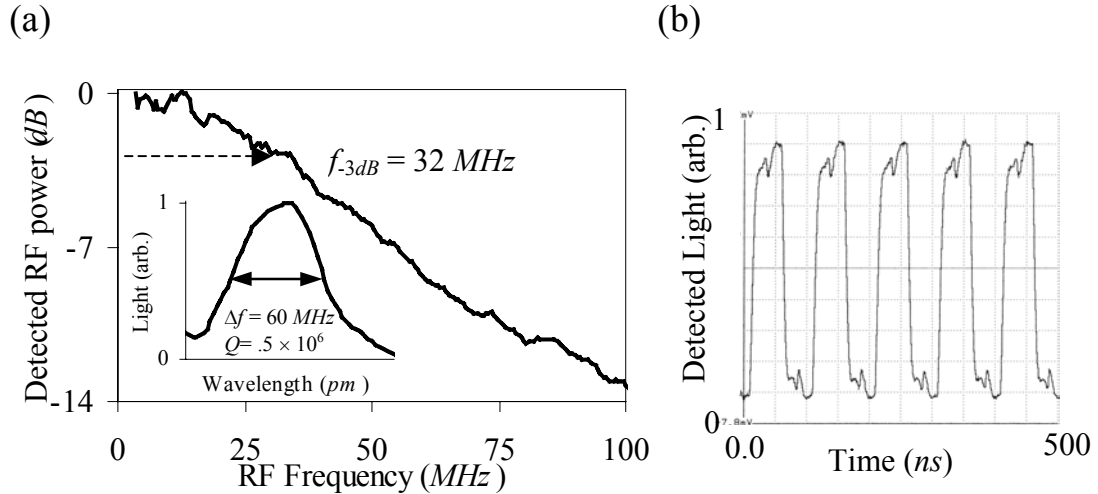


Figure 35. (a) Detected small-signal RF optical modulation as a function of frequency for a LiNbO_3 disk of radius $R = 3 \text{ mm}$. The inset shows the corresponding optical line-width of the high-Q whispering gallery mode resonance. (b) Time domain modulation of the LiNbO_3 by application of a 10 MHz square wave.

For example in Figure 36(a), if the light enters the cavity at a wavelength λ_2 , the output light will be amplitude modulated between points (a) and (b). At λ_1 , the resulting modulation is frequency doubled in a fashion similar to frequency doubling in a Mach-Zehnder modulator. In Figure 36(b) we experimentally show the amplitude modulation as a function of wavelength. We apply an electrical modulation of 100 kHz while sweeping the wavelength at 20 Hz . The black curve shows the detected optical signal vs. wavelength for zero voltage on the disk. By tuning the wavelength at a rate much slower than the applied modulation, the detected signal on the oscilloscope is a band between the maximum and minimum

amplitude for a fixed wavelength (gray curve). The gray curve shows optical modulation at the modulating frequency only. Consequently frequency doubled modulation is not shown.

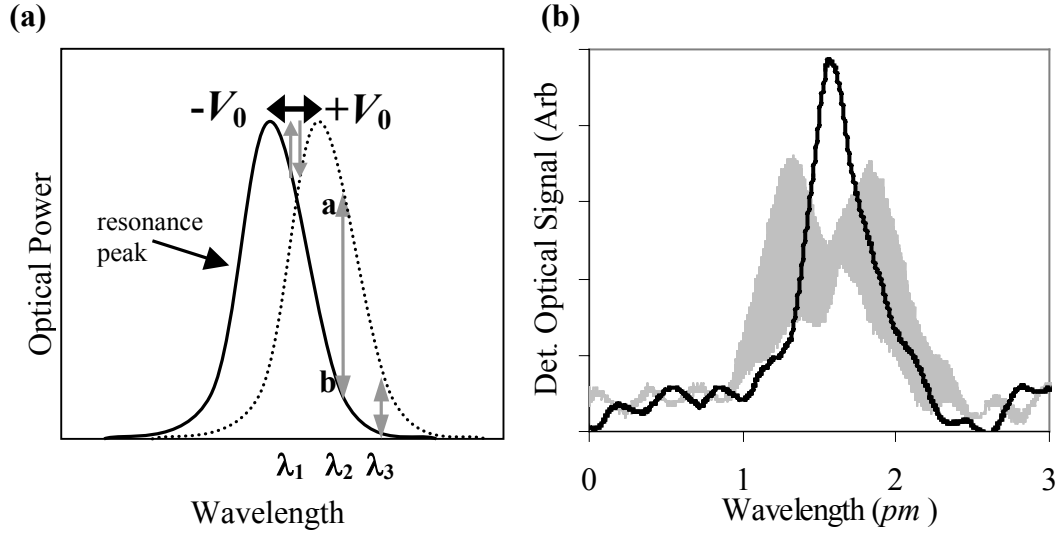


Figure 36. (a) Base-band modulation mechanism. Maximum ($+V_0$) and minimum ($-V_0$) shift of resonance frequency during base-band modulation. Input at the wavelength λ_2 will result in amplitude modulation between points a and b. Input at the wavelength λ_1 will result in frequency doubling. (b) 100 kHz optical modulation amplitude versus wavelength for an applied 100 kHz modulation. Black line is for zero applied modulation. The gray band is the modulation amplitude vs. wavelength. Modulation at doubled frequencies (200 kHz) is not shown. .

4.5 Electrical pulse response of the LiNbO₃ resonator

Passive cavity rise and fall times are investigated in Chapter 3. In this section, we investigate the active cavity rise and fall times of the LiNbO₃ microresonator. Application of an electrical field has been shown to shift the resonant frequency of the optical mode. By generating an electrical pulse, we can very quickly and

adiabatically shift the disk resonant wavelength from the resonant wavelength when the electrical pulse is off (λ_{off}) to the resonant wavelength when the pulse is on (λ_{on}).

A DC optical input of wavelength λ_{laser} is coupled to the disk. With zero applied electrical field, the resonant wavelength of the disk is λ_{off} . A RF pulse is then applied to the microresonator such the optical resonance shifts to λ_{on} for the duration of the pulse. If $\lambda_{laser} = \lambda_{on}$, the laser is at the resonant wavelength of the cavity, and the optical field inside the cavity will begin to build. This will generate an output optical pulse.

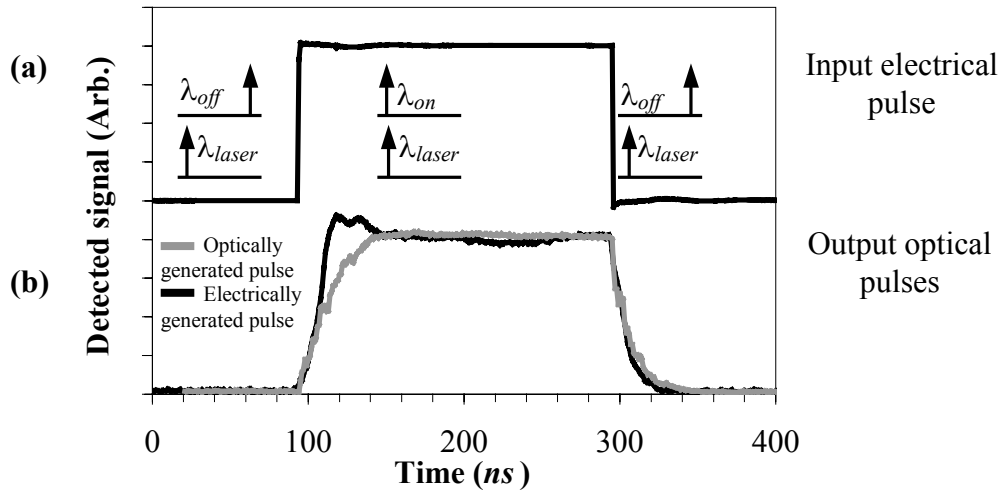


Figure 37. (a) Electrical RF pulse imparted on the ring electrode of the disk. Pulse width = 200 ns, repetition rate = 10 μ s, and pulse risetime of 125 ps. (b) Detected optical pulse generated by the input electrical pulse. Overlaying this is a pulse generated by pulsing the input light with no applied RF.

Figure 37(a) shows the applied electrical pulse with 200 ns width, 10 μ s repetition rate, and 125 ps risetime. Figure 37(b) shows the resulting detected optical pulse.

An exponential decay time of 12.5 ns is measured. The transient in the risetime is a result of improper impedance match of the electrical input pulse. We compare this result to the optical results of the passive cavity (see section 3.7). The second curve of Figure 37(b) shows the output response of a 700 ps risetime input optical pulse. This shows the similarity between the two experiments. This shows conclusively that the electrically induced cavity rise and decay times are no different from the risetime (Q) of the passive cavity. Reversing the experiment such that $\lambda_{laser} = \lambda_{off}$ with no electrical field, resulted in the cavity switching off at the start of the pulse, and then on at the end of the pulse with similar rise and fall times.

We next investigate whether electrically shifting off the resonant frequency of the cavity will hasten the decay of photons that are already in the cavity. Pulsed laser light with a rise and fall time of 700 ps is incident on the disk. An expanded view of the falling edge of the resulting optical output is shown in Figure 38(b). At time $t = 0$ in the figure the light is on, and $\lambda_{laser} = \lambda_{off}$. Light is then turned off and the optical field begins to decay with a photon decay time constant dependent on cavity Q . After the input light is turned off, we apply the electrical rising edge shown in Figure 38(a). Now, the resonant frequency of the cavity shifts to λ_{on} . The resulting optical output is shown in Figure 38(b), and is of no significant difference to having no electric field present. This concludes that the decay time of the cavity is independent of the resonant frequency of the disk.

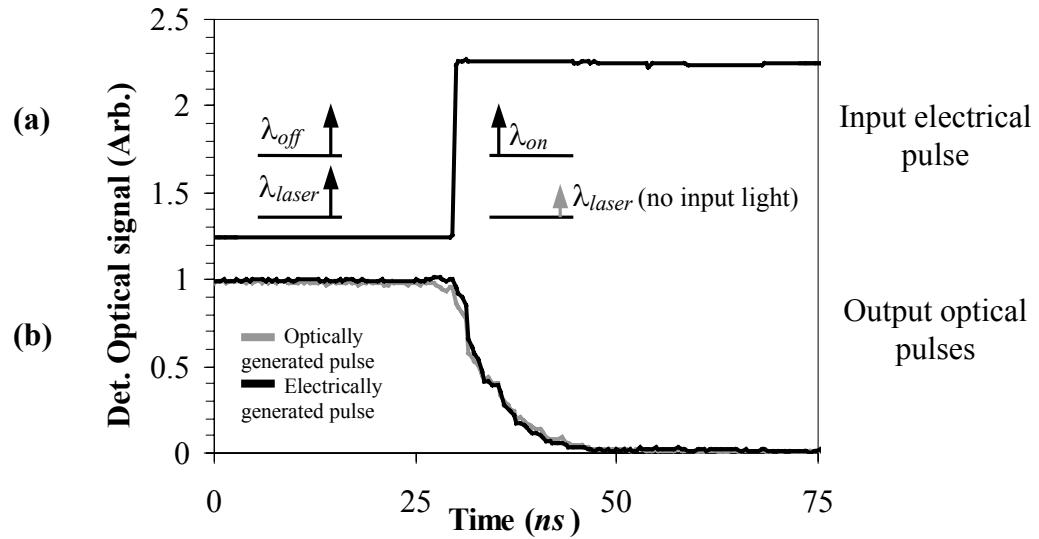


Figure 38. (a) Electrical RF pulse imparted on the ring electrode of the disk. Pulse width = 200 ns, repetition rate = 10 μ s, and pulse risetime of 125 ps. (b) Detected optical decay time generated by the input electrical pulse. Overlaying this is the decay time of a pulse generated by pulsing the input light with no applied RF.

4.6 Out-of-band modulation

In practice, conventional Mach-Zehnder traveling-wave devices are bandwidth limited by electrical attenuation and phase-mismatch of the electrical and optical waves over the active length of the device. This is a result of the difference in propagation speeds of the optical and electrical waves. It is very difficult to design such devices for operation at *mm*-wave frequencies.

In contrast, the whispering gallery mode resonator is of small enough dimensions that its RF properties can be approximated using a lumped element circuit model. As will be shown, these devices are not limited to operation at relatively low RF

frequencies because the physics governing performance of a microphotonic modulator is different than LiNbO₃ Mach-Zehnder travelling-wave modulators. However, RF design and modulator geometry for tens of GHz operation of the LiNbO₃ microresonator is a very subtle problem, and must be explored.

4.6.1 Introduction to RF resonator design principles

A basic principle in RF resonator construction is the need for a non-uniform applied RF electric field. Initial modulation experiments demonstrated this principle using a symmetric metal walled RF cavity, such as is shown in Figure 17. The excited RF mode resulted in uniform electric field along the *c*-axis of the crystal. A LiNbO₃ optical resonator with round trip time τ , and frequency $f = 1/\tau$ was placed symmetrically in the cavity. It will be shown later that the applied RF field frequency f_{RF} must be equal to, or a multiple of the optical round trip frequency f of the disk. This condition allows the applied RF phase shifts to be added constructively.

When $f_{RF} = f$, the phase shift induced on the photons during the positive first half of the RF field cycle, is exactly cancelled by the negative phase shift from the second half of the RF field cycle. The uniform electric field of the metal walled RF cavity resulted in a null in the experimental modulation results. This demonstration verified the need for design of a cavity with non-uniform RF electric field lines.

Direct patterning of metal electrodes on the LiNbO₃ resonator is a more attractive approach than design of a non-uniform metal walled cavity. This approach permits definition of the RF cavity by standard lithography used in the microelectronics industry. In addition, improved control of the overlap of RF and optical electric fields is inherent to this approach.

4.6.2 Resonant periodic metal-electrode modulation approach

One possible solution that achieves efficient high frequency modulation and a non-uniform RF electric field is the resonant periodic metal-electrode modulation approach. By patterning the metal electrodes periodically about the disk circumference, as shown in Figure 40(b), it is possible to obtain a resonant optoelectronic modulation response at large RF frequencies. It will be shown that electrode design is critical to this approach.

Theory of periodic metal-electrode modulation

Figure 39 shows the configuration for this approach. As in a standard waveguide Mach-Zehnder LiNbO₃ amplitude modulators, input light is split into an active and passive path. Optical path lengths of the two arms are matched. The active section of the waveguide modulator is replaced with an active microphotonic resonator. Light is then recombined after the disk. This method allows for conversion of the disk's phase modulation to amplitude modulation at large RF frequencies.

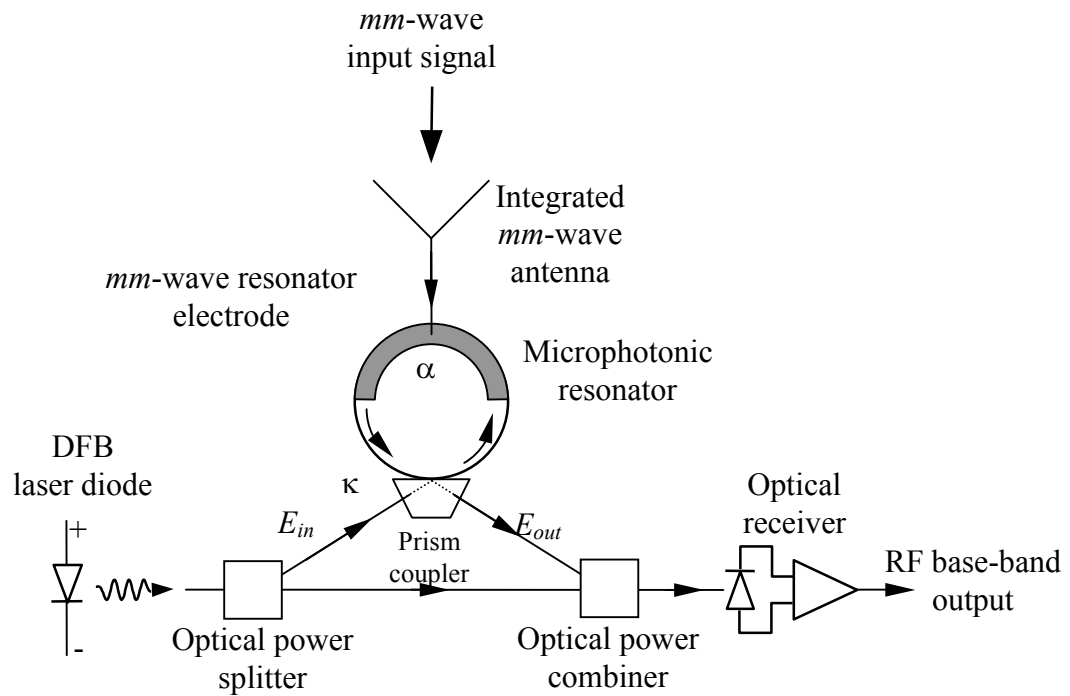


Figure 39. Schematic showing the receiver proposed for *mm*-wave RF detection. An electromagnetic wave received at a RF antenna feeds electrodes of the microphotonic modulator. The modulator directly converts the RF signal to an optical carrier via the electro-optic effect. The resulting phase-modulated optical signal is converted to amplitude-modulation through the use of a standard Mach-Zehnder configuration.

It will be shown that the RF modulation frequency of the microphotonic resonator is determined by the free spectral range (FSR) of the optical resonator and the spatial pattern of the metal-electrode structure. The frequency of the RF carrier f_{RF} should be an integral multiple m of the optical FSR, f_{FSR} , where $f_{FSR} = 1 / \tau_{disk} = c / n_{opt}2\pi R$, τ_{disk} is the optical round-trip time of the disk, and R is the disk radius [see section 3.4]. A periodic metal electrode structure permits operation of the modulator well

beyond a typically 20 GHz -3 dB roll-off of conventional commercial LiNbO₃ modulators.

This is understood by first considering an ideal non-resonant single optical-pass configuration ($\kappa = 1$). In this case, light is coupled into the disk to minimize the resonant effects of the disk, and maximize the single pass throughput of the light. We initially assume ideal 100% coupling ($\kappa = 1$) into and out of the disk. In this limit, the response of the disk is that of a traditional LiNbO₃ amplitude modulator with the advantage of compact size, and potential for integration not achievable in traditional modulators. If we consider an applied RF sinusoidal electric field of the form $E_{RF} = E_{dc} + E_m \sin(\omega_{RF}t)$, we will find that the phase modulation in a disk of circumference L will go as $\Phi(L) = \beta_{dc}L + \delta(L) \sin(\omega_m t - \phi(L))$, such that

$$\begin{aligned}\beta_{dc} &= \frac{\omega n^3}{2c} E_{dc} r_{33} \\ \delta(x) &= \beta_{RF} L \frac{\sin(\Delta)}{\Delta} \\ \Delta(x) &= \frac{\omega_{RF}}{2c} (n_{rf} - n)x \\ \beta_{RF} &= \frac{\omega n^3}{2c} E_m r_{33} \\ \phi(x) &= \frac{\omega_{RF}}{2c} (n_{RF} - n)x\end{aligned}$$

where $k = n\omega/c$, $k_{RF} = n_{RF}\omega_{RF}/c$, and ω , ω_{RF} are the optical and RF frequencies, and $x = L$. The term $(n_{RF} - n)$ is the phase match condition. If a stationary electric field

is applied along the z -axis, we have $k_m = n_m = 0$ in the above equations. We therefore never have phase matching at high frequencies. The RF phase amplitude will fall off as a sinc function with respect to frequency. If we recombine the light of the two arms of the Mach Zehnder modulator, the resulting intensity detected in a square wave detector is $I = I_0 + I_{RF}\sin(\Phi(L))$.

The following sections show simulation results using a Mach-Zehnder configuration similar to that shown in Figure 39. It will be shown later that the Mach-Zehnder configuration is not required. Amplitude modulation can be achieved without the use of interference from a reference signal. A correctly implemented resonant disk provides its own effective reference allowing AM modulation from phase modulation with efficiency better than that of the Mach-Zehnder configuration.

4.6.3 Single pass periodic metal-electrode modulation simulation

The simulated modulation response of a solid-ring electrode is just that of a conventional Mach-Zehnder interferometer as shown in Figure 40(a). We assume a radius $R = 3.18 \text{ mm}$ which gives a FSR of $f_{FSR} = 7.03 \text{ GHz}$. As expected, the modulator has a sinc function response with little efficiency at large values of f_{RF} . The -3 dB point at approximately 5 GHz is due to the "walk off" of the traveling optical wave with respect to the applied RF field. The first null in the frequency response at about 7 GHz is where the round-trip time of the optical wave τ_{disk} equals

the period $T = 1 / f_{RF}$. This occurs because during the positive part of the RF electric-field's cycle, the disk's optical field obtains a positive phase-shift ("+" in Figure 40(a)) which is exactly canceled during the negative cycle ("-") in Figure 40(a)).

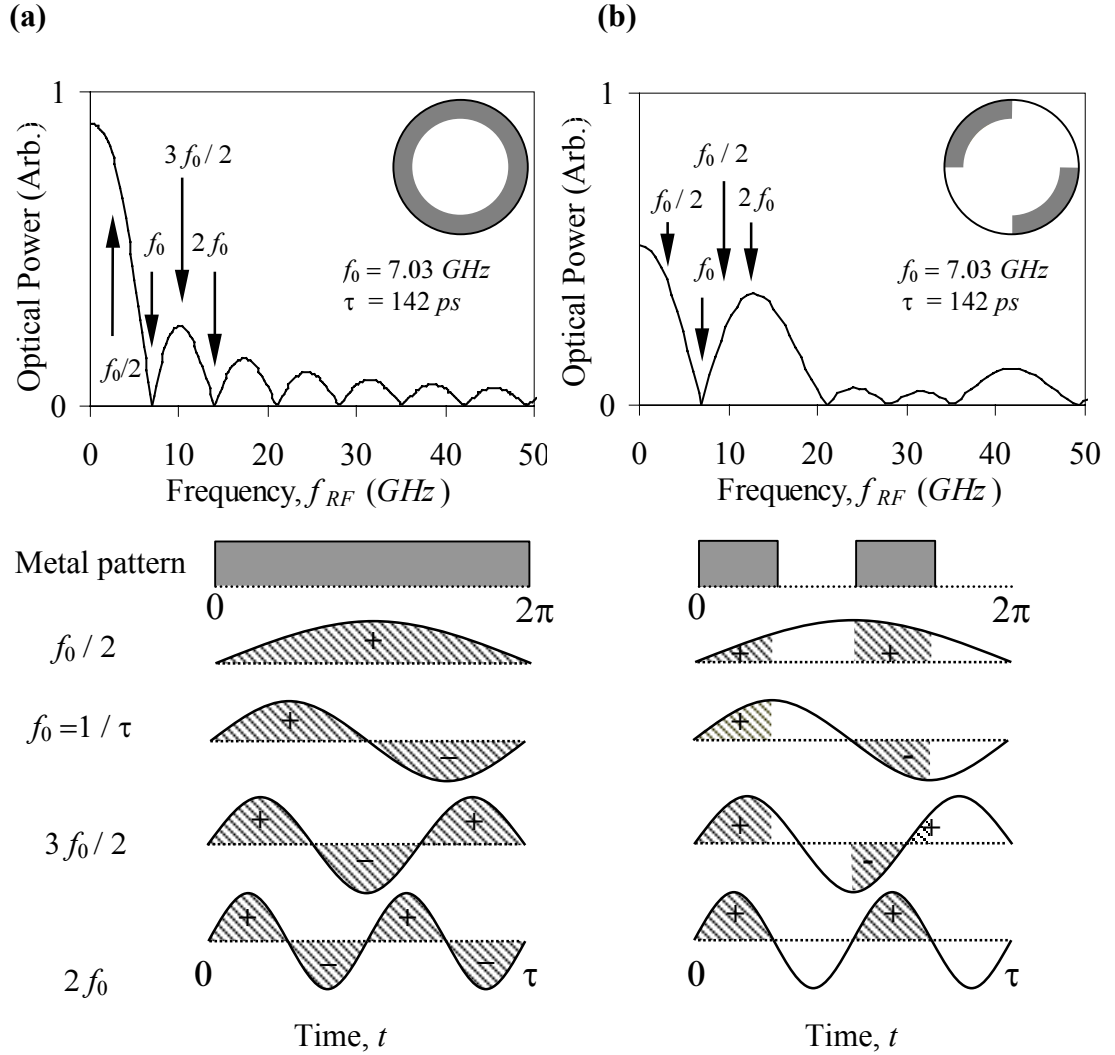


Figure 40. Calculated response of a microphotonic-based opto-electronic modulator with the indicated periodic metal-electrode structures and $f_0 = 7 \text{ GHz}$. (a) A $R = 3.18 \text{ mm}$ LiNbO₃ disk modulator with $\kappa = 1$ and a continuous ring-electrode. (b) $\kappa = 1$ optical-coupling with a split 4-segment ring-electrode showing a peak in opto-electronic response at 14 GHz .

Similarly, when the applied RF frequency is any integer multiple m of the optical round-trip frequency ($f_{RF} = m / \tau_{disk}$), a null in the frequency response results. The maximum modulation occurs when the applied RF frequency is at odd half integer multiples ($f_{RF}=(m/2)*1/\tau_{disk}$) for odd m , where the maximum intensity goes as $1/m$ (m odd).

Modulation at the nulls may be enhanced if the electrode structure is modified as, for example, shown in Figure 40(b). In this case, while the RF electric-field at frequency $f_{RF} = 2 f_{FSR}$ is positive, light passing through a region with an electrode receives a positive phase-shift. While the RF electric-field is negative, the light passes through a region without an electrode and receives no phase-shift. Results of calculations given in Figure 40(b) show that use of such a patterned two-electrode structure enables efficient modulation near 14 GHz. The loss in base-band efficiency in Figure 40(b) compared to the ring electrode of Figure 40(a) is a result of only half the disk being patterned.

4.6.4 Resonant periodic metal-electrode modulation simulation in the Mach-Zehnder configuration

For the optically resonant case ($\kappa < 1$), photons make a number of round trips in the resonator, thereby interacting with the RF field on multiple passes. For large optical coupling, the extra round trips increase the total phase shift seen by any individual photon. This results in improved sensitivity to the applied RF field. This optical

phase shift can then be converted to amplitude modulation by interfering with the second arm of the Mach-Zehnder as shown in Figure 39. As the optical coupling decreases toward that of critical coupling each photon will make many more round trips. The optical output is then a superposition of many optical waves. These waves will then amplitude modulate by interfering with themselves, and the second arm of the Mach-Zehnder is unnecessary.

The modulated optical electric-field resulting from multiple round-trips may be obtained in Chapter 3 from the expressions

$$E_{out1}(t) = \left[\sqrt{1 - \kappa_1^2} - \frac{\kappa_1^2}{\sqrt{1 - \kappa_1^2}} \sum_{p=1}^{\infty} \rho_1^p e^{i \sum_{q=0}^{p-1} [\phi_1(t - \tau_2 - q\tau) + \phi_2(t - q\tau)]} \right] E_{in}(t)$$

$$\rho_1 \equiv \alpha \sqrt{1 - \kappa_1^2} \sqrt{1 - \kappa_2^2} e^{i\omega\tau}$$

where $E_{out1}(t)$ is the electric-field exiting the prism, $E_{in}(t)$ is a the field entering the prism, and p is the round trip number. This equation assumes that the incident light can be approximated by a monochromatic wave. The above equation simplifies when the applied RF electric field frequency is the same as the optical FSR of the disk ($f_{RF} = 1 / \tau$) and the metal electrode is a solid ring. In this case, the expression is

$$E_{out1}(t) = \left[\sqrt{1 - \kappa_1^2} - \frac{\kappa_1^2}{\sqrt{1 - \kappa_1^2}} \left\{ \frac{\rho'_1}{1 - \rho'_1} \right\} \right] E_{in}(t)$$

$$\rho'_1 \equiv \alpha \sqrt{1 - \kappa_1^2} \sqrt{1 - \kappa_2^2} e^{i(\omega\tau + \phi_{tot}(t))}$$

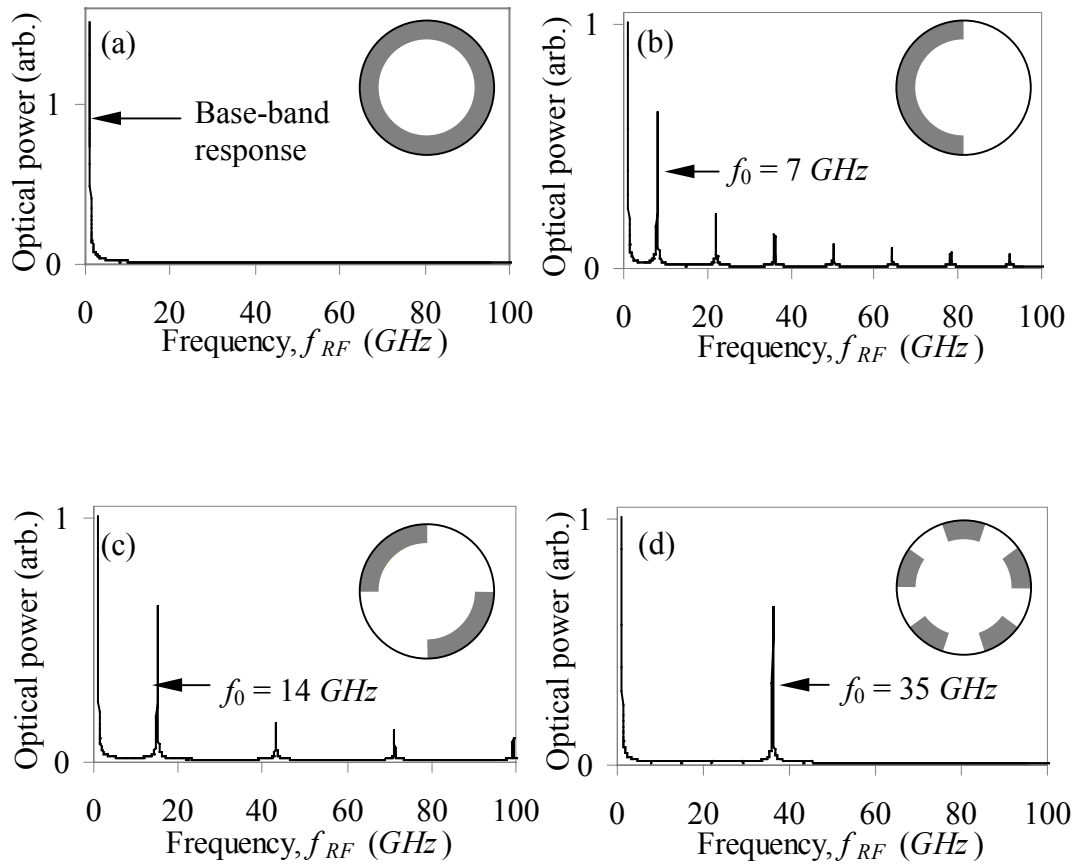


Figure 41. Calculated response of a microphotonic-based opto-electronic modulator with the indicated periodic metal electrode structures. (a) A $R = 3.18$ mm LiNbO₃ disk modulator with $\kappa = 0.05$ and a continuous ring electrode. (b) $\kappa = 0.05$ with a split 2-segment ring-electrode showing resonant opto-electronic response at 7 GHz. (c) $\kappa = 0.05$ with 4 segments and response at 14 GHz. (d) $\kappa = 0.05$ with 10 segments showing response at 35 GHz.

As shown in Figure 41(a) for the resonant solid-ring electrode, high optical- Q results in a summation of multiple round-trips that further suppresses modulation efficiency at finite frequency. Figure 41(b) - Figure 41(d) illustrate how a change in the metal

electrode pattern shifts the resonant response to higher frequencies with little decrease in efficiency. This demonstrates that disk size, in itself, does not limit *mm*-wave operation.

The relative response at the resonant frequency compared to base-band is 0.63 indicating the potential for efficient modulation. A larger modulation response at base-band results because a photon will encounter a larger average electric field during a single round trip. This is because the time constant determining this response is the round trip time $\tau_{disk} = 1/f_{FSR}$ of the disk.

If the applied RF frequency, f_{RF} is much less than f_{FSR} , a photon will make many round trips within one frequency cycle time $1/f_{RF}$, and thereby encounters a relatively uniform RF field. At higher frequencies, a photon will encounter a varying RF field during a single round trip, reducing the average electric field seen.

Figure 42(a) plots the optical power for the split 2 segment electrode case shown in Figure 41(b) on a logarithmic scale. RF detected power would be two times optical power on this log scale. Figure 42(b) and (c) show expanded views of the optical modulation response at base-band and fundamental disk frequency. Qualitatively, the presence of modulation dips result from spectral filtering by the optical resonance of the optical modulation side-bands.

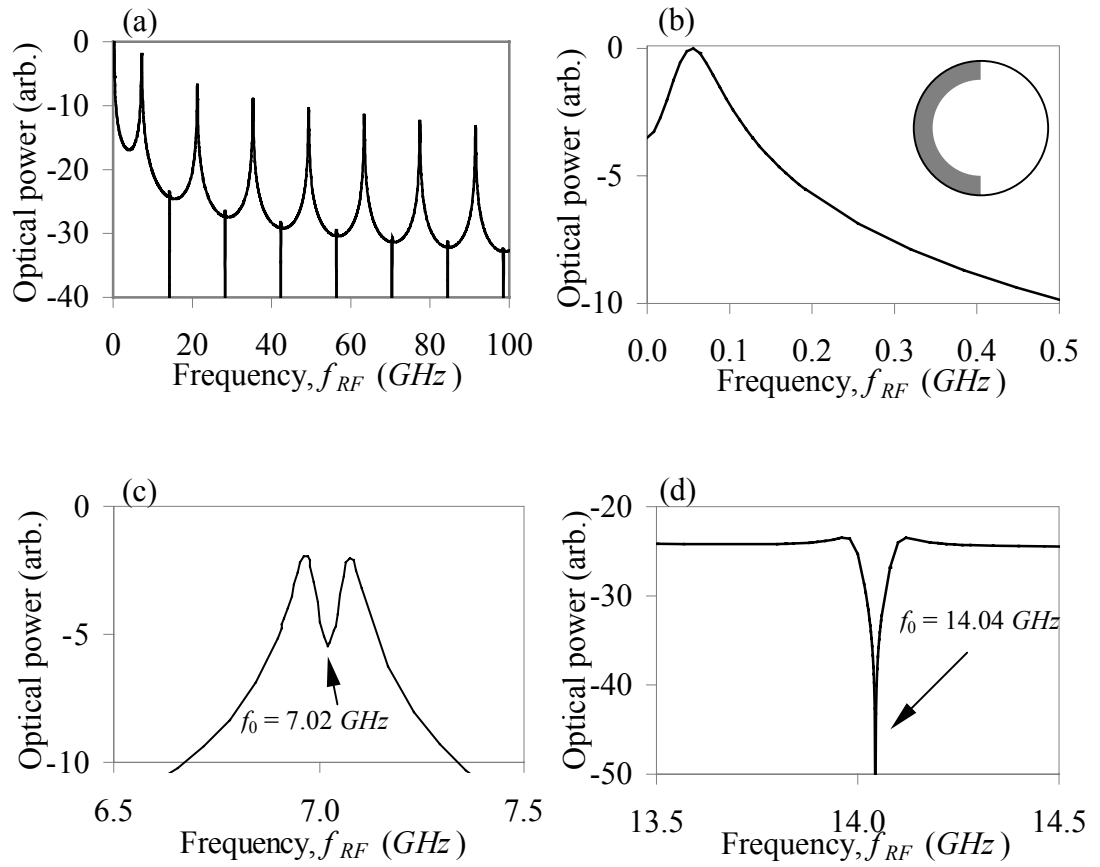


Figure 42. (a) Log scale of the $\kappa = 0.05$ with a split 2-segment ring-electrode calculated response. (b) Expanded view of the base-band response. (c) Expanded view of the fundamental 7 GHz modulation response showing a modulation dip at the center of the modulation peak. (d) Expanded view at 14 GHz showing a null in modulation at the second harmonic.

Figure 43 qualitatively explains the presence of the dips. At base-band for a fixed RF power and frequency f_{RF} , modulated optical power will be coupled out of the optical carrier frequency $f_{opt} = c/\lambda_{opt}$ and into optical side-bands $f_{opt} \pm f_{RF}$. All three optical frequencies, f_{opt} and $f_{opt} \pm f_{RF}$, must be resonant within the disk to propagate.

Figure 43(a) shows the CW optical resonance peak centered at $\lambda_{peak} = c/f_{peak}$ as a function of wavelength.

Both experiment and simulation have verified that maximum modulation occurs near the maximum slope of the CW optical resonance, labeled in Figure 43(a) as λ_{opt} . The base-band modulated response for the $\kappa = 0.05$ split 2-segment ring-electrode of Figure 42 is shown in Figure 43(b).

As f_{RF} increases, the optical side-bands are modified according to the optical resonance peak. The approximate condition for maximum modulation occurs when one optical side-band is aligned with the resonance peak ($f_{RF} = f_2$ in the figure). In the simulation, the optical input wavelength λ_{opt} was centered above the resonant wavelength such that $\Delta f = f_{peak} - f_{opt} = 50 \text{ MHz}$.

In agreement with this qualitative description, simulated maximum modulation occurs at 54 MHz . The dip at 7 GHz is understood through a similar argument, where side-bands are shifted by plus and minus one free spectral range into adjacent resonances. The peaks at 7 GHz occur $\pm 54 \text{ MHz}$ from the 7 GHz dip. Figure 42(d) demonstrates the null in modulation at when excited at the second harmonic frequency. As described in the previous section, the modulated phaseshift is canceled as the light passes between the electrode at the second harmonic.

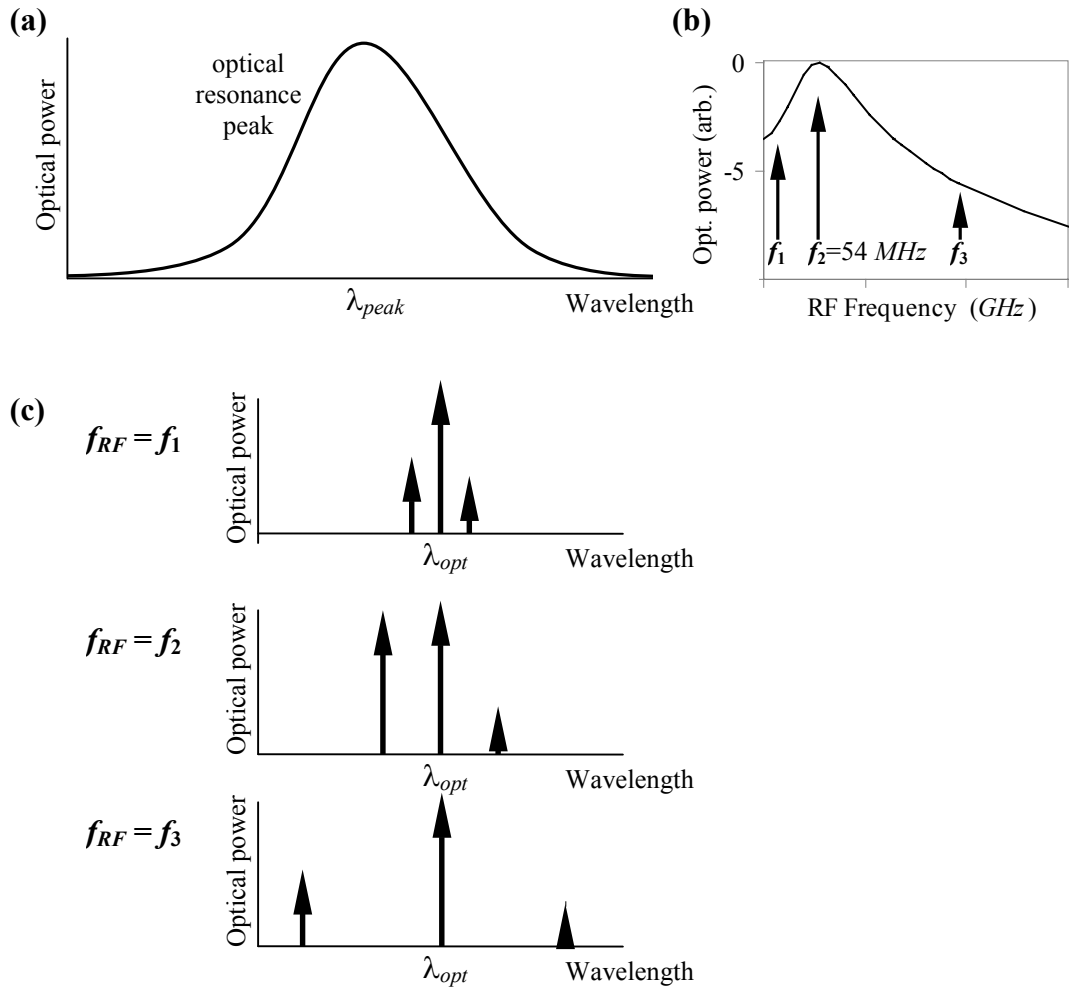


Figure 43. (a) CW optical resonance peak centered at wavelength λ_{peak} . (b) Optical modulation response as a function of applied RF frequency for the two-section electrode in Figure 42(b). (c) Optical carrier and side-band wavelengths for the three indicated RF frequencies shown in part (b). The amplitude of each wavelength is optically filtered by the resonance peak. Therefore $f_{RF} = f_2$ will have the maximum modulation as shown in (b).

Figure 44 shows the simulated response for a finite-round trip electric field loss α of the disk. A distributed value of $\alpha = 0.01 \text{ cm}^{-1}$ is typical for the experimental results presented.

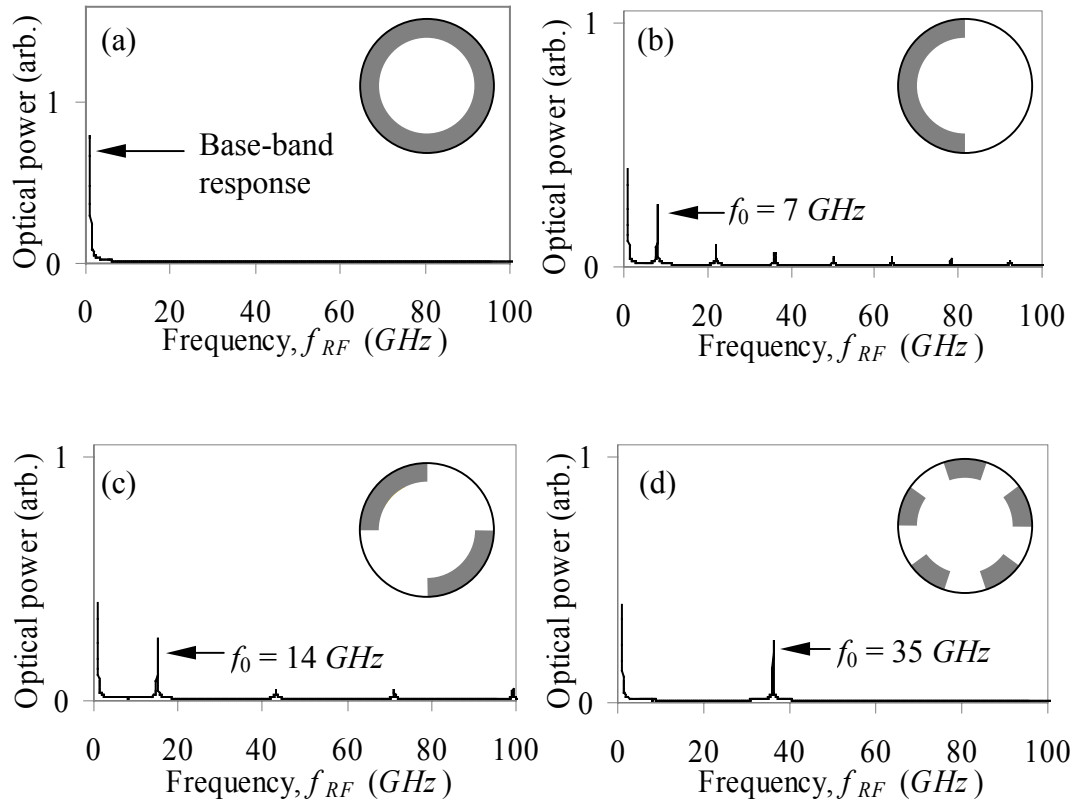


Figure 44. Calculated response of a microphotonic-based opto-electronic modulator with the indicated periodic metal electrode structures and finite scattering coefficient $\alpha = 0.01 \text{ cm}^{-1}$. (a) A $R = 3.18 \text{ mm}$ LiNbO_3 disk modulator with $\kappa = 0.05$ and a continuous ring electrode. (b) $\kappa = 0.05$ with a split 2-segment ring-electrode showing resonant opto-electronic response at 7 GHz . (c) $\kappa = 0.05$ with 4 segments and response at 14 GHz . (d) $\kappa = 0.05$ with 10 segments showing response at 35 GHz .

The modulation efficiency of the lossy resonant case at large RF frequency is found to be about 25% that of the zero-loss base-band modulation shown in Figure 41. This is a combination of the 0.63 resonant frequency to base-band efficiency, and finite α loss. A factor of two improvement in modulation efficiency is achievable by patterning electrodes in a differential (push-pull) configuration. Unpatterned regions

of the disks shown in Figure 41 could be patterned and fed by a π phase-shifted RF field. This converts the negative phase-shift incurred during the negative cycle of the RF field to a positive phase shift, thereby doubling the optical modulation efficiency.

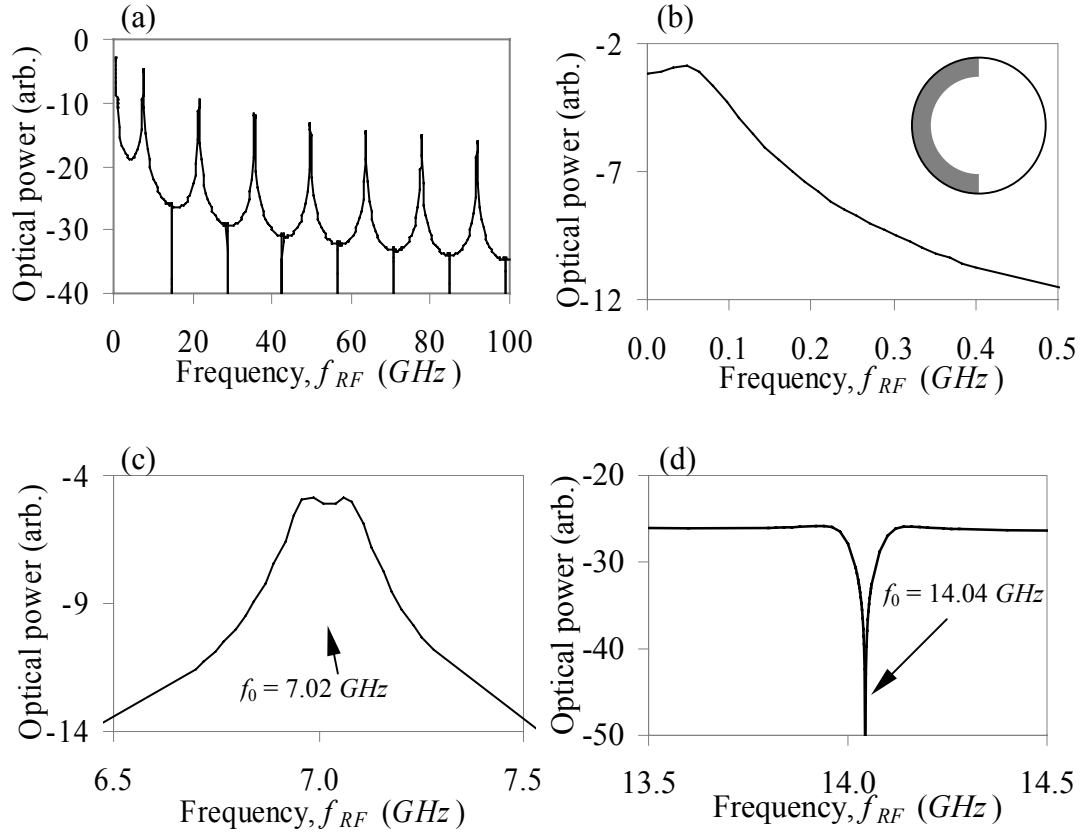


Figure 45. (a) Log scale of the $\kappa = 0.05$ and finite scattering coefficient $\alpha = 0.01 \text{ cm}^{-1}$ with a split 2-segment ring-electrode calculated response. (b) Expanded view of the base-band response. (c) Expanded view of the fundamental 7 GHz modulation response showing a modulation dip at the center of the modulation peak. (d) Expanded view at 14 GHz showing a null in modulation at the second harmonic.

Figure 45 (a) plots on a logarithmic scale the optical power for the split 2 segment electrode and finite scattering coefficient $\alpha = 0.01 \text{ cm}^{-1}$ case shown in Figure 44(b).

Similar trends in the zero scattering case are present but smoothed out due to the finite loss of the resonator.

4.6.5 Resonant periodic metal-electrode modulation simulation without a reference arm

Both experimental and simulation results have shown that the reference arm in Figure 39 is not always necessary to achieve efficient modulation. For the single coupler configuration ($\kappa_2 = 0$), Figure 46 shows as the coupling coefficient decreases, a point is passed where the Mach-Zehnder geometry is no longer needed.

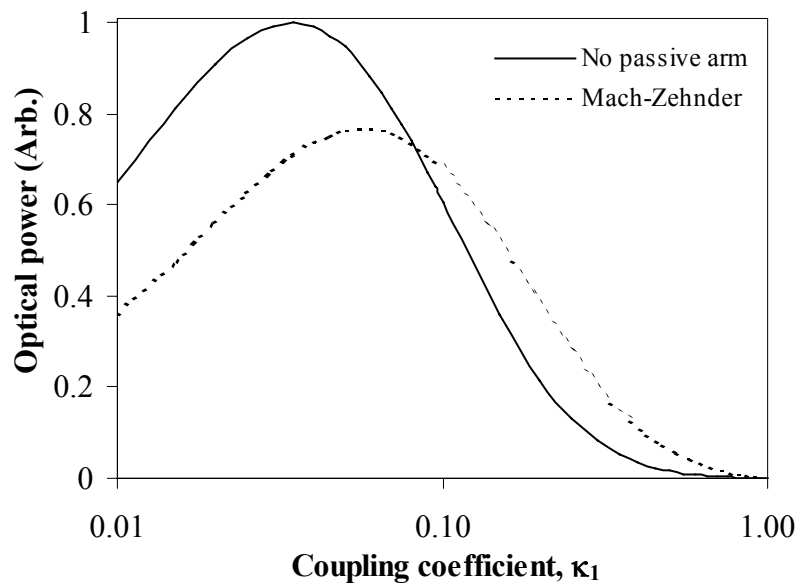


Figure 46. Simulated comparison of modulation both with and without the use of a Mach-Zehnder geometry using the single coupler geometry. Amplitude modulation without the Mach-Zehnder is shown to result in larger modulation at coupling coefficients $\kappa_1 < 0.085$. Values used in the simulation are the same as those in Figure 41(b).

Amplitude modulation is achieved through a combination of two different mechanisms. (1) Phase shifted light exiting the active arm of the Mach-Zehnder interferes with light in the passive arm, thereby converting phase information to amplitude modulation. (2) Because light of increasing round trip number has a larger accumulated phase shift, amplitude modulation will result from the interfering of these individual round trips. Because each round trip optical path length is an integral multiple of the optical wavelength, this “self-modulation” is inherently phase matched.

Figure 46 shows a comparison of modulation with and without the Mach-Zehnder geometry. In the single pass limiting case $\kappa_1 = 1$ and $\kappa_2 = 0$, light passing along the active arm is phase modulated. It is then amplitude modulated through interference with the passive arm. Because there is only one round trip, there is no self-modulation. As κ_1 decreases from 1, self-modulation becomes a larger fraction of the total modulation. Below a value of $\kappa_1 = 0.85$ in the simulation, the Mach-Zehnder geometry becomes a disadvantage, and a modulation geometry without the passive arm becomes more efficient. A smaller value of κ_1 means that more light is being coupled into the disk. Therefore, the inefficiency of the Mach-Zehnder geometry results because half of the optical power is split into the passive arm, and cannot partake in the more efficient self-modulation mechanism.

Comparison of experiment and simulation shows the typical coupling coefficients are $\kappa_1 < 0.05$, and therefore using a single-arm non-Mach-Zehnder configuration will result in more efficient modulation geometry.

4.7 Direct-contact (“T - electrode”) modulation

To confirm our simulations, a microstrip electrode is placed on top of the LiNbO₃ disk and directly excited with a RF field using a SMA microstrip launcher as shown in Figure 47. The electrode geometry in Figure 48(a) was used to understand propagation of the RF field along the electrode. The “T-electrode” was composed of a 50 Ω microstrip line that terminates at a microstrip resonator of length L . Simulations demonstrate that most of the RF power launched into the microstrip reflects at the end of the line. However, some of the energy is coupled into a standing wave along the length of the microstrip resonator. The frequency of the standing wave is $f_{RF} = c/(2n_{eff}L)$, where n_{eff} is the effect index of refraction seen by the RF resonant mode. Figure 48(b) shows the RF electric field magnitude at the sensor location shown in Figure 48(a). Efficient coupling of electric fields at DC, base-band, and the resonator fundamental frequency are all coupled to the RF resonator. In the geometry shown, loading of the resonator by the microstrip feed does not permit second or higher harmonics to couple onto the resonator. By shifting the launch position along the length of the resonator, coupling of higher harmonics was achievable. This “current resonator” geometry is similar to a shunt (parallel)

LRC circuit, where there is current gain, but no voltage gain. This geometry thereby allows investigation into modulator efficiency independent of any effect due to voltage gain that we will see later in this chapter. A final advantage is that this design will scale to mm-wave frequencies.

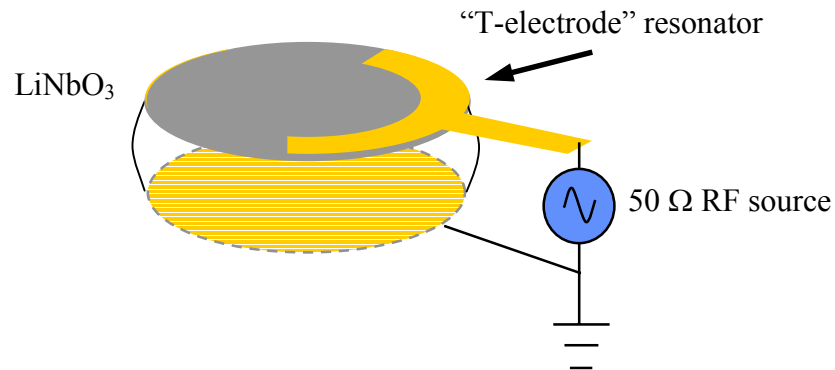


Figure 47. Direct-contact electrode geometry used to excite a “T-electrode” resonator. This RF resonator is used to couple RF power onto the LiNbO₃ disk to achieve out-of-base-band modulation.

4.7.1 Experimental results of RF modulation

Experimental results are presented using the “T - electrode” geometry as shown in the inset of Figure 49. Light of wavelength $1.55 \mu\text{m}$ is coupled into a $2R = 5.8 \text{ mm}$ diameter LiNbO₃ disk with a resulting FSR of 7.6 GHz . Using a network analyzer, the fundamental resonant RF frequency of the microstrip electrode is tuned to match the FSR of 7.6 GHz by monitoring the dip in the reflected RF excitation response, S_{11} , as shown in Figure 49(a). Figure 49(b) and Figure 49(c) demonstrate the detected modulated optical power from the LiNbO₃ microphotonic modulator. We

see that the 7.6 GHz optical modulation is 60% that of base-band modulation as expected by simulation discussed Section 4.6.4. In addition, the RF bandwidth of 150 MHz matches closely with the measured optical Q of 1.3×10^6 .

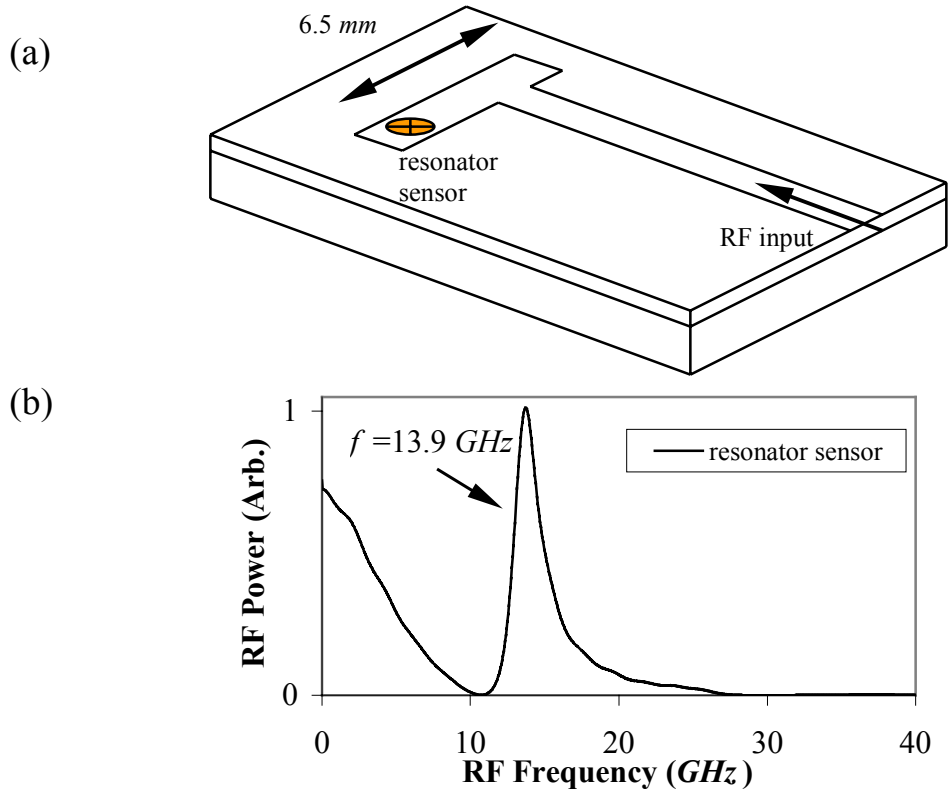


Figure 48. “T-electrode” (a) Simulation geometry, with microstrip width = 1.5 mm, substrate thickness = 0.5 mm, and relative dielectric constant, $\epsilon_r = 2.94$. (b) Simulated RF power at the resonator sensor in (a).

Modulation side-band suppression is directly related to the unmodulated optical spectrum of the disk, although in a complex manner. Figure 50(a) shows an optical spectrum with two small side modes spaced about 150 MHz from the center mode.

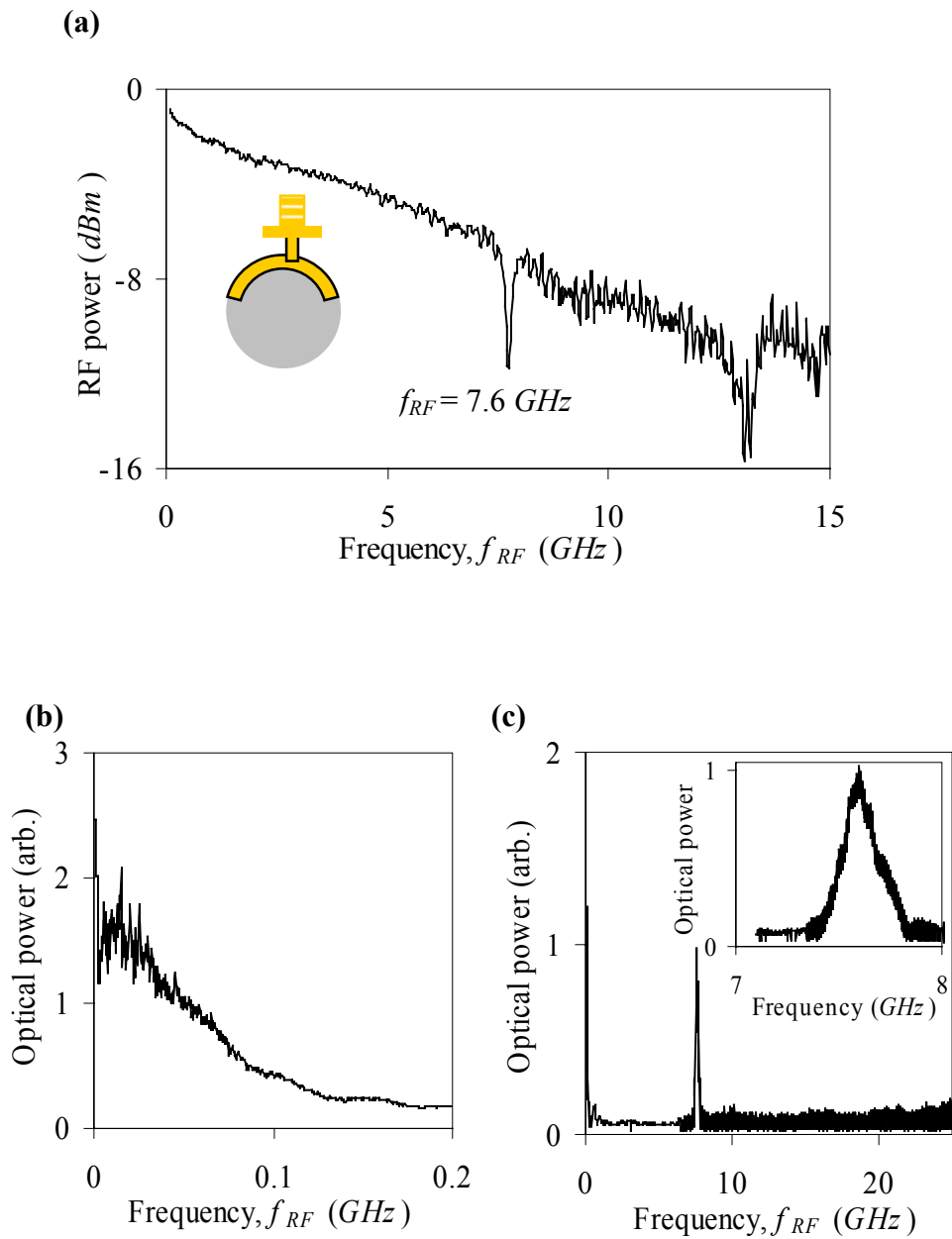


Figure 49. Measured results showing optical modulation of a 5.8 mm diameter, 0.74 mm thick LiNbO₃ microphotonic modulator at 7 GHz. (a) The reflected swept RF excitation response, S_{11} , of the resonant electrode (“T electrode”) structure show in the inset. (b) Detected optical response at base-band frequencies versus a swept RF input. (c) Detected optical response versus a swept RF input. The resulting modulation peak is at 7.6 GHz with a measured bandwidth of 150 MHz.

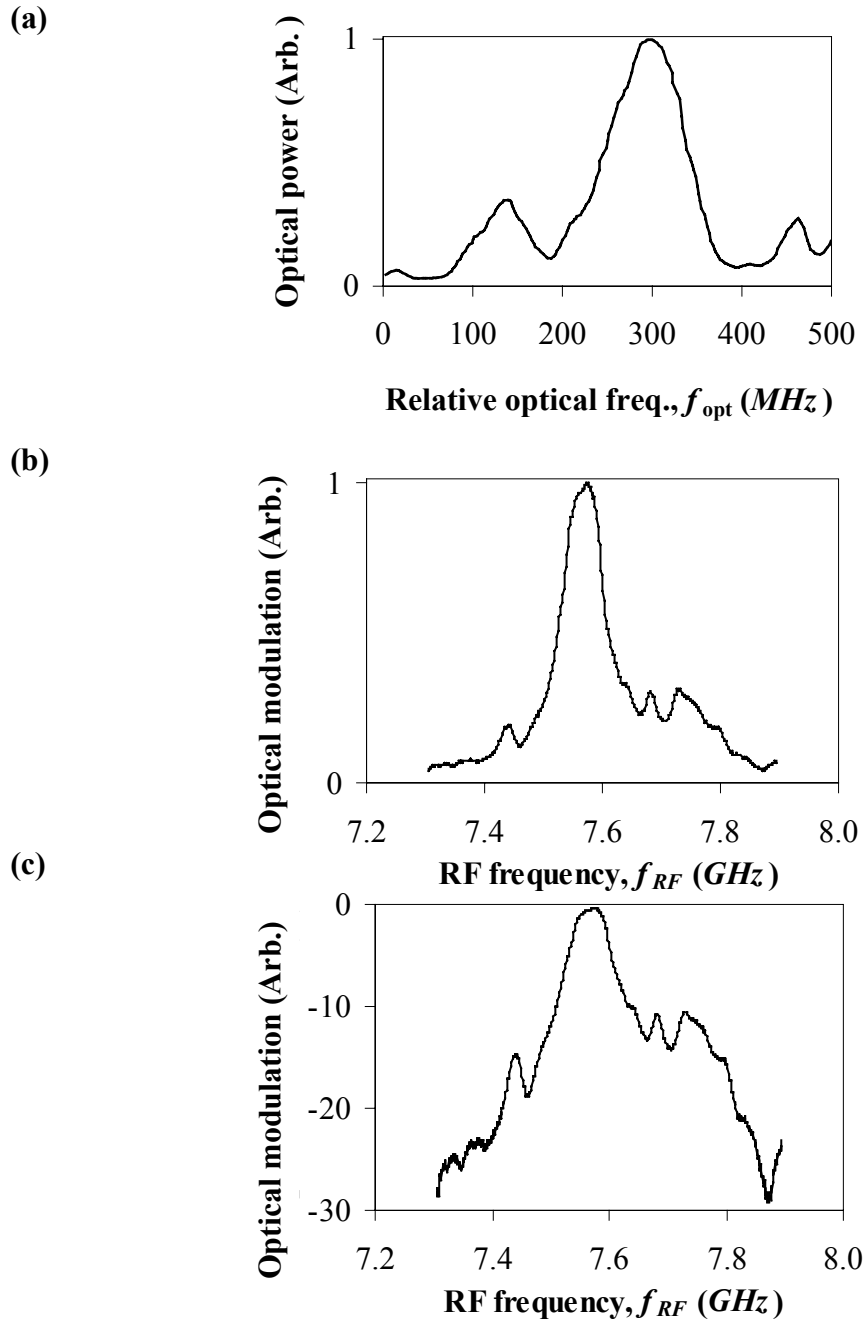


Figure 50. (a) Optical spectrum showing the *WGM* used for modulation and two smaller optical side-modes. (b) Detected optical modulation response on a linear scale. Existence of the optical side-modes in (a) are the cause of the modulation side-bands shown. (c) Same as (b) using a logarithmic scale.

Figure 50(b) and Figure 50(c) shows the linear and logarithmic optical modulation response using a center wavelength of about $1.55 \mu m$ which is centered at $250 MHz$ with respect to Figure 50(a). Energy coupled into these optical side modes, will generate modulation side-bands with frequency spacing similar to that in the optical domain, as we see in Figure 50(b) and Figure 50(c). The cleaner the optical spectrum, the larger the modulation side-band suppression.

The actual relation between the optical spectrum and the modulation RF spectrum is complex. The modulation mechanism requires that three wavelengths (one carrier and the two side-bands) be simultaneously in resonance. When the spacing of the optical side-bands are not equal to the fundamental FSR (as is the case with the modulation side-bands), the optical side-bands will couple to different modes with different slopes. Therefore, the final shape of the optical modulation response will not directly map with the optical spectrum.

4.7.2 Experimental results of *mm*-wave modulation

As indicated through simulation, modulation can be achieved at an integral number times the optical FSR of the disk by changing the period of the metal electrodes. This is demonstrated through experiment where we achieve *mm*-wave modulation in the Ka band as shown in Figure 52(a). By modifying the periodicity of the metal electrodes on a $LiNbO_3$ microphotonic modulator, *mm*-wave modulation at a

frequency of 30.25 GHz is obtained using the electrode shown in Figure 51. This electrode was tuned to the second harmonic of the optical resonator at approximately 15.15 GHz . By tuning the optical wavelength to the maximum of the optical resonance peak, modulation frequency doubling was achieved (see Section 4.8.1). The resulting modulation frequency is approximately four times the optical FSR of 7.6 GHz as expected. Figure 52(a) shows both RF and optical electrical fields simultaneously tuned on resonance.

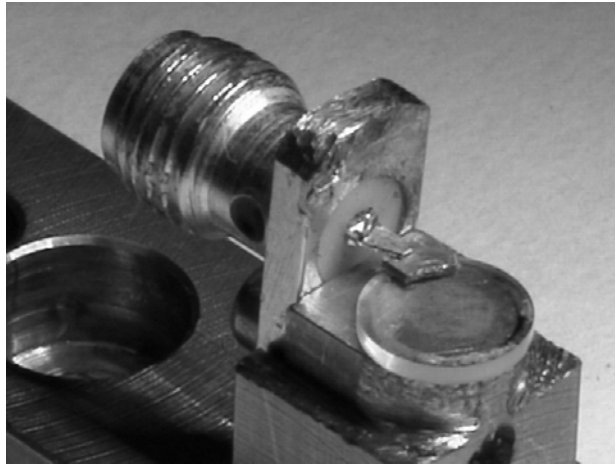


Figure 51. Electrode structure used to achieve optical modulation at 30.25 GHz . The SMA launch was tapered to reduce loading on the relatively small electrode.

To confirm that modulation is a result of simultaneous resonance of RF and optical electric fields within the disk, we individually detune the applied RF frequency, and optical wavelength from that of resonance. In Figure 52(b) we keep the RF on resonance, while tuning the optical wavelength off resonance, showing that there is

only residual modulation at less than -40 dB as compared with the simultaneously on resonance modulation. This is a result of optical excitation of low- Q higher-order modes while tuned off-resonance. Figure 52(c) shows complete loss of modulation as the RF electric field is detuned from resonance.

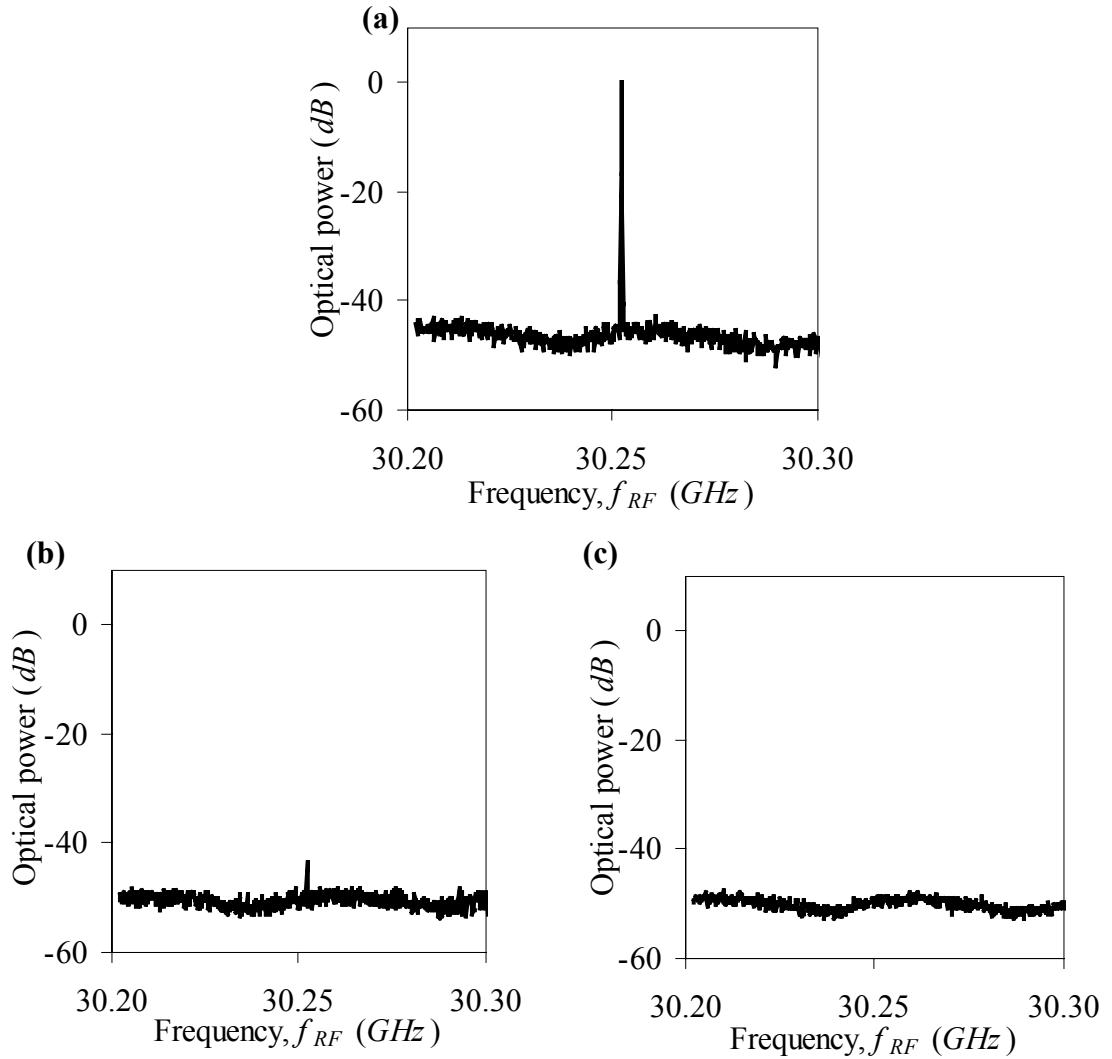


Figure 52. (a) Measured results showing optical modulation of a 5.8 mm diameter, 0.74 mm thick LiNbO₃ microphotonic modulator at 30.25 GHz for a CW RF input. (b) Detected optical response when the optical wavelength is tuned off the optical resonance. (c) Detected optical response when the applied RF field is tuned off the RF resonant frequency.

4.8 Side-coupled-electrode modulation

An electrode geometry using side coupling of microstrip lines is suggested by capacitively coupled stripline resonators. A large class of filters known as coupled-line filters are manufactured using side-coupling as a means to transfer RF power from one microstrip to another [80]. Figure 53 shows just such a filter in a bandpass geometry. Here, a microstrip of impedance Z_0 evanescently side couples energy over a coupling length x to a microstrip resonator of length L . This resonator will have a resonant fundamental frequency at $f = c/2nL$, where L is the length of the resonator. In addition, voltage amplification occurs as a result of evanescent coupling of the fringing fields of the microstrip line. This passband filter will then couple energy only at the resonant frequency f to the output microstrip line.

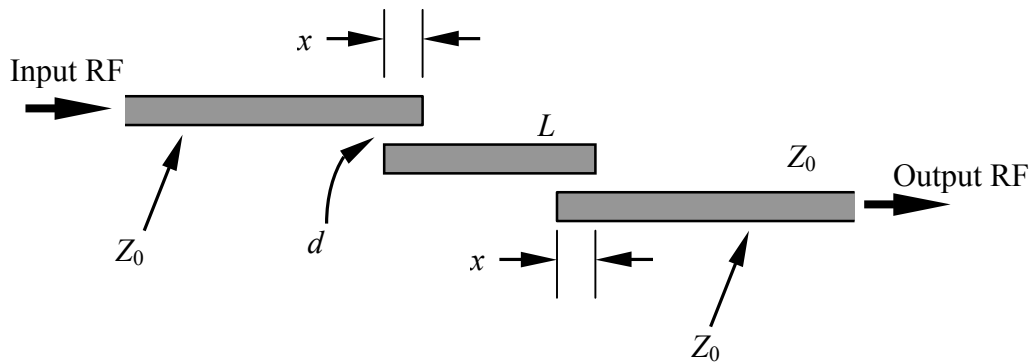


Figure 53. Coupled-line filter in a band pass filter geometry. .

Although evidence of field amplification within the resonator of a coupled-line filter was not found in the literature, basic electromagnetic waveguide arguments [80],

comparison to LRC circuits (see Section 2.5.1), and RF simulation using GENESISe [81] confirm that the resonator will have voltage amplification at the resonant frequency with an associated quality factor, Q .

A related side-coupling RF-coupling scheme is used to excite a RF microstripline resonator to achieve both voltage amplification and efficient RF coupling to the microphotonic resonator. Figure 54(a) shows the geometry of the side-coupled electrode. A SMA launch is used to couple power from the RF source to the $50\ \Omega$ microstrip line patterned on a RT-Duroid 6002 substrate with $\epsilon_r = 2.94$ at $20\ \text{GHz}$, propagation losses of $2.89\ \text{dB/m}$ at $6.67\ \text{GHz}$, and a loss tangent of 0.00119 . [82]. The RF power reflects from the open end of the microstrip line generating the standing wave pattern seen in Figure 54(b). However, part of the RF power evanescently couples to a microstrip resonator of length L that is either patterned or placed on the LiNbO_3 disk. This coupled power generates standing waves at RF frequencies $f_{RF} = mc/(2n_{eff}L)$, where n_{eff} is the effective RF index of refraction seen by the RF mode, and m is an integer. Figure 54(b) shows RF intensity of a simulated resonant standing wave at $9.3\ \text{GHz}$.

Radiation losses from this type of structure cannot be ignored. For an open-end microstrip discontinuity of width w and height h , losses at frequencies below approximately $10\ \text{GHz}$ are dominated by radiation losses that increase as ω^2 [84]. At

frequencies above 10 GHz, losses through surface wave propagation on the dielectric material at the end of the discontinuity become significant, and are shown to be of the same order as radiation loss [85]. The first approach to reduce radiation is metallic shielding. Simulations have shown consistent improvement in the Q , of microstrip resonators in the presence of a metallic shield. In the case of a capacitive coupled microstrip resonator [80], simulations using HFSS showed that the RF Q improved by a factor of 2, and throughput by 6.4 dB. Surface wave propagation tends to be reinforced by shielding, and suggestions to reduce these waves include introduction of lossy material near the discontinuity (while trying to avoid reducing the resonator Q), and cutting slots in the dielectric to repress propagation of the radiative modes. In addition, total losses $\sim 1/\epsilon_r$, and therefore a larger dielectric material will reduce such losses [80].

4.8.1 Experimental results of RF modulation

Figure 55, and the inset to Figure 56 show the RF and optical experimental configuration. Prisms are used to couple laser light of approximate wavelength $\lambda = 1.55 \mu\text{m}$ into and out of the WGM optical mode of the microphotonic resonator. The optical wavelength is tuned to a resonant wavelength of the optical resonator. A RF electric field propagating on a 50 Ω metal microstrip line evanescently side-couples to a metal electrode resonator on the LiNbO₃ disk. The fundamental resonant

frequency of the electrode resonator is tuned to match the optical FSR of 7.56 GHz as indicated by the dip in the reflected RF excitation response shown in Figure 56.

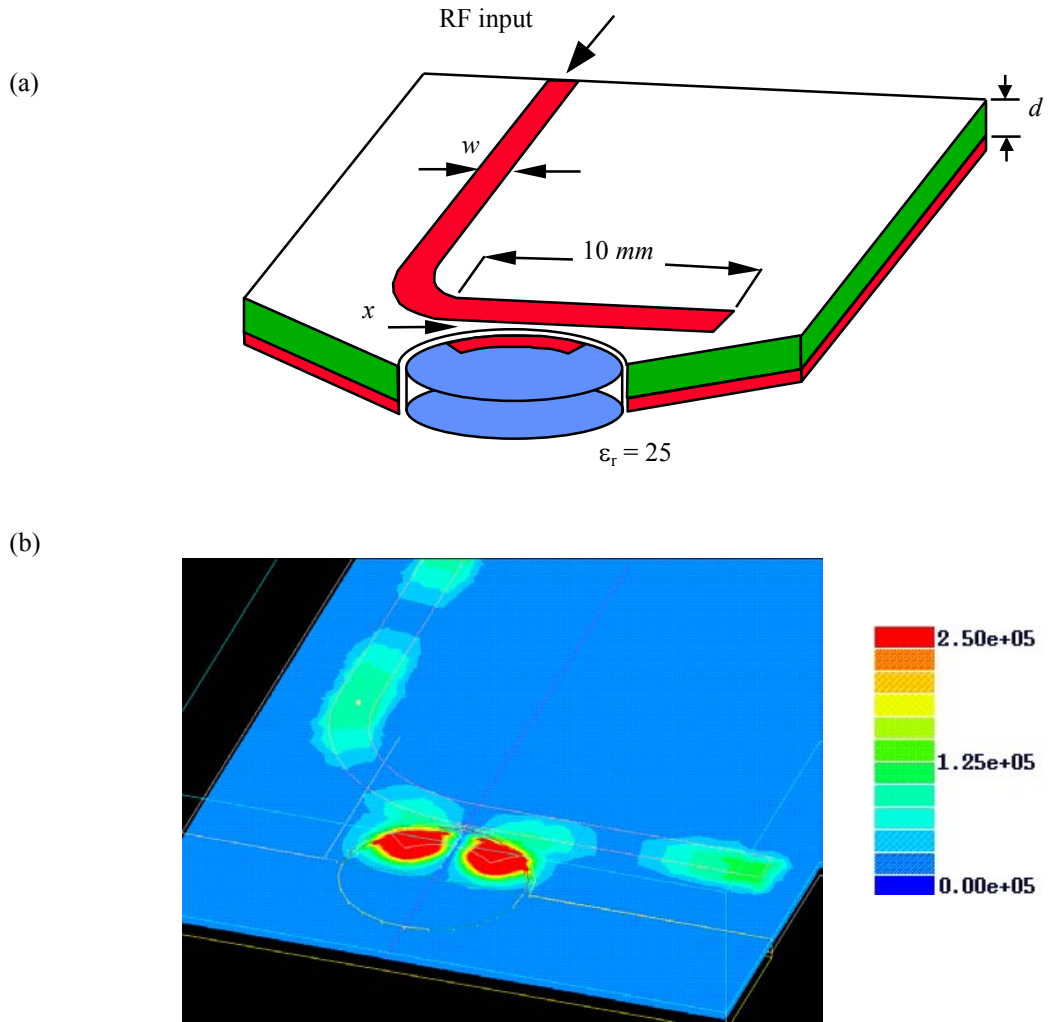


Figure 54. (a) Side-coupled resonator geometry used to achieve simultaneous resonance with RF voltage gain. (b) Simulation results showing the RF intensity at the fundamental frequency of the RF resonator. The simulation assumed a dielectric thickness, $d = 0.508 \text{ mm}$, relative dielectric constant, $\epsilon_r = 2.94$, line width, $w = 1.2 \text{ mm}$, disk thickness, $t = 0.7 \text{ mm}$, resonator width = 1.2 mm , resonator angle = 90 degree, and gap spacing, $x = 0.3 \text{ mm}$. Scale is in arbitrary linear units. The simulation was generated using Ansoft HFSS [83].

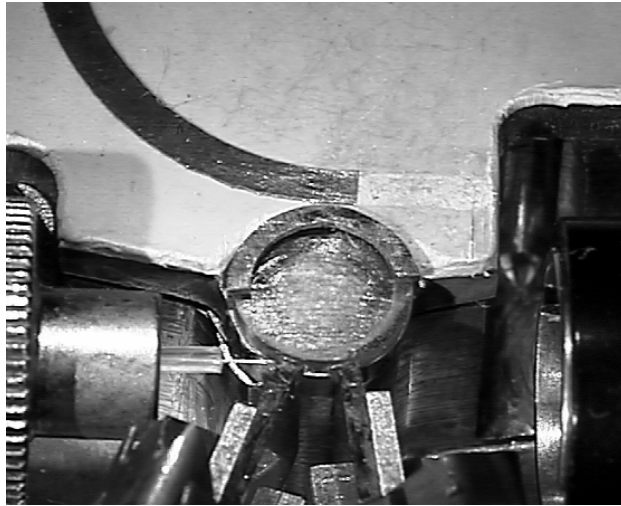


Figure 55. Photograph showing the experimental setup used for the side-coupled electrode coupling scheme.

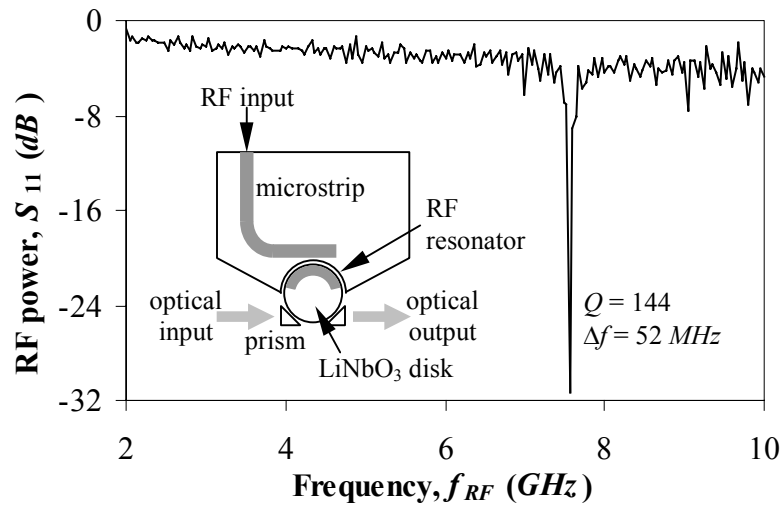


Figure 56. Measured reflected RF power S_{11} demonstrating maximum coupling of energy to the microstrip resonator at 7.56 GHz. An absorption $Q = 144$ is measured. The geometry of the side-coupled microstrip resonator approach is shown in the inset.

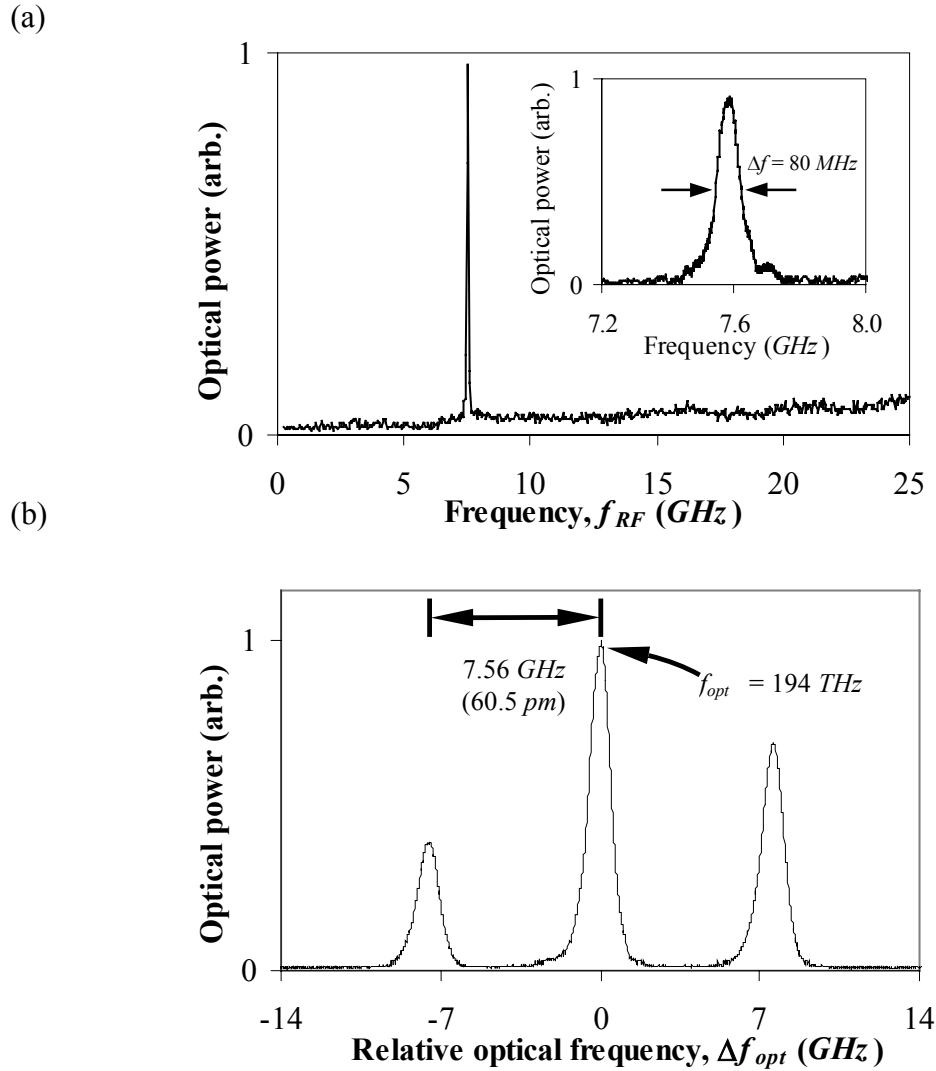


Figure 57. (a) Detected output optical power versus input RF frequency for a $R = 2.92$ mm LiNbO₃ disk modulator. The light exiting the disk is optically modulated at 7.56 GHz, with a bandwidth of 80 MHz. (b) Detected output optical power as a function of optical frequency is shown. Both the optical carrier at 194 THz (1.55 μm) and 7.56 GHz optical side-bands are shown. The measured optical line width is limited by the Fabry-Perot filter resolution which is $f_{3dB} = 900$ MHz.

Figure 57(a) shows the detected optical signal as a function of the applied RF frequency, f_{RF} . The resulting optical modulation is centered at 7.56 GHz with a -3 dB bandwidth $\Delta f = 80$ MHz. The measured voltage gain provided by this resonator is

greater than 4. Improved resonator designs should be capable of achieving voltage gains in excess of 100. This can be realized through reduction of radiation losses and an understanding of the relation of Q and voltage amplification in the case of the curved resonator.

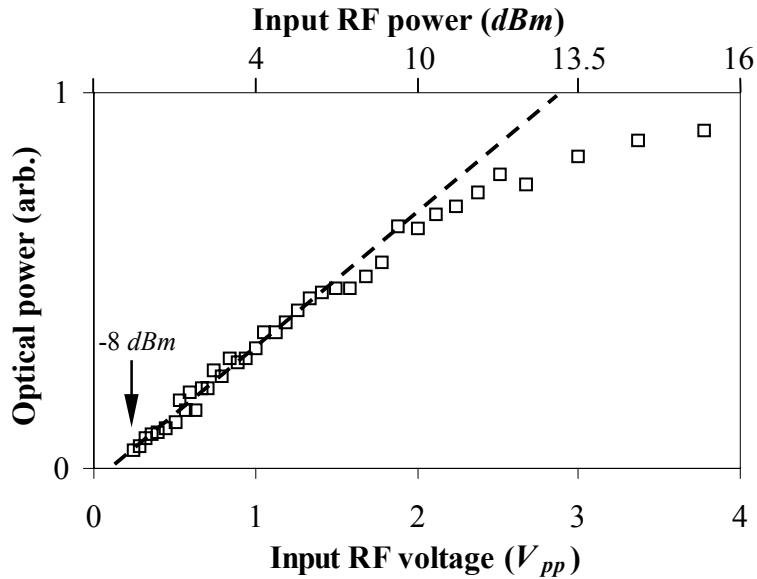


Figure 58. Detected optical modulation as a function of RF power launched onto the RF microstrip resonator. Optical power of 1.0 corresponds to the measured optical power at the maximum of the optical resonance with no modulation. This demonstrates that near 100% modulation is achievable at voltages comparable to conventional LiNbO₃ Mach-Zehnder interferometers.

RF modulation of the optical carrier was directly observed by passing light exiting the microphotonic resonator through a Fabry-Perot interferometer with an optical resolution of $f_{3dB} = 900 \text{ MHz}$. As indicated in Figure 57(b), the optical carrier at 194 THz ($\lambda = 1.55 \text{ }\mu\text{m}$) is centered between two optical side-bands, each separated by 7.56 GHz ($\Delta\lambda = 60.5 \text{ pm}$) from the optical carrier. Input light has an optical

bandwidth of less than 0.5 MHz. The measured optical line width is limited by the Fabry-Perot filter resolution which is $f_{-3dB} = 900$ MHz.

Figure 58 shows the modulated optical power at 7.6 GHz for a fixed optical wavelength, where 1.0 equals 100 % optical modulation. Small signal modulation shows a linear increase with input RF voltage. At larger voltages, nearly 100 % modulation is achieved. These voltages are similar to values of V_π found in commercial LiNbO₃ Mach Zehnder modulators.

Modulation saturation is expected because the basis of optical modulation is phase modulation. As in a conventional Mach Zehnder modulator, beyond a 2π phase shift one is driving the modulator strongly into the non-linear domain, and power in the fundamental mode is transformed to the higher. This is shown by simulation in Figure 59. Modulation response is related to the slope of the optical resonance. The inset shows less efficient modulation at the fundamental RF frequency can occur at extremely large RF fields. This second less efficient peak occurs when the large RF field drives the modulator so hard that the slope of an adjacent resonance is sampled.

Minimum sensitivity in our initial experiments was found to be 250 mV_{pp} or 160 μW electrical. The dynamic range, DR of the modulator can be estimated from this using

$$DR (dB) = P_{-1dB} (dB) - NF (dB)$$

where P_{-1dB} is the 1 dB compression point and NF is the noise floor [86]. The noise floor is measured to be $160 \mu W = -7.96 dBm$, and the 1 dB compression point is 2.7 V, or 12.6 dBm. Therefore the experimentally measured electrical dynamic range is 20.6 dB. Use of narrow band RF filters to remove the broadband noise of the optical detector should increase the dynamic range beyond the experimental result shown here.

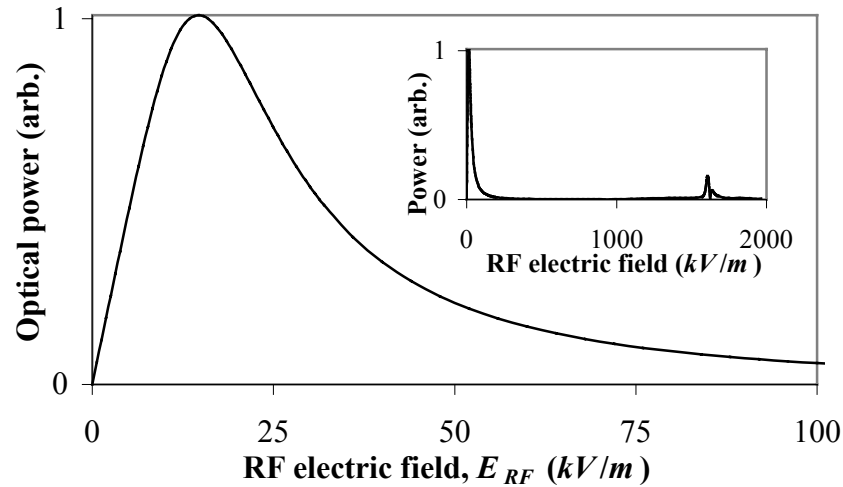


Figure 59. Graph showing modulation at the fundamental frequency as a function of applied electric field. Large applied electric fields drive modulation outside of the linear response region and couple energy into higher harmonic frequencies. The inset shows that at extremely large RF fields, a smaller peak in modulation at the fundamental occurs.

A dramatic increase in RF sensitivity may be achieved by placing the metal electrodes closer to the optical WGM, improving spatial overlap of the RF field with the optical mode, and increasing the Q of the RF resonator.

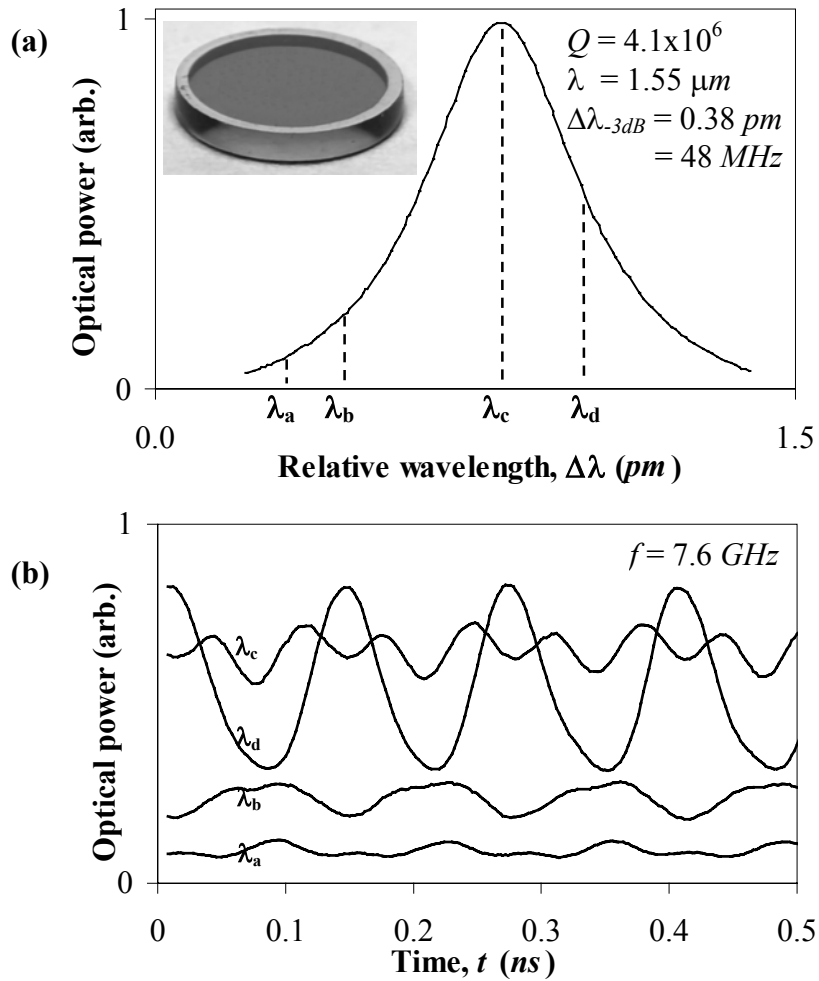


Figure 60. (a) Measured optical resonance of the LiNbO₃ disk near wavelength $\lambda = 1.55 \mu\text{m}$. The measured Q of this device is more than 4×10^6 . Inset shows a photograph of a z-cut LiNbO₃ disk-shaped resonator with optically polished curved side-walls. Gold electrodes are placed in an annulus around the disk to increase the overlap of electrical bias and optical fields. The dimensions of the disk are radius $R = 2.92 \text{ mm}$ and thickness $d = 0.74 \text{ mm}$. (b) Detected optical time-domain signal showing 7.56 GHz modulation. Modulation is shown at four wavelengths referenced in (a), and is maximum at a wavelength corresponding to the maximum slope of the optical resonance.

Figure 60(a) shows the measured optical spectrum of the WGM resonance in the absence of RF modulation, with a resulting optical $Q = 4 \times 10^6$. As shown in Figure

60(b), optical modulation is maximized for a fixed RF input power when the optical wavelength λ_d is located at the maximum slope of the WGM spectral shape. Frequency doubling is shown to occur at the wavelength λ_c at the center of the optical resonance. In addition, because the slopes are opposite on either side of the optical resonance, the modulation response at λ_c and λ_d are π out of phase.

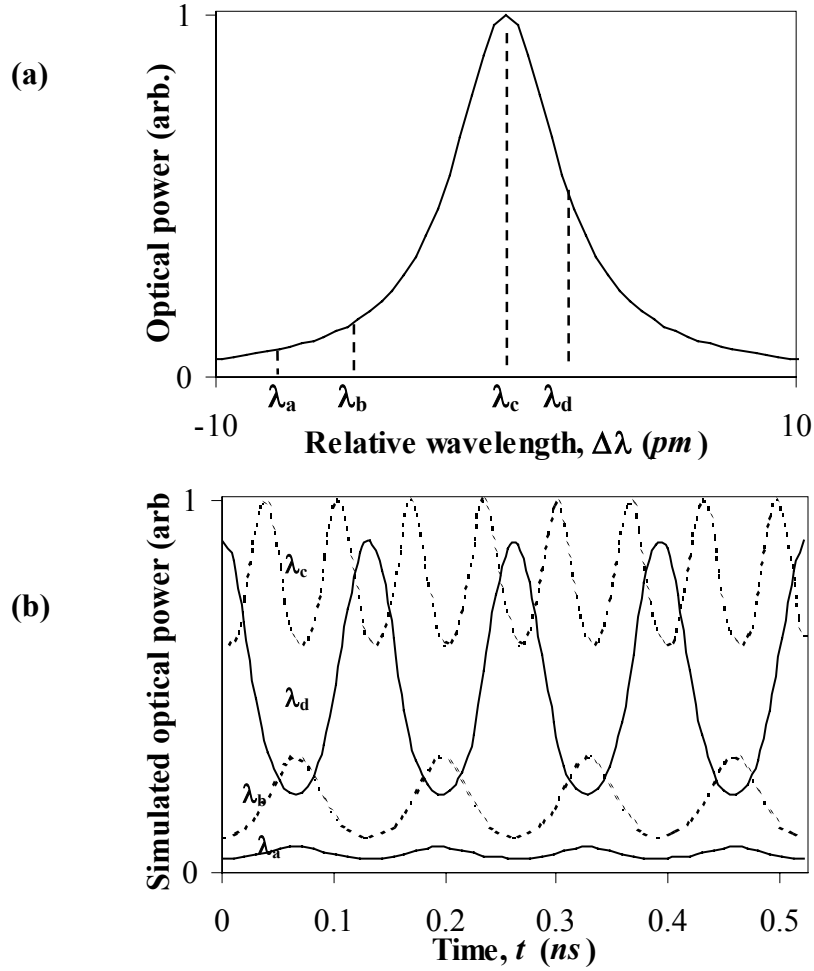


Figure 61. (a) Simulated optical resonance of the LiNbO₃ disk near wavelength $\lambda = 1.55 \mu\text{m}$. The radius of the simulated disk is $R = 2.92 \text{ mm}$. (b) Simulated optical time-domain signals showing 7.6 GHz modulation. Modulation is shown at four wavelengths referenced in (a), and is maximum at a wavelength corresponding to the maximum slope of the optical resonance.

As additional confirmation of the microphotonic resonator modulation model, time domain simulation was compared to the experimental data shown in Figure 60. Figure 61 shows very good agreement with the experimental data including frequency doubling, the π phase change, and maximum modulation occurring near the maximum slope of the optical resonance.

4.8.2 Experimental results of *mm*-wave modulation

Figure 62 shows *mm*-wave RF coupling on a side-coupled microstrip resonator. 30.3 GHz modulation is achieved by using the third harmonic of the RF resonator.

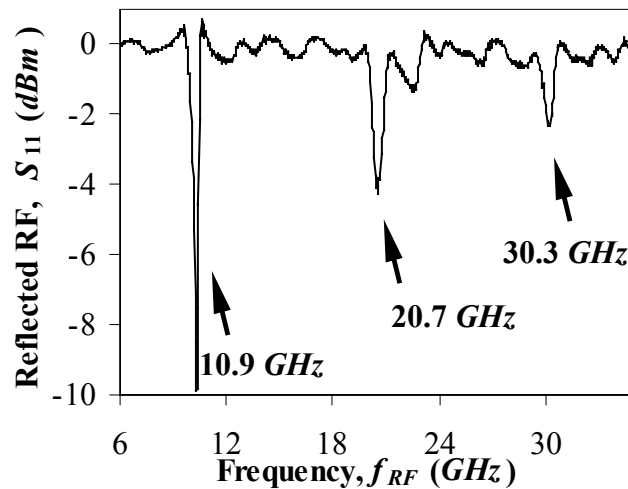


Figure 62. Reflected RF power S_{11} from a side coupled microstrip resonator showing *mm*-wave RF coupling at 30.3 GHz.

Optical modulation is also demonstrated at *mm*-wave frequencies in the Ka band as shown in Figure 63(a). Figure 63(b) shows only residual modulation when the

optical wavelength is tuned off resonance, while the RF frequency is still set to resonance. Figure 63(c) shows the optical wavelength on resonance, with the RF frequency tuned off resonance.

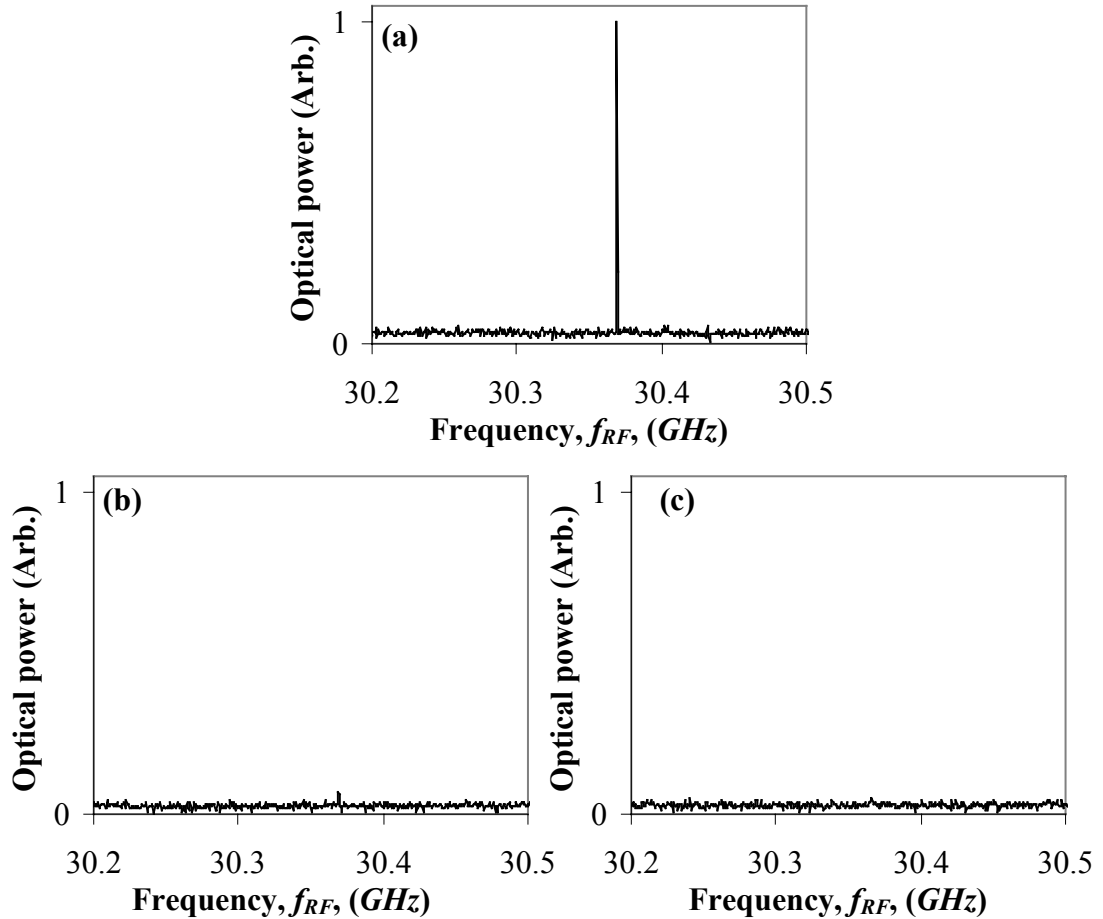


Figure 63. (a) Demonstration of mm-wave modulation at 30.37 GHz with both the RF frequency, and optical wavelength tuned into resonance. (b) When the optical wavelength is tuned off resonance, while the RF frequency stays in resonance, we see no modulation. (c) In addition, no modulation results if the optical wavelength is kept tuned on resonance, while the RF frequency is tuned off resonance.

Efficient modulation at *mm*-wave frequencies is achievable if work is undertaken to improve RF coupling to the disk. It was observed experimentally that large

modulation efficiency become challenging above 20 GHz. At these frequencies, features of a few millimeters in size become stray resonators in the system. In addition, the material properties of RF cables, SMA launchers, and microstrip lines can become lossy. Though better RF design, a significantly similar coupling scheme to that used should permit efficient operation to 40 GHz. To support this statement, modulation at 37.9 GHz has been demonstrated as shown in Figure 64. This modulation used the third harmonic of a 12.3 GHz microstrip resonator.

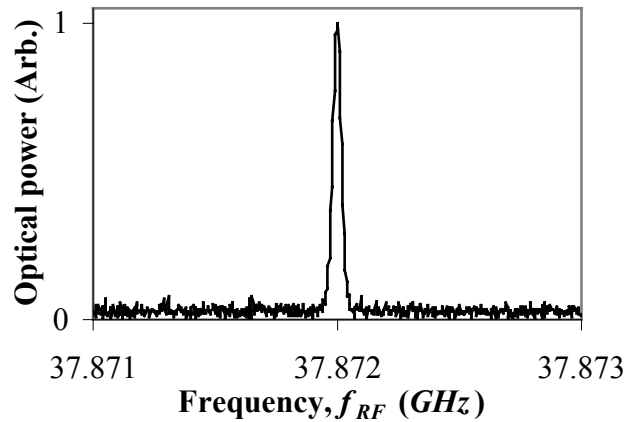


Figure 64. Modulation of the LiNbO₃ resonator at 37.9 GHz. This was achieved using the third harmonic of a 12.6 GHz microstrip resonator.

4.9 Measured linearity of LiNbO₃ optical microresonator

Frequency doubling is an inherent modulation response to the non-linearity of the microphotonic modulator. To understand the impact on measured linearity, a single tone RF frequency was launched onto the disk using the direct electrode approach. Figure 65(a) shows the maximum modulation response for a single tone RF input

($f_{RF} = 7.6 \text{ GHz}$) where the optical wavelength was tuned near the maximum slope of the optical resonance.

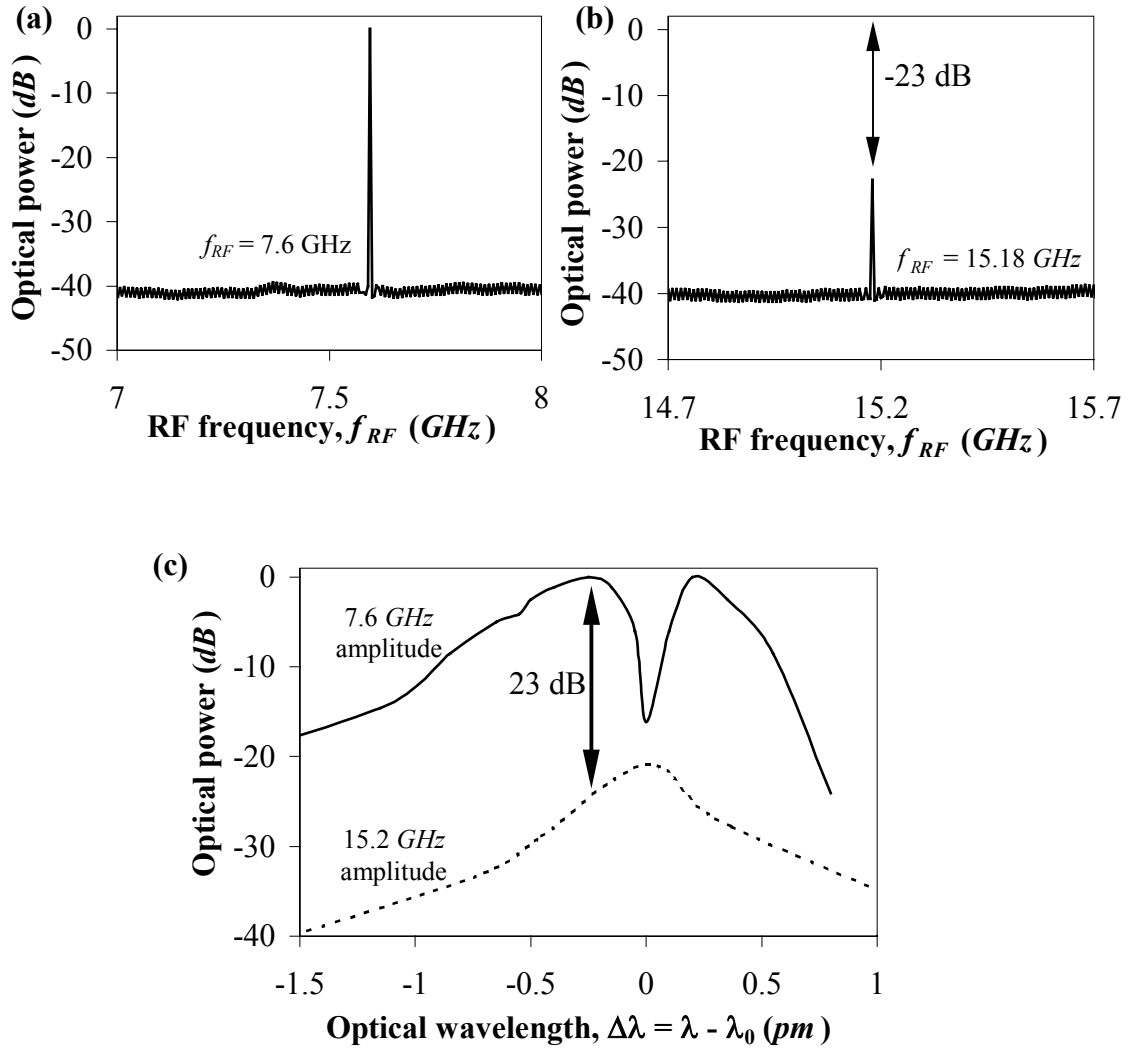


Figure 65. (a) Maximum modulation response of the microphotonic resonator when excited by the fundamental frequency $f_{RF} = 7.6 \text{ GHz}$. The optical wavelength is tuned near the maximum slope of the optical resonance. (b) Frequency doubled modulation response at the second harmonic $2f_{RF} = 15.2 \text{ GHz}$ when excited by the same RF power as (a) at a frequency $f_{RF} = 7.6 \text{ GHz}$. (c) Fundamental and second harmonic modulation response for an input frequency $f_{RF} = 7.6 \text{ GHz}$ versus optical wavelength. This shows that frequency doubling is maximum at the optical resonance peak λ_0 .

Figure 65(b) shows the maximum frequency doubled optical response at the second RF harmonic ($2f_{RF} = 15.2 \text{ GHz}$) at the same optical wavelength. The frequency-doubled response was found to be 23 dB below the maximum of the fundamental modulation amplitude. Figure 65(c) shows a plot of the fundamental and second harmonic amplitudes as a function of optical wavelength. This demonstrates that frequency doubling is maximized at the peak wavelength of the optical resonance λ_0 .

4.10 Scaling of the LiNbO₃ microresonator

Scaling of the microphotonic resonator is important in understanding the limitations of device operation. Optical polishing of the curved sidewalls is key to resonator fabrication and is the limiting factor in development of bulk (non-monolithic) LiNbO₃ optical resonators. From experiment, an optical Q of 1×10^6 is an acceptable quality of polishing. Ignoring scattering losses at disk sidewalls, intrinsic optical radiation losses in a WGM of $l = m \sim 15$ will result in an intrinsic optical Q of 1×10^6 [79]. This results in a lower bound of disk diameter equal to $3.5 \mu\text{m}$. The lowest frequency of operation of a microphotonic resonator is equal to the free spectral range, $f_{FSR} = c/(n_{opt}\pi d)$ and therefore determined by the disk diameter, d . For example, 100 GHz modulation gives a disk diameter of 0.45 mm . Polishing of bulk curved sidewalls for a disk of this size may be achievable with advanced polishing techniques. The 2 mm diameter disk shown in Chapter 2 was achievable, and the jump to 0.5 mm may therefore be within reach. Mode size is also of no concern

because the projection of the mode along the z -axis becomes smaller as radius decreases as shown in Section 3.2. At or above 100 GHz , RF material properties come into question. Literature has shown that $LiNbO_3$ RF properties are acceptable up to 140 GHz [87], but no information on RF properties were found beyond that frequency. In addition, the ability to couple RF fields on to the disk is yet another challenge that must be addressed. If one is only interested in the 10 to 100 GHz RF range, monolithic manufacture of this resonator with advanced lithography, and future electro-optic materials, is not precluded.

4.11 System impact/efficiency

4.11.1 Thermal stability

Thermal control is critical in determining the stability of the resonant optical mode. Table 1 in Chapter 2 lists coefficients for the change in refractive index and thermal expansion of $LiNbO_3$ due to temperature change. For a disk of diameter 5.84 mm , the thermal change in the optical resonant wavelength λ_{opt} is $d\lambda_{opt}^e/dT = 24.2 pm/^\circ C = 3.02 GHz/^\circ C$ along the extraordinary axis (z -axis), and along the ordinary axis $d\lambda_{opt}^o/dT = 25.4 pm/^\circ C = 3.17 GHz/^\circ C$. The change in wavelength for thermal expansion is 10 times larger than that from refractive index change. Given that a typical mode is 60 MHz , this shift is significant, and thermal stabilization must be factored into any system design. A simple way to achieve this is use of a control

voltage applied across the LiNbO₃ electrodes as part of a feedback loop controlling the optical resonance wavelength, and/or an input laser wavelength control feedback loop that locks the optical resonance to the laser line.

4.11.2 System noise

In the microphotonic receiver shown in Figure 5, there are three main sources of noise; (1) RF electrical noise incident on the RF electrode, (2) RIN noise of the input laser power, and (3) RF electrical noise generated by the optical receiver.

Figure 66 shows a block diagram of the receiver, where P_{RF}^{in} and N_{RF}^{in} are the input RF power and input RF noise on the electrode. P_{opt}^{in} (N_{opt}^{in}) is the input CW laser optical power (noise) coupled into the microphotonic modulator, and P_{opt}^{out} (N_{opt}^{out}) is the input CW laser optical power (noise). The output electrical power and noise from the optical detector is P_{RF}^{out} and N_{RF}^{out} .

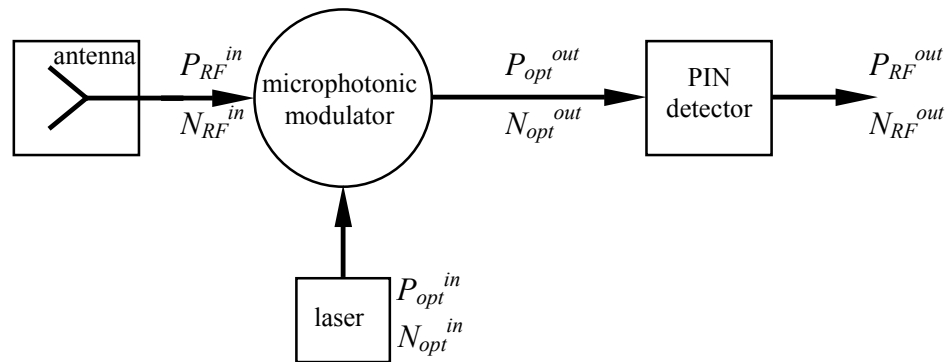


Figure 66. Block diagram of the noise model.

In a real system, N_{RF}^{in} will be dominated by the RF noise of the received RF signal at the antenna. This noise is dominated by unwanted signals from multipath, with significant additional noise from thermal noise and interference from other RF sources. In this case, noise is calculated from the received RF signal to noise ratio (SNR_{in}).

The small signal modulated optical power P_{opt}^{out} generated by the received RF power P_{RF}^{in} is approximated by the linear transfer function of the simulation of Section 4.6.4.

$$P_{opt}^{out} = (2.13 \times 10^{-5}) E_{RF}^{in}(V/m) P_{opt}^{in}(W)$$

where $E_{RF}^{in} = V_{RF}^{in} / d = (P_{RF}^{in} R)^{1/2} / d$, R is the resistance in the antenna circuit, and d is the disk thickness. The optical noise from light exiting the microphotonic modulator resulting from RF noise input N_{RF}^{in} is similarly found from

$$N_{opt}^{out}(RF) = (2.13 \times 10^{-5}) (N_{RF}^{in} R)^{1/2} / d P_{opt}^{in}$$

where we assume P_{opt}^{in} is 5 mW, $R_{PIN} = 10 \text{ k}\Omega$ from the transimpedance amplifier (TIA) resistor, and $d = 0.1 \text{ mm}$.

Random intensity noise (RIN) dominates the laser noise N_{opt}^{in} , and is equal to [89]

$$N_{opt}^{in} = [RIN(Hz^{-1}) \Delta f_{laser}]^{1/2} P_{opt}^{in}$$

where $RIN \sim -140 \text{ dB}/\text{Hz} = 10^{-14} \text{ Hz}^{-1}$ is typical for single mode semiconductor lasers where spontaneous emission is the main source of noise. Although challenging,

external feedback loops may be able to stabilize a typical laser linewidth, Δf_{laser} to less than 0.01 MHz. Assuming uncorrelated noise, N_{opt}^{in} adds to the optical noise generated by the RF input noise $N_{opt}^{out}(RF)$ such that $N_{opt}^{out} = N_{opt}^{out}(RF) + N_{opt}^{in}$. In addition, the optical resonator acts as an optical filter to the input optical noise. This filtering is ignored for Q 's of 10^6 since the resulting optical pass-band (~ 100 MHz) is wider than the noise bandwidth.

The optical input P_{opt}^{out} and associated optical noise N_{opt}^{out} is received at the detector. The photodiode has noise from both dark and photo currents. Current fluctuations called shot noise consist of discrete electrons flows which change in a quantum manner. This noise is found from $N_{RF}^{out}(\text{shot}) = 2q\Delta f_{PIN}(I_p + I_{ds})R$ [88]. Here $q = 1.6 \times 10^{-19}$ C is the electron charge and Δf_{PIN} is the receiver noise bandwidth. These currents are typically 10's of nA for the dark current, and mA's for the photo current. Therefore $N_{RF}^{out}(\text{shot}) \sim 1.4$ nW. The final significant source of noise is the thermal (Johnson) noise of the resistor in the PIN detector. In a photodiode, bias and feedback resistors contribute thermal noise due to the random motion of the electrons. This thermal noise, $N_{RF}^{out}(\text{thermal}) = 4 k_b T(^{\circ}K) \Delta f_{PIN}$ where the device temperature $T(^{\circ}K) = T(^{\circ}C) + 273$ °C and Boltzmann's constant $k_b = 1.38 \times 10^{-23}$ J/°K [88]. For a ideal narrow band 100 MHz PIN receiver centered at the RF carrier frequency of interest at 290 °K, $N_{RF}^{out}(\text{thermal}) = 1.6$ pW. Therefore shot noise is

1000 times larger than thermal noise and dominates. Any amplifier noise after the PIN would dominate thermal noise.

Figure 67 shows results of the above theoretical noise analysis. The output signal to noise ratio $SNR_{out} = P_{RF}^{out} / N_{RF}^{out}$ and noise figure $NF = (P_{RF}^{out} / N_{RF}^{out}) / (P_{RF}^{in} / N_{RF}^{in})$ are plotted versus the input RF signal to noise ratio $SNR_{in} = P_{RF}^{in} / N_{RF}^{in}$. This simulation assumes a RF input of $1 \mu W$, $5 mW$ coupled laser input, disk thickness of $100 \mu m$, 180Ω input resistance, and detector efficiency of $0.88 A/W$.

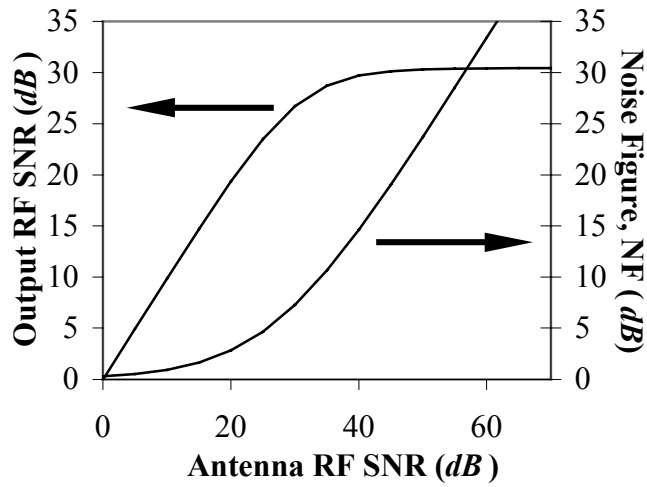


Figure 67. Estimated signal to noise ratio (SNR) and noise figure (NF) versus the input RF signal to noise ratio.

The targeted minimum input RF sensitivity of the microphotonic RF receiver is $1 \mu W$ ($-30 dBm$). Using this RF input power, the resulting maximum SNR_{out} is $-30 dB$

electrical. This limitation to SNR_{out} is primarily a result of the shot noise at the detector. Optical receiver noise is two orders of magnitude larger than RIN noise.

Allowing for both a 3 dB input RF coupling loss and a 3 dB input optical coupling loss, results in a maximum SNR_{out} of -27 dB electrical. This decreased SNR_{out} is from the loss of detected signal and not from an increase in noise terms.

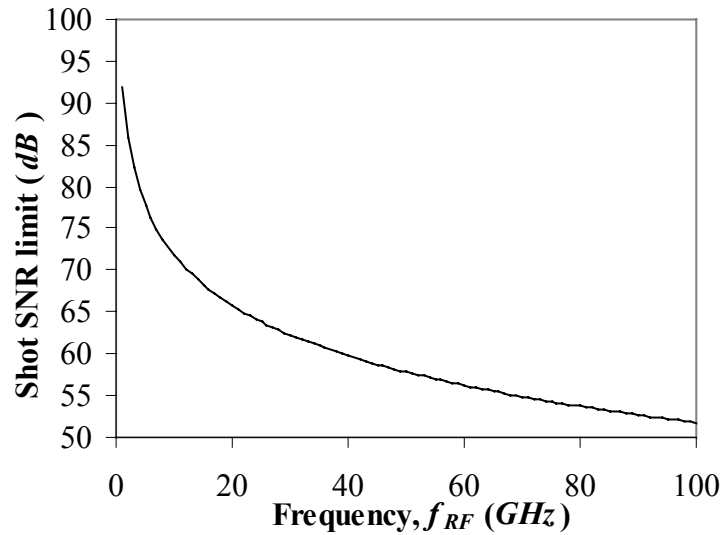


Figure 68. Shot noise imposed maximum signal to noise ratio SNR_{in} at the antenna for a $1 \mu W$ RF signal.

Shot noise at the RF antenna places an upper bound on the minimum input signal to noise ratio SNR_{in} . The minimum power received P_{RF}^{in} at the antenna will reach a quantum limit (shot noise), which can be approximated as the point when the detected noise power N_{RF}^{in} fluctuates at one RF photon per RF period or $N_{RF}^{in} \sim hf/\Delta t$

$\sim hf^2$. For the desired $1 \mu W$ RF sensitivity, Figure 68 shows the shot noise imposed maximum signal to noise ratio SNR_{in} .

At $60 GHz$, shot noise limits SNR_{in} to 56. However, Figure 67 shows that the best output signal to noise ratio occurs when $SNR_{in} \geq 50 dB$. Therefore, shot noise at the antenna begins to limit device performance above frequencies $\sim 60 GHz$.

Figure 69 shows experimental modulation results using the direct contact T-electrode. This noise floor is that of the spectrum analyzer. This figure demonstrates that a SNR_{out} of greater than $35 dB$ is achievable.

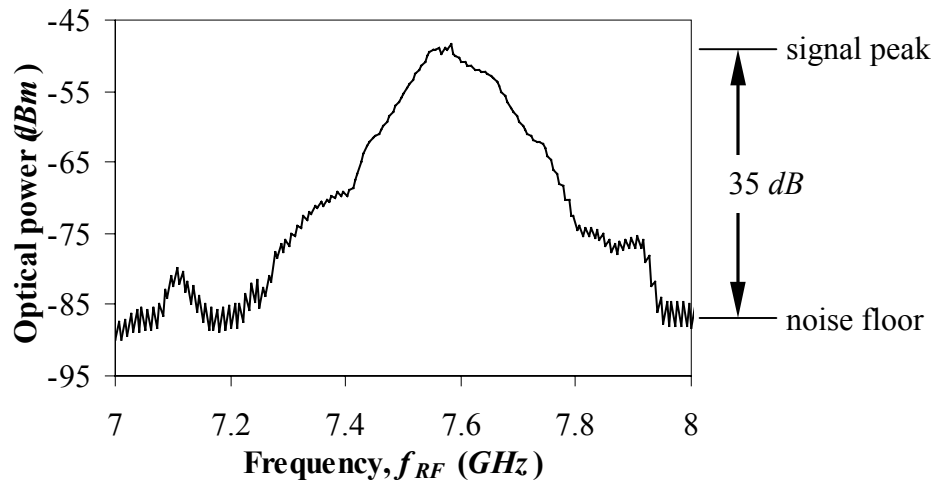


Figure 69. Swept RF optical modulation response of the direct contact (“T” electrode) RF coupling method. The noise floor is that of the RF spectrum analyzer.

4.12 Summary

A new type of electro-optic modulator using a z -cut LiNbO_3 disk-shaped resonator with optically-polished curved side-walls has been demonstrated. Initial experiments have achieved near 100% modulation at voltages comparable to MZ modulators.

There are two bands of modulation with fundamentally different physical causes. Base-band modulation of the LiNbO_3 disk is accomplished by shifting the resonant frequency of the disk on and off the input optical frequency. Out-of-band modulation is more complex and involves coupling of photons into optical side-bands at the FSR of the disk.

Numerical simulation of a microphotonic modulator which uses simultaneous resonance of optical and RF electric-fields has demonstrated that efficient modulation is achievable at mm -wave frequencies through the use of a periodic metal electrode. Dual resonance of optical and RF fields was achieved using direct-contact or “T - electrode”, while simultaneous resonance with voltage gain was successfully exploited using a side-coupled electrode configuration. Experimental results confirm our model and demonstrate modulation at mm -wave frequencies.

In addition, linearity, system noise, system thermal stability, and scaling of the microphotonic modulator was addressed.

4.13 References

- [79] Kouroggi, M., Nakagawa, K., and Ohtsu, M.: 'Wide-span optical frequency comb generator for accurate optical frequency difference measurement' IEEE J. Quantum Electron., 1993, **29**, pp. 2693-2701
- [80] Rizzi, P. A.: 'Microwave Engineering Passive Circuits', (Prentice Hall, Englewood Cliffs, NJ, 1988), ISBN 0-13-586702-9
- [81] GENESISe - EM Lab Version 6.0 developed by Integrated System Engineering (ISE), Switzerland, available at <http://www.ise.ch/>
- [82] Microwave materials division of Rogers Corp., available at <http://www.rogers-corp.com/mwu/index.htm>.
- [83] HFSS version 7.0 developed by Ansoft Corporation, Pittsburgh, PA, available at <http://www.ansoft.com/>.
- [84] Edwards, T., 'Foundations for microstrip circuit design', (John Wiley & Sons, New York, 1992), ISBN 0 471 93062 8
- [85] Horng, T. S., Yang, H. Y., and Alexopoulos, N. G.: 'A full-wave analysis of shielded microstrip line-to-line transitions', IEEE MTT-S International Microwave Symposium, 1990, pp. 251-254
- [86] Green, D. C., 'Radio communication', (Pearson Education, Essex, UK, 2000), ISBN 0 582 36908 8
- [87] Robertson, W. M., Arjavalingham, G., and Kopcsay, G. V.: 'Broadband microwave dielectric properties of LiNbO₃', Electron. Lett., 1991, **27**, pp. 175-176
- [88] Green, L. D.: 'Fiber Optic Communications', (CRC Press, Ann Arbor, MI, 1993) ISBN 0-8493-4470-0
- [89] Senior, J. M., 'Optical fiber communications: principles and practice', (Prentice Hall, New York, 1992), ISBN 0-13-635426-2

Chapter 5

Conclusion and future work

5.1 Conclusions

Placing future opto-electronic systems into the marketplace require development of novel optical building blocks. Research and development of LiNbO₃ microphotonic technologies provides us with one possible source for devices to be used in RF receivers for *mm*-wave wireless and front-end antenna applications. This first introduction of an active material into contemporary microresonator research should inspire development of an entirely new line of technologies merging electro-optic materials and high- Q resonant cavities.

A new type of *mm*-wave RF receiver architecture using a *z*-cut LiNbO₃ disk-shaped resonator with optically-polished curved side-walls and direct electrical-to-optical conversion has been demonstrated. Numerical simulation of a microphotonic modulator which uses simultaneous resonance of optical and RF electric-fields has shown that efficient modulation is achievable at *mm*-wave frequencies through the

use of a periodic metal electrode. Initial experiments have achieved near 100% modulation at voltages comparable to Mach Zehnder modulators. In addition, experimental results confirm our model and demonstrate modulation at *mm*-wave frequencies

Optical polishing of LiNbO₃ has led to optical Q 's greater than 10^6 . Decreasing the radius of the disk to 2 *mm*, and the thickness to 200 μm has been achieved. Scaling down beyond these dimensions will introduce new challenges, but should be achievable by an extension of current methods. As a complication of the high index of LiNbO₃, optical coupling methods are limited and challenging. Initial experiments have achieved up to 25 % coupling of light using prism coupling. New coupling schemes must be developed to reduce device insertion loss to acceptable limits. In addition, the ability to pattern gold electrodes for RF field coupling has also been demonstrated.

RF WGM excitation at *GHz* frequencies using stripline coupling suggests that the LiNbO₃ material system will not limit the extension of experiments to *mm*-wave RF frequencies. In addition, resonance spectra and pulse response of the passive LiNbO₃ optical cavity show features similar to that of silica spheres. Therefore, optical WGM coupling is not limited by the birefringent nature of LiNbO₃.

This work has presented two bands of modulation with fundamentally different physical origins. Base-band modulation of the LiNbO₃ disk is generated by an induced shift in the refractive index of the disk. This shifts the input optical frequency into and out of resonance with the LiNbO₃ disk. At these slower modulations, photons have time to build up and decay, and modulation times follow that of the optical Q . Out-of-band modulation is more complex and involves coupling of photons into optical side-bands at the FSR of the disk.

Numerical simulation of a microphotonic modulator which uses simultaneous resonance of optical and RF electric-fields has demonstrated that efficient modulation is achievable at mm -wave frequencies through the use of periodic metal electrodes. Dual resonance of optical and RF fields was achieved using direct-contact or “T - electrode”, while simultaneous resonance providing voltage enhancement was successfully exploited using a side-coupled electrode configuration. Finally, linearity, system noise, system thermal stability, and scaling issues of the microphotonic modulator were addressed.

In conclusion, both simulation and experimental results suggest the use of LiNbO₃ microphotonic resonators as building blocks in a new class of small, lightweight, and efficient microphotonic components for mm -wave receivers is achievable.

5.2 Future work

This work has accomplished significant achievements toward the development of an entirely new microphotonic based receiver architecture. However, there are many avenues that must be investigated to justify the viability of the microphotonic modulator in tomorrow's marketplace.

Future work is divided into the categories of optical coupling, RF electrical coupling, system issues, and alternate design implementations

Optical coupling

Improvement in optical coupling to the LiNbO_3 microphotonic modulator is a function of the optical coupling coefficient (Chapter 3). This coefficient is determined by the physical geometry of the prism / disk coupling interface. Experiments suggest that optical coupling using large disks ($\sim 3 \text{ mm}$ radius) and diamond prisms resides in the undercoupled regime. An understanding of the relationship between disk diameter and the coupling coefficient will improve the chances of critical coupling of light into the disk. However, the mixed geometries of the flat prism and curved resonator complicate any analytical solution and make a theoretical understanding of coupling a significant challenge. In addition, finite element simulations are not practical due to the large size of the optical resonator relative to the optical wavelength. Therefore an experimental approach with varying

silica sphere diameters is suggested as the most time efficient manner to understand the relationship between disk diameter and coupling coefficient.

Improved coupled should be achievable through pre-distortion of the optical beam. The flat prism coupler was shown (Chapter 3) to be a non-ideal coupling geometry. Therefore, by modifying or adding optical elements (such as cylindrical lenses) to critically couple the optical input beam to the disk resonance, improved coupling should be obtainable. More advanced coupling methods would introduce an appropriately modified prism coupler to achieve the desired beam control.

Enhanced optical coupling into the fundamental TE polarized $l = m$ whispering gallery modes will allow for improved optical alignment, and increased signal to noise of the optically modulated output. Ideally, spherical whispering gallery modes with fixed l but differing m have degenerate resonance frequencies. However, aspherical imperfections in the disk break this degeneracy. By enhancing the aspherical nature of the disk, coupling into higher order modes should be reduced. This can be achieved experimentally by reducing the radius of curvature of the polished curved side-walls for a fixed disk radius. A simple extension of current optical polishing techniques should allow for the manufacture of these new aspherical disks.

The dependence of input polarization when optically coupling into the LiNbO₃ disk has not yet been completely understood. The birefringent nature of the disk introduces this new parameter to traditional microsphere WGM research. A complete understanding of polarization dependence, and specifically the nature of the TM mode's ease of optical alignment compared to the TE mode may shed some new insight into optical coupling issues.

RF electrical coupling

Although trivial, a proof of increased sensitivity through decreasing electrode separation should be pursued to demonstrate the feasibility of compact device packaging. A more significant challenge is excitation of more than one electrode in the periodic electrode structure. The ramifications of electrode cross-talk should be understood at an early stage because of its impact on future electrode design.

Finally, antenna design and integration has not been addressed in this work. Although secondary to modulator development, antenna design will impact future electrode configuration and a parallel research track should be undertaken.

System issues

Modulation instability has generally been attributed to thermal and mechanical fluctuations in both the mount and LiNbO₃ disk. In addition, heating of the RF

electrode by the applied RF power results in significant additional thermal variations. Improvement in modulation stability is therefore a significant challenge that must be addressed. One possible solution uses the electro-optic nature of the disk to provide a feedback loop. This provides a natural mechanism to control the resonant wavelength of the device. In addition, improvements in RF modulation efficiency will reduce RF electrode heating by reducing received RF power requirements.

Selection of an optical encoding scheme should also be investigated. Optical filtering by the LiNbO₃ modulator (Chapter 4) will naturally suppress one optical side-band while enhancing the other side-band. This may suggest that an early encoding scheme candidate is single-side-band (SSB) modulation

Alternate geometries

Although this work shows that bulk LiNbO₃ disks with curved side-walls are practical candidates for future product development, alternate geometries should not be dismissed. For example, the use of Ti-indiffusion to form a waveguide around the equator of the disk may be a practical way to either enhance optical confinement of the fundamental mode, or a method to remove the need for curved side-wall confinement entirely. Although additional losses would be incurred, the real challenge is developing methods to lithographically define the waveguide around a curved surface. Development of a high- Q planar geometry with lithographically

defined coupling regions would provide the greatest feasible for a commercially viable design.

Appendix A

Microwave band designations

A.1 Designation of the microwave spectrum

This appendix is provided to clarify the letter designation of microwave bands. Table 2 shows RF band designations from three different sources covering 100 *MHz* - 143 *GHz*. As demonstrated from the differing band allocations between sources, there is no consistent band allocation in the literature. Therefore, care must be taken while surveying the literature.

Figure 70 shows the atmospheric attenuation for electromagnetic waves as a function of frequency [93]. The Ka band is near a local minimum of atmospheric absorption. V-band covers a peak in atmospheric absorption due to O₂ near 60 *GHz*, and is therefore targeted as an opportune frequency for spectral channel re-use by atmospheric absorption in micro-cell networks [94]. The W band is of use for its local minimum of absorption near 100 *GHz*. D-band again is a high atmospheric absorption band from O₂ molecular resonance.

Table 2 Microwave frequency band designations.

Designation	Microwave Engineering Passive Circuits [90]		Ref. Data for Radio Engineers [91]	US Navy [92]
	Frequency	Wavelength	Frequency	Frequency
I				100 – 150 MHz
G				150-225 MHz
P			225-390 MHz	225-390 MHz
L	1 - 2 GHz	30.0 - 15.0 cm	0.39 – 1.55 GHz	0.39 – 1.55 GHz
S	2 - 4 GHz	15.0 - 7.5 cm	1.55 – 5.2 GHz	1.55 – 3.9 GHz
C	4 - 8 GHz	7.5 - 3.8 cm	3.9 – 6.2 GHz	3.9 – 6.2 GHz
X	8 - 12 GHz	3.8 - 2.5 cm	5.2 – 10.9 GHz	6.2 – 10.9 GHz
Ku	12 - 18 GHz	2.5 - 1.7 cm	15.35 – 17.25 GHz	15.25 – 17.25 GHz
K	18 - 26 GHz	1.7 - 1.2 cm	10.9 – 36 GHz	10.9 – 36 GHz
Ka	26 - 40 GHz	1.2 - 0.8 cm	33 – 36 GHz	33 – 36 GHz
Q	42 - 46 GHz	7.1 - 6.5 mm	36 – 46 GHz	36 - 46 GHz
V	54 - 62 GHz	5.6 - 4.8 mm	46 – 56 GHz	46 – 56 GHz
W	92 - 96 GHz	3.3 - 3.1 mm	56 – 100 GHz	56 – 100 GHz
D	137-143 GHz	2.2 - 2.1 mm		

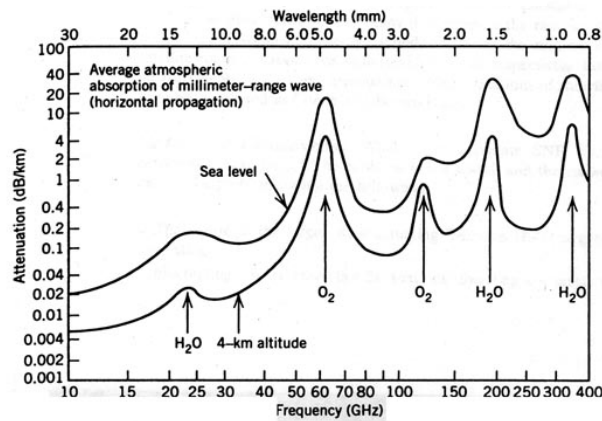


Figure 70. Atmospheric attenuation for millimeter waves.

A.2 References

- [90] Rizzi, P. A.: 'Microwave Engineering Passive Circuits', (Prentice Hall, Englewood Cliffs, NJ, 1988), ISBN 0-13-586702-9
- [91] Jordan, E. C.: 'Reference Data for Radio Engineers, Fifth Edition', (Howard W. Sams & Co., Inc., Indianapolis, Indiana: 1970)

- [92] US Navy Submarine Communications Spectrum, available at <http://www.fas.org/man/dod-101/navy/docs/scmp/apx-c.pdf>
- [93] Fourikis, N.: 'Phased array-based systems and applications', (John Wiley & Sons, NY, 1997), ISBN 0-471-01212-2
- [94] Ohata, K., Inoue, T., Funabashi, M., Inoue, A., Takimoto, Y., Kuwabara, T., Shinozaki, S., Maruhashi, K., Hosaya, K., and Nagai, H.: 'Sixty-GHz-Band Ultra-Miniature Monolithic T/R Modules for Multimedia Wireless Communication Systems', IEEE Trans. Microwave Theory Techn., 1996, **44**, pp. 2354-2360

Appendix B

Bibliography

- Braginsky, V. B.; Gorodetsky, M. L.; and Ilchenko, V. S.: 'Quality-factor and nonlinear properties of optical whispering-gallery modes', *Phys. Lett. A*, 1989, **137**, pp. 393-397
- Braginsky, V. B.; Gorodetsky, M. L.; and Ilchenko, V. S.: *Sov. Phys. Dokl.*, 1987, **32**, pp. 306-309
- Cai, M., and Vahala, K.: 'Highly efficient optical power transfer to whispering-gallery modes by use of a symmetrical dual-coupling configuration', *Opt. Lett.*, 2000, **25**, (4), pp. 260-262
- Cai, M., Hedekvist, P. O., Bhardwaj, A., and Vahala, K.: '5-Gbit/s BER performance on an all fiber-optic add/drop device based on a taper-resonator-taper structure', *IEEE Photon. Tech. Lett.*, 2000, **12**, pp. 1177-1178
- Cai, M., Hunziker, G.; and Vahala, K.: 'Fiber-optic add-drop device based on a silica microsphere-whispering gallery mode system', *IEEE Photon. Tech. Lett.*, 1999, **11**, pp. 686-687
- Chelnokov, A.V., and Lourtioz, J. M.: 'Optimized coupling into planar waveguides with cylindrical prisms' *Electron. Lett.*, 1995, **31**, pp. 269-271
- Chu, S. T.; Pan, W.; Suzuki, S.; Little, B. E.; Sato, S.; and Kokubun, Y.: 'Temperature insensitive vertically coupled microring resonator add/drop filters by means of a polymer overlay', *IEEE Photon. Tech. Lett.*, 1999, **11**, pp. 1138-1140
- Collot, L.; Lefevre-Seguin, V.; Brune, M.; Raimond, J. M.; and Haroche, S.: *Europhys. Lett.*, 1993, **23**, pp. 327-334

- Edwards, T., 'Foundations for microstrip circuit design', (John Wiley & Sons, New York, 1992), ISBN 0 471 93062 8
- Fourikis, N.: 'Phased array-based systems and applications', (John Wiley & Sons, NY, 1997), ISBN 0-471-01212-2
- Frateschi, N. C.; and Levi, A. F. J.: 'The spectrum of microdisk lasers', *J. Appl. Phys.*, 1996, **80**, pp. 644-653
- Gargione, F. and Iida T.: 'Services, technologies, and systems at Ka band and beyond – a survey', *IEEE J. Select. Areas Commun.*, 1999, **17**, (2), pp. 225-229
- Gayral, B., Gerard, J. M., Lamaitre, A., Dupuis, C., Manin, L., and Pelouard, J. L.: 'High Q wet-etched GaAs microdisks containing InAs quantum boxes', *Appl. Phys. Lett.*, 1999, **75**, pp. 1908-1910
- GENESISe - EM Lab Version 6.0 developed by Integrated System Engineering (ISE), Switzerland, available at <http://www.ise.ch/>
- Gorodetsky, M. L. and Ilchenko, V. S.: 'High-Q optical whispering-gallery microresonators: precession approach for spherical mode analysis and emission patterns with prism couplers', *Opt. Comm.*, 1994, **113**, pp. 133-143
- Gorodetsky, M. L.; and Ilchenko, V. S.: 'Optical microsphere resonators: optimal coupling to high-Q whispering-gallery modes', *J. Opt. Soc. Am. B.*, 1999, **16**, pp. 147-154
- Gorodetsky, M. L., Savchenkov, A. A., and Ilchenko, V. S.: 'Ultimate Q of optical microsphere resonators' *Opt. Lett.*, 1996, **21**, pp. 453-455
- Green, D. C.: 'Radio communication', (Pearson Education, Essex, UK, 2000), ISBN 0 582 36908 8
- Green, L. D.: 'Fiber Optic Communications', (CRC Press, Ann Arbor, MI, 1993) ISBN 0-8493-4470-0
- Hecht, E.: 'Optics', (Addison-Wesley Publishing Company, Inc., NY, 1987)
- Hecht, J.: 'Long-haul DWDM systems go the distance', *Laser Focus World*, 2000, **36**, (10), pp. 23-28
- HFSS version 7.0 developed by Ansoft Corporation, Pittsburgh, PA, available at <http://www.ansoft.com/>.

- Hida, Y., Imamura, S., and Izawa, T.: 'Ring Resonator Composed of low loss polymer waveguides at 1.3 μm ', *Electron. Lett.*, 1994, **28**, (14), pp. 1314-1316
- Hill, S. C., and Benner, R. E.: 'Optical Effects Associated With Small Particles', (World Scientific, Singapore, 1988)
- Ho, K. P., and Kahn, J. M.: 'Optical frequency comb generator using phase modulation in amplified circulating loop', *IEEE Photon. Tech. Lett.*, 1993, **5**, (6), pp. 254-256
- Hoffman, R. K.: 'Handbook of microwave integrated circuits', (Artech House, Norwood, MA, 1987) ISBN 0-89006-163-7
- Hornig, T. S., Yang, H. Y., and Alexopoulos, N. G.: 'A full-wave analysis of shielded microstrip line-to-line transitions', *IEEE MTT-S International Microwave Symposium*, 1990, pp. 251-254
- Hryniewicz, J. V.; Absil, P. P.; Little, B. E.; Wilson, R. A.; and Ho, P. T.: 'Higher order filter response in coupled microring resonators', *IEEE Photon. Tech. Lett.*, 1999, **12**, pp. 320-322
- Hutcheson, L. D.: 'Integrated Optical circuits and components', (Merzel Dekker, Inc., New York, 1987), ISBN 8-8247-7575-9
- Ilchenko, V. S., Volikov, P. S., Velichansky, V. L., Treussart, F., Lefevre-Seguin, V., Raimond, J. M., and Haroche, S.: 'Strain-tunable high-Q optical microsphere resonator', *Opt. Comm.*, 1998, **145**, pp. 86-90
- Ilchenko, V. S.; Yao, X. S.; and Maleki, L.: 'Pigtailing the high-Q microsphere cavity: a simple fiber coupler for optical whispering-gallery modes', *Optics Lett.*, 1999, **24**, pp. 723-725
- Jordan, E. C.: 'Reference Data for Radio Engineers, Fifth Edition', (Howard W. Sams & Co., Inc., Indianapolis, Indiana: 1970)
- Khan, M. J.; Manolatu, C.; Shanhu, F.; Villeneuve, P. R.; Haus, H. A.; and Joannopoulos, J. D.: 'Mode-coupling analysis of multipole symmetric resonant add/drop filters' *IEEE J. Quan. El.*, 1999, **35**, pp. 1451-1460
- Klien, M. V., and Furtak, T. E.: 'Optics', (John Wiley and Sons, New York, 1986), ISBN 0-471-87297-0

- Knight, J. C.; Cheung, G.; Jacques, F.; and Birks, T. A.: 'Phase-matched excitation of whispering-gallery-mode resonances by a fiber taper', *Opt. Lett.*, 1997, **15**, pp. 1129-1131
- Knight, J. C.; Dubreuil, N.; Sandoghdar, V.; Hare, J.; Lefevre-Seguin, V.; Raimond, J. M.; and Haroche, S.: 'Mapping whispering-gallery modes in microspheres with a near-field probe', *Opt. Lett.*, 1995, **20**, pp. 1515-1517
- Korotky, S. K., and Alferness, R. C.: 'Integrated optical circuits and components', (Marcel Dekker, Inc., New York, 1987), ISBN 8-8247-7575-9
- Kouroggi, M., Nakagawa, K., and Ohtsu, M.: 'Wide-span optical frequency comb generator for accurate optical frequency difference measurement' *IEEE J. Quantum Electron.*, 1993, **29**, pp. 2693-2701
- Laine, J. P., Little, B. E., Lim, D. R., Tapalian, H. C., Kimerling, L. C., and Haus, H. A.: 'Microsphere resonator mode characterization by pedestal anti-resonant reflecting waveguide coupler', *IEEE Photon. Tech. Lett.*, 2000, **12**, (8), pp. 567-569
- Laine, J. P., Little, B. E., Lim, D. R., Tapalian, H. C., Kimerling, L. C., and Haus, H. A.: 'Planar integrated wavelength-drop device based on pedestal antiresonant reflecting waveguides and high-Q silica microspheres', *Opt. Lett.*, 2000, **25**, (22), pp. 1225-1234
- Lee, D. L.: 'Electromagnetic Principles of Integrated Optics', (John Wiley & Sons, NY, 1986)
- Levi, A. F. J.; McCall, S. L.; Pearton, S. J.; and Logan, R. A.: 'Room temperature operation of submicrometre radius disk laser' *Electron. Lett.*, 1993, **29**, pp. 1666-1667
- LiNbO₃ Group Home Page, University of Padova, Italy, available at <http://solidi4.padova.infm.it/research.html>
- Little, B. E., Laine, J. P., and Haus, H. A.: 'Analytic theory of coupling from tapered fibers and half-blocks into microsphere resonators', *J. Lightwave Technol.*, 1999, **17**, (4), pp. 704-708
- Little, B. E., Laine, J. P., Lim, D. R., Haus, H. A., Kimerling, L. C., and Chu, S. T.: 'Pedestal antiresonant reflecting waveguides for robust coupling to microsphere resonators and for microphotonic circuits', *Optics Letters*, 2000, **25**, (1), pp. 152-153

- Little, B. E.; Haus, H. A.; Foresi, J. S.; Kimerling, L. C.; Ippen, E. P.; and Ripin, D.: 'Wavelength switching and routing using absorption and resonance', IEEE Photon. Tech. Lett., 1998, **10**, pp. 816-818
- Little, B. E.; Laine, J. P.; and Haus, H. A.: 'Analytic theory of coupling from tapered fibers and half-blocks into microsphere resonators', IEEE J. Lightwave Tech., 1999, **17**, pp. 704-715
- Little, B., Laine, J., and Chu, S.: 'Surface-roughness-induced contradirectional coupling in ring and disk resonators', Optics Lett., 1997, **22**, (1), pp. 4-6
- Lord Rayleigh (J. W. Strutt): 'The problem of the whispering gallery', Phil. Mag., 1910, **20**, pp. 1001-1004
- Mabuchi, H. and Kimble, H. J.: 'Atom galleries for whispering atoms: binding atoms in stable orbits around an optical resonator', Opt. Lett., 1994, **19**, pp. 749-751
- McCall, S. L., Levi, A. F. J., Slusher, R. E., Pearton, S. J., and Logan, R. A.: 'Whispering mode microdisk lasers', Appl. Phys. Lett., 1992, **60**, pp. 289-291
- McKinley, M. C., Smith Jr., C. V., Nunnally, W. C., Magnusson, R., and Black, T. D.: 'A spherical electro-optic high-voltage sensor', Pulsed Power Conference, 1989, **7**, pp. 380 – 383
- McKinley, M. C., Smith Jr., C. V., Nunnally, W. C., Magnusson, R., and Black, T. D.: 'Laser interference figure measurement of 60 Hz high voltages using a LiNbO₃ spherical electrooptic sensor', IEEE Photon. Tech. Lett., 1990, **2**, (6), pp. 447-449
- Microwave materials division of Rogers Corp., available at <http://www.rogers-corp.com/mwu/index.htm>.
- New Focus Corp., available at <http://www.newfocus.com>
- Noguchi, K., Mitomi, O., and Miyazawa, H.: 'Millimeter-wave Ti:LiNbO₃/sub 3/ optical modulators', J. Lightwave Tech., 1998, **16**, pp. 615-619
- Ohata, K., Inoue, T., Funabashi, M., Inoue, A., Takimoto, Y., Kuwabara, T., Shinozaki, S., Maruhashi, K., Hosaya, K., and Nagai, H.: 'Sixty-GHz-Band Ultra-Miniature Monolithic T/R Modules for Multimedia Wireless Communication Systems', IEEE Trans. Microwave Theory Techn., 1996, **44**, pp. 2354-2360

- Reitz, J. R., Milford, F. J., and Christy, R. W., 'Foundations of electromagnetic theory, third edition', (Addison-Wesley Publishing Company, NY, 1980), ISBN 0-201-06332-8
- Rizzi, P. A.: 'Microwave Engineering Passive Circuits', (Prentice Hall, Englewood Cliffs, NJ, 1988), ISBN 0-13-586702-9
- Robertson, W. M., Arjavalingham, G., Kopcsay, G. V., 'Broadband microwave dielectric properties of Lithium Niobate', *Electron. Lett.*, 1991, **27**, pp. 175-176
- Rosenberger, A. T., and Rezac, J. P.: 'Evanescent wave sensor using microsphere whispering-gallery modes', *Proc. SPIE*, 2000, 3930, pp. 186-187
- Saitoh, T.; Kourogi, M.; and Ohtsu, M.: 'A waveguide-type optical-frequency comb generator' *IEEE Photon. Tech. Lett.*, 1995, **7**, pp. 197-199
- Sandoghdar, V.; Treussart, F.; Hare, J.; Lefevre-Seguin, V.; Raimond, J. M.; and Haroche, S.: 'Very low threshold whispering-gallery-mode microsphere laser', *Phys. Rev. A*, 1996, **54**, pp. 1777-1780
- Schiller, S., Yu, I., Feher, M., and Byer, R.: 'Fused-silica monolithic total-internal-reflection resonator', *Optics Lett.*, 1992, **17**, (5), pp. 378-380
- Senior, J. M., 'Optical fiber communications: principles and practice', (Prentice Hall, New York, 1992), ISBN 0-13-635426-2
- Serpenguzel, A.; Arnold, S.; and Griffel, G.: 'Excitation of resonances of microspheres on an optical fiber' *Opt. Lett.*, 1995, **20**, pp. 654- 656
- Steier, W. H., Chen, A., Lee, S., Garner, S., Zhang, H., Chuyanov, V., Dalton, L. R., Wang, F., Ren, A. S., Zhang, C., Todorova, G., Harper, A., Fetterman, H. R., Chen, D., Udupa, A., Bhattacharya, D., and Tsap, B.: 'Polymer electro-optic devices for integrated optics', *Chemical Physics*, 1999, 245, pp. 487-506
- Stratton, J.A.: 'Electromagnetic theory', (McGraw-Hill Book Company, New York, 1941)
- Thiyagarajan, S. M. K.; Cohen, D. A.; Levi, A. F. J.; Ryu, S.; Li, R.; and Dapkus, P. D.: 'Continuous room-temperature operation of microdisk laser diodes', *Electron. Lett.*, 1999, **35**, pp. 1252-1254

- Thiyagarajan, S. M. K.; Levi, A. F. J.; Lin, C. K.; Kim, I.; Dapkus, P. D.; and Pearton, S. J.: 'Continuous room-temperature operation of optically pumped InGaAs/InGaAsP microdisk lasers' *Electron. Lett.*, 1998, **34**, pp. 2333-2334
- Tien, P.K., Ulrich, R.: 'Theory of Prism-Film Coupler and Thin-Film Light Guides', *J. Opt. Soc. Am.*, 1970, **60**, pp. 1325-1337
- Treussart, F.; Hare, J.; Collot, L.; Lefevre, V.; Weiss, D. S.; Sandoghdar, V.; Raimond, J. M.; and Haroche, S.: 'Quantized atom-field force at the surface of a microsphere', *Opt. Lett.*, 1994, **19**, pp. 1651-1693
- Ulrich, R.: 'Optimum excitation of optical surface waves', *J. Opt. Soc. Am.*, 1971, **61**, pp. 1467-1477
- US Navy Submarine Communications Spectrum, available at <http://www.fas.org/man/dod-101/navy/docs/scmp/apx-c.pdf>
- Valpey Fisher website, available at <http://www.valpeyfisher-ud.com/>
- Vassiliev, V. V.; Velichansky, V. L.; Ilchenko, V. S.; Gorodetsky, M. L.; Hollberg, L.; and Yarovitsky, A. V., 'Narrow-line-width diode laser with a high-Q microsphere resonator', *Opt. Comm.*, 1998, **158**, pp. 305-312
- Vedrenne, C., and Arnaud, J.: 'Whispering-gallery modes of dielectric resonators', *Proc. Inst. Elec. Eng. pt. H*, 1982, **129**, pp. 183-187
- Wait, J. R.: 'Electromagnetic whispering-gallery modes in a dielectric rod', 1967, *Radio Sci.*, **14**, (9), pp. 1005-1017
- Weis, R. S. and Gaylord, T. K.: 'Lithium Niobate: Summary of Physical Properties and Crystal Structure', *Appl. Phys. A*, 1985, **37**, pp. 191-203
- Wong, K. K.: 'Properties of lithium niobate', (INSPEC, Institution of Electrical Engineers, London, 1989), ISBN 0 85296 7993
- Yariv, A., Yeh, P.: 'Optical waves in crystals', (John Wiley and Sons, New York, 1984), ISBN 0-471-09142-1
- Yariv, A.: 'Voltage controlled micro cavity-waveguide coupling for switching, routing, and modulation of optical waves', *Darpa/MTO workshop*, 2000, pp. 56-68

